# DESIGN AND METROLOGY OF OPTICS FOR TELESCOPES AND SUNLIGHT CONCENTRATION

by

Ryker Eads

A Dissertation Submitted to the Faculty of the

JAMES C. WYANT COLLEGE OF OPTICAL SCIENCES

In Partial Fulfillment of the Requirements

For the Degree of

DOCTOR OF PHILOSOPHY

In the Graduate College

THE UNIVERSITY OF ARIZONA

2021

THE UNIVERSITY OF ARIZONA
GRADUATE COLLEGE

As members of the Dissertation Committee, we certify that we have read the dissertation prepared by **Ryker Eads**, titled ***Design and Metrology of Optics for Telescopes and Sunlight Concentration*** and recommend that it be accepted as fulfilling the dissertation requirement for the Degree of Doctor of Philosophy.

Date: _ 2/15/2021______

*Professor J. Roger P. Angel*

Date: _2/15/2021__

*Professor Daewook Kim*

Jose Sasian

Date: 2-15-21

*Professor José M. Sasián*

Final approval and acceptance of this dissertation is contingent upon the candidate's submission of the final copies of the dissertation to the Graduate College.

I hereby certify that I have read this dissertation prepared under my direction and recommend that it be accepted as fulfilling the dissertation requirement.

Date: ___2/15/2021_________

*Professor J. Roger P. Angel*
Dissertation Committee Chair
*Wyant College of Optical Sciences*

# ACKNOWLEDGEMENTS

I gratefully acknowledge the help and guidance that has been provided by my advisor and friend Roger Angel. I have learned more from him about applying science than from any other source throughout my education. He has been an example to me of dedication, passion, and humility. It has been an honor to work by his side.

I thank my professors at the College of Optical Sciences for taking the time to share their knowledge with me in their various classes: José Sasián, Dae Wook Kim, John Greivenkamp, John Koshel, and many more. José opened my eyes to the world of optical aberrations and the fun of optimizing an optical system. Dae Wook showed me many of the amazing ways that light can be used to measure the physical properties of a system. John G. was the first person who explained to me what it meant to image a pupil (or even what a pupil was), which has proven to be quite useful. John K. taught me about the fundamental limitation of étendue (which I may be naming one of my children after). Finally, I again thank my professor, Roger Angel, who helped me take the knowledge I gained from my course professors and apply it to the optical design of telescopes and solar energy systems, as well as metrology design, testing of optical systems, etc.

Throughout my courses I have been blessed to work with other students who have been great examples to me, and many times have helped me to deepen my knowledge: Justin Hyatt, Christian Davila, Travis Sawyer, Seth Erickson, and many more. For the new metrology idea presented in Section 5.6, I owe gratitude to my teammates in Dae Wook's Optical Testing Lab, who were joint contributors to the idea: Katharine Armstrong, Divya Guruprasad, and Amit Kumar Jha.

I owe much gratitude to the Boye family for their FoTO scholarship, which allowed a smooth transition into graduate school and has certainly allowed me to graduate sooner. Also, funding from Tech Launch Arizona, which provided the means for creating the actively focusing heliostat and associated metrology system of Chapter 4.

# DEDICATION

To my wife KaChele, who has loved and supported me in my pursuit of higher education. Without her encouragement I would not have made it this far. My children who have helped me to take time for the most important things. Also, my parents, who convinced me I was capable of more and have never stopped believing in me.

# TABLE OF CONTENTS

PAGE

# LIST OF FIGURES

**Page**

# LIST OF TABLES

# ABSTRACT

The principles of optical and metrology design form the foundation for technologies in many areas. Of interest to this dissertation are the areas of solar energy and telescopes. For solar energy, low quality (~1 mrad) solar disk images are formed for the purposes of photovoltaic or heat energy production. For space and ground telescopes, high quality (0.1-1.0 μrad) stellar images can be formed, especially over wide fields where phenomena such as dark energy can be further studied. There are 3-4 magnitudes of difference in precision between solar energy and telescopes, and yet similar optical and metrology design principles are applicable.

Concentrated solar energy can be used to exploit the benefits of high efficiency Photovoltaic Multi-Junction cells (CPV). The design of these optics is largely driven by the cost per watt of generation. Pupil-imaging techniques help with mispointing and low tolerance alignment of optical components. Several designs will be covered in detail, exploring their benefits and limitations.

The cousin to CPV, Concentrated Solar Power (CSP) is of special interest. Industry standards involve usage of tens of thousands of heliostats focusing sunlight on a central "power tower" at ~500X solar concentration. Concave focusing heliostats are of limited value, they suffer from spillage of sunlight around the tower receiver due to changing astigmatic aberrations as the sun angle changes. We have designed and built a prototype that uses active bending astigmatic modes in a 1.6 $m^2$ heliostat mirror, demonstrating sharp disk images of the Sun formed from 0 degree angle of incidence to >70 degree angle of incidence with >90% ensquared energy into an

area little larger than the disc image. With ~10X concentration only hundreds of heliostats are needed to achieve ~1000X.

Optical and metrology design are further applied to another metrology system for a 1.6-m gull-wing lens, which is part of a recent design for a wide field 6.5-m Cassegrain telescope. The telescope design is intended as a future replacement for DESI, acting as a spectrometer for ~10,000 stellar objects simultaneously. The gull-wing lens is a key component for the telescope achieving ~0.5 arcsecond resolution for a 3.0-degree field of view for 365 nm - 950 nm wavelengths.

Several other telescope designs are presented, including a ground telescope with 10,000 $m^2$ of area that can achieve 300,000X spectroscopic resolution for the oxygen band. This makes possible the search for life on exoplanets. Another design is presented that pushes resolution and field of view to the very limits of a 20-m space telescope with ~0.01 arcsecond resolution (at 1 μm wavelength) and a 1-degree field of view. A new class of telescopes with an analytical solution are presented, the Double-Cassegrain.

# CHAPTER 1 : INTRO TO OPTICAL AND METROLOGY DESIGN

## 1.1 Introduction

This dissertation addresses a series of topics that all share similar principles: solar concentration, telescope designs, and metrology. At a first glance, solar concentration, telescope designs, and metrology do not seem very related. However, an understanding of geometric optics is necessary for each, among other topics including pupil imaging, aberration theory, cost versus benefit, optimization techniques, etc. Design work for both optical and metrology systems rely upon the same fundamentals, particularly one major and somewhat obvious fundamental.

The design work and metrology for optical elements and systems depend on the specifications and requirements. What are you trying to measure and how good does that measurement have to be? Optical designs that are well optimized but require high-precision tolerances may be rejected in favor of other designs that perform worse but require lower tolerances. Metrology systems that measure the surface of an optic to sub-nanometer precision and accuracy may be required for high-performance systems, such as with Extremely Large Telescopes (ELT) [1]. This level of surface knowledge may not be required for loose-tolerance systems, such as for solar concentration. Sun Tzu once said, “Know thy enemy”. The “enemy” or challenge of an optical engineer is meeting the requirements. Therefore, the optical engineer may rephrase this to, “Know thy requirements.”

What follows is a series of sub chapters that introduce the fundamentals for understanding the contents of this dissertation. These sub chapters are brief and are therefore intended as solely a primer for the optical engineer. The topics discussed in this chapter will be freely used in the remaining chapters where solar concentration design, metrology systems and designs, and telescope designs will be discussed in detail.

## 1.2 Geometric Optics

A preliminary understanding of an optical system starts with the first order analysis. The well-known marginal and chief rays define important features of imaging (and pupil-imaging) designs. The marginal ray passes through the edge of the stop, and the chief ray passes through the center of the stop (see Figure 1.1). Where the marginal ray crosses the optical axis an image of the object is formed. Where the chief ray crosses the optical axis an image of the pupil is formed. Calculation of these crossings involves a first order ray trace, which requires three basic equations [2]. The first equation involves the change in ray height, which is calculated by

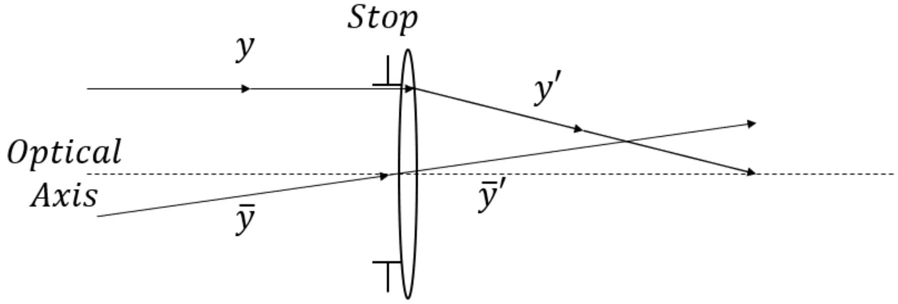

*Figure 1.1: A basic optical layout showing the chief ray in object space ($\bar{\mathbf{y}}$), marginal ray in object space ($\mathbf{y}$), chief ray in image space ($\bar{\mathbf{y}}'$), marginal ray in image space ($\mathbf{y}'$), stop, and optical axis.*

$$y' = y + ut, \qquad \textit{Eq. 1-1}$$

where $y$ is the beginning ray height, $u$ is the optical angle (slope) of the ray, $t$ is the distance traversed, and $y'$ is the final ray height.

The second equation involves the change in ray angle, which is calculated by

$$n'u' = nu - y\phi, \qquad \textit{Eq. 1-2}$$

where $n$ is the index of refraction before the refracting surface, $u$ is the ray angle before, $y$ is the ray height before, $\phi$ is the power of the refracting surface, $n'$ is the index of refraction after, and $u'$ is the ray angle after. The power of a refracting surface is given by

$$\phi = \frac{n'-n}{R}, \qquad \textit{Eq. 1-3}$$

where $R$ is the radius of curvature.

These equations, while simple in form, are very powerful for determining the characteristics of an optical design. In section 1.4, a brief discussion of aberration theory will show that just the chief and marginal rays are required to understand the 4th order wavefront errors of an optical system. The 4th order wavefront equations will prove useful for understanding how to correct for the off-axis aberrations of a heliostat mirror (see Chapter 3 and Appendix A).

## 1.3 Pupil-imaging Optical Designs

The imaging of the stop, or pupil, has proven to be useful in a variety of applications: Köhler illumination, gravitational distortion correction, atmospheric correction, concentrated photovoltaics (CPV), etc. A basic layout of pupil-imaging is given in Figure 1.2.

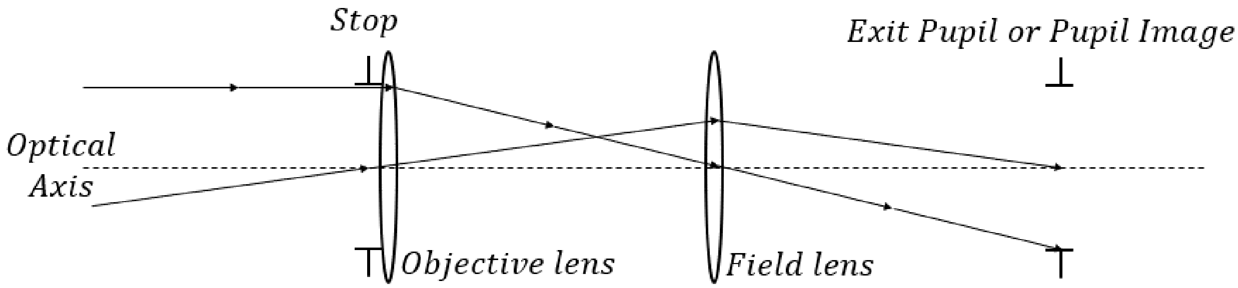

*Figure 1.2: Optical layout with objective lens focusing light onto a field lens, which in turn images the stop.*

If the object were a spatially non-uniform light source being imaged onto the field lens, the Fourier transform of the angular distribution of the object would be located at the field lens, i.e.

the spatial distribution of the object convolved with the point spread function (PSF) of the lens. The field lens is then taking this spatial distribution and applying another Fourier transform such that the angular distribution of the light source is located at the imaging conjugate of the field lens. Each point of a light source tends to emit uniformly at all angles; thus, the pupil image is a highly uniform irradiance distribution. Such is the case for Köhler illumination in microscopes [3].

Consider the motion of a refracting telescope as its pointing sweeps across the sky to view various astronomical objects. The force of gravity relative to the pointing of the telescope goes as $F = g \sin\theta$, where $\theta$ is the angle of the pointing relative to the horizon (i.e. the elevation angle) and $g \cong 9.8\, m/s^2$. With the telescope Zenith pointing there is a greater moment in the center of the lens. Thus, the shape of the objective lens is altered. To measure this change in shape an optical instrument may be placed at the focus of the telescope. With the telescope directed at a point source, an image of the primary mirror can be formed on a fly's eye array. The local slopes across the wavefront can then be measured from the spot local deviations from on-axis, and the slopes can be integrated to provide the wavefront introduced by the gravitational sag. In this scenario you have created a Shack-Hartmann wavefront sensor.

Generally, the thickness of glass of optical elements is chosen such that this gravitational effect can be considered negligible, but not always. Because this change in sag with gravity can be measured, engineers have discovered ways it can be fixed (e.g.

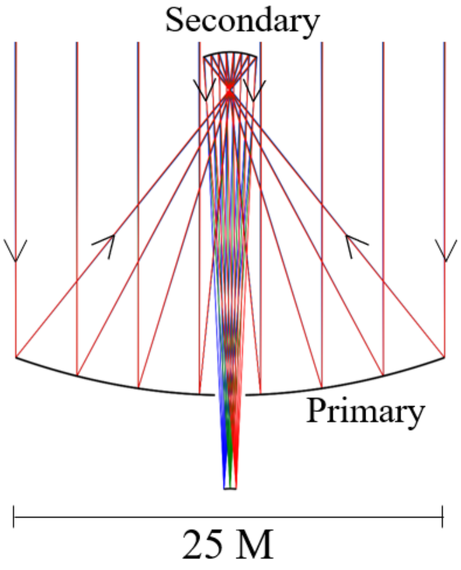

*Figure 1.3: GMT layout*

placing a deformable mirror at a pupil-image). Thus, pupil-imaging can be used in the measuring and correction of mechanically introduced aberrations.

The principle of imaging optical elements need not apply solely to the objective (stop) element of an optical system. In the case of the Giant Magellan Telescope (GMT), a Gregorian telescope design (Figure 1.3) was chosen so that the secondary mirror could be imaged by the primary mirror to ~200 m above the primary mirror (see Figure 1.4). This makes it possible to correct for phase variations introduced by the atmospheric ground layer [4]. As shown in Figure 1.4, the off-axis edge rays do not focus in the same focal plane as the on-axis edge rays, yet the atmospheric wavefront errors can still be corrected. The image of the secondary does not need to be sharp for atmospheric correction to work. This correction of the atmospheric ground layer will ideally allow the GMT to obtain 0.30 arcsec FWHM resolution images across a ~10 arcmin field of view for wavelengths >1 μm [5]. The possibility of obtaining such earth-based images with this technique sheds some light on its usefulness and power.

A further application of pupil-imaging is with concentrated solar energy, where the drive to reduce cost leads to very blurred images. When focusing sunlight in CPV applications it can be challenging to keep the spot focused on the multi-junction (MJ) cell. Any fluctuations in the geometry of the tracker due to wind or slop in the driving mechanisms causes the focal spot to shift around. To keep the spot within the MJ cell area it needs to be much smaller than the size of the cell.

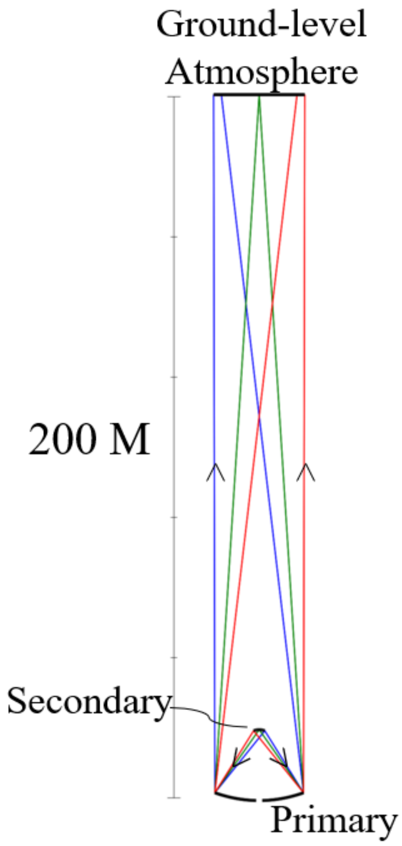

*Figure 1.4: GMT layout with the secondary mirror set as the object.*

However, this creates hot spots, which tend to degrade the performance of the cell [6]. To keep the spot from moving around, an object that is not moving relative to the MJ cell can be imaged onto the cell. In practice the stop is chosen, thus an image of the pupil is formed on the MJ cell. Placing a CPV cell at the pupil-image in Figure 1.2 illustrates this technique. Now when the tracker has fluctations in pointing the spot position on the cell does not change significantly. Additionally, because the pupil is imaged (i.e. the spot is the Fourier transform of the spatial distribution of the Sun), the spot on the cell tends to be more uniform, thus reducing the risk of hotspots.

More details on the techniques discussed in this section are found in Chapter 2. An understanding of these techiniques also helps with understanding the basic principles of both null and non-null type metrology systems. In section 1.4 this is briefly described.

## 1.4 Non-null Metrology Systems

The metrology of optical elements, mechanical components, stellar objects, etc. is performed using a variety of techniques. Mechanical or contact measurement procedures often involve coordinate measuring machines (CMM), Geneva gauges, spherometers, Faro arms, etc. Contactless measurement processes can be done in a greater number of ways: deflectometry, point source microscopes, confocal chromatic sensors, interferometry, Hartmann measurements, etc. There are only so many ways you can physically touch an object. In contrast, the number of ways an object can be optically measured is limited by the imagination of the engineer.

Optical measurement techniques can be divided into two highest level categories: non-null metrology, and null metrology. The category of the optical metrology system is determined by the answer to the following question: Is the returning light in a similar form to the outgoing light? In other words, if the light is passing through a focal point, does it return through that focal point?

Does the light return through some or all the optics used in the outgoing beam? Is the measurement absolute or relative to an ideal? If the answer is yes to any of these questions, then the type of metrology system is generally considered a null metrology system.

The quintessential example of a null metrology system is an interferometer. In a Fizeau type interferometer, light is emitted by a source and passes through optics, which often focus the light. This focused light continues (effectively acting like a point source) towards an optical component being tested, perhaps a spherical concave mirror. If the mirror is concentric with the focal point, then the light will focus back on itself and return through the optics from which the light originated. Using interference, the shape error of the optic under test can be directly measured. More details about this type of system will be discussed in Section 1.6 and Chapter 5.

Non-null metrology systems often consist of a light source and a sensor. Light from the light source is incident upon the optic under test, and the reflected or refracted light is measured by the sensor. If light is measured in reflection, a triangle is formed containing the light source, optic under test, and sensor. The angular separation of the outgoing and reflected beams is the same as the angle made between the light source and sensor with the vertex located on the optic under test (see Figure 1.5).

The angular deviation of the ray is associated with the local slope of the optic under test. In the trivial case, the slope is zero, and the light reflects upon itself. In a normal situation, the slope is non-zero, and the direction of the ray is deviated by twice the local slope. Thus, the local slope

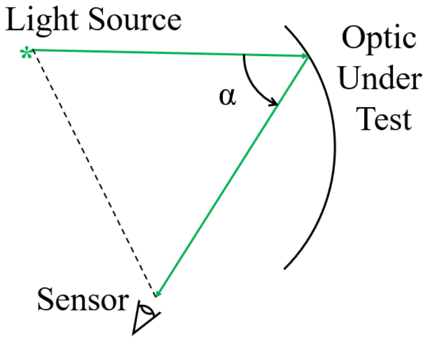

*Figure 1.5: Basic non-null metrology arrangement. Light is emitted by the source, which reflects from a known position on the optic under test. A sensor then detects the final position of the light. Together the light source, position on the optic under test, and sensor define a triangle with an angular separation, α, of the outgoing and reflected light.*

of the mirror is related to half the angular deviation of the light (i.e. $S = \tan\left(\frac{\alpha}{2}\right)$). By measuring the angular deviations of the spots across the optic under test the slope of the optic can be measured. The slope has two dimensions, thus the slope in x and y need to be measured.

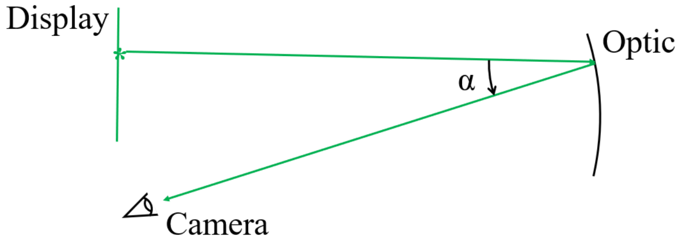

*Figure 1.6: A basic deflectometry arrangement where a Display flashes known patterns across the screen, light from the Display reflects from the Optic onto the Camera, and the Camera takes pictures of the Optic. Based on the geometry and images of the optic, the local slopes across the Optics can be measured. These slopes can then be integrated to obtain the surface shape.*

A common non-null metrology system uses deflectometry (see Figure 1.6). In phase-shifting deflectometry, millions of pixels across a television display are flashed in known patterns, which allow for individual identification of pixels [7]. This is often accomplished in ≥4 measurements, but has been done in one measurement [8]. Generally, this technique is used for measurements in reflection, but can also be done in transmission [9]. In a reflection measurement, the light from the display is reflected from an optic under test. A camera, focusing on the optic, captures images of the display patterns. From these images, individual pixels are identified, and millions of triangles are formed between the display, optic, and camera. Thus, the slope across the optic can be calculated, and by advanced integration techniques [10] the surface of the optic can be computed.

Deflectometry itself has been identified as a Hartmann test in reverse [11]. Deflectometry has enough resolution and accuracy to get the low-order and high-order figuring as well as the roughness of a surface. In contrast, the Hartmann test has a more limited resolution, which works well for measuring low-order surface figuring [12], but not high-order. A full discussion of the Hartmann test appears in Chapter 4 where a Hartmann Laser metrology system is introduced.

## 1.5 Optimization and Aberration Theory

Inherent aberrations of optical systems can be categorized based on the characteristic optical performance. Additionally, many systems are designed with a specific application in mind and situations outside the design parameters may lead to undesirable performance. For example, certain applications require a small spot size, such as for telescopes. Other applications require a well corrected wavefront with a Modulation Transfer Function (MTF) that has a high contrast at a desired spatial frequency, such as for military imaging applications. If an MTF optimized system were used to view stars there would be a noticeable loss of resolution for the system. Conversely, if a spot-size optimized system were used in low contrast imaging situations, the features of the scene would be more challenging to define.

These different optimization techniques are both driven by an understanding of the intrinsic aberrations of optical systems. To understand the spot characteristics or the wavefront departure, the aberration of an optical system needs to be broken down into its constituent parts. The fundamental optical aberrations are named spherical, coma, astigmatism, field curvature, and distortion. Other low-order terms are generally not considered in optimization except chromatic aberrations, which should be considered for refracting optical systems that require multiple wavelengths. The other low-order terms are more related to alignment: tilt, piston, and defocus. Defocus can also be used to balance aberrations. It is induced by a shift in the focal plane from the marginal ray (first order) focal point. It is used to get a better fit sphere to the focusing wavefront.

The fundamental, or 4th order, aberrations have been derived in previous texts [13]. Shown here are the results of those derivations with some introductory explanation. For the wavefront description of optical aberrations, the vector, $\vec{H}$, is the normalized field vector of the optical system. The chief ray slope multiplied by $\vec{H}$ provides the field vector. The vector, $\vec{\rho}$, is the normalized pupil vector of the optical system. The entrance pupil radius multiplied by $\vec{\rho}$ gives the pupil vector. Together, $\vec{H}$ and $\vec{\rho}$ form a basis for wavefront errors of optical systems. The normalized field and pupil vectors are defined in the plane of the entrance pupil or exit pupil. Because the vectors are normalized, the wavefront error can be defined in either. This is illustrated in Figure 1.7. These vectors can be combined by the scalar product of each with itself, or with one another. The wavefront error is not defined to have directionality, which is why the cross product is not considered. Thus, the wavefront error can be defined as

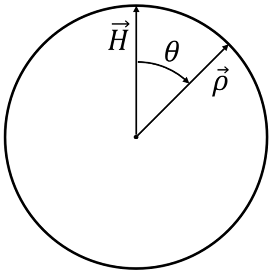

*Figure 1.7: The normalized field, $\vec{H}$, and pupil, $\vec{\rho}$, vectors located in the entrance pupil plane, separated by an angle $\theta$.*

$$W(\vec{H},\vec{\rho}) = \sum_{i=0}^{\infty}\sum_{j=0}^{\infty}\sum_{k=0}^{\infty} a_i b_j c_k \left(\vec{H}\cdot\vec{H}\right)^{i}\left(\vec{H}\cdot\vec{\rho}\,\right)^{\mathrm{j}}(\vec{\rho}\cdot\vec{\rho})^{\mathrm{k}}\,, \qquad \textit{Eq. 1-4}$$

where $a_i, b_j, c_k$ represent the coefficients for each term. This form of the wavefront function is not generally used. Instead, the wavefront function is written in the form

$$W(\vec{H},\vec{\rho}) = \sum_{i=0}^{\infty}\sum_{j=0}^{\infty}\sum_{k=0}^{\infty} a_i b_j c_k H^{2i+j}\rho^{2k+j}\cos^{\mathrm{j}}(\theta)\,,\text{ or} \qquad \textit{Eq. 1-5}$$

$$W(H,\rho,\theta) = \sum_{m=0}^{\infty}\sum_{n=0}^{\infty}\sum_{j=0}^{\infty} W_{mnj}H^{m}\rho^{n}\cos^{\mathrm{j}}(\theta)\,, \qquad \textit{Eq. 1-6}$$

where $m = 2i + j$ and $n = 2k + j$. Note, whenever $j$ is nonzero, all three terms are influenced in odd increments, whereas $i$ and $k$ only influence the field term and pupil term in even increments, respectively. Therefore, some combinations of the summations using $m$ and $n$ notation are not possible. For example, it is not possible for $m = 1$, $n = 0$, and $j = 1$, but it is possible to have $m = 1$, $n = 1$, and $j = 1$. The fourth order terms are thus defined by a combination of the field and pupil terms such that $m + n = 4$. Therefore,

$$W(\vec{H},\vec{\rho}) = W_{400}(\vec{\rho}\cdot\vec{\rho})^2 + W_{131}(\vec{H}\cdot\vec{\rho}\,)(\vec{\rho}\cdot\vec{\rho}) + W_{222}(\vec{H}\cdot\vec{\rho})^2 + W_{220}(\vec{H}\cdot\vec{H})(\vec{\rho}\cdot\vec{\rho}) + W_{311}(\vec{H}\cdot\vec{H})(\vec{H}\cdot\vec{\rho}), \text{ or} \quad \textit{Eq. 1-7}$$

$$W(H,\rho,\theta) = W_{400}\rho^4 + W_{131}H\rho^3\cos(\theta) + W_{222}H^2\rho^2\cos^2(\theta) + W_{220}H^2\rho^2 + W_{311}H^3\rho\cos(\theta) \quad \textit{Eq. 1-8}$$

is the wavefront error function where the aberration coefficients are labeled as follows: $W_{400}$ is spherical, $W_{131}$ is coma, $W_{222}$ is astigmatism, $W_{220}$ is field curvature, and $W_{311}$ is distortion. The 4th order term $W_{004}$ is not considered in this treatment because it depends solely on the field and is therefore a piston term. In other applications, such as interferometry, piston terms may not be negligible.

The value of each of the coefficients is determined by the Seidel formulas, first discovered by L. Seidel [14]. The equations can be found in “Introduction to Aberration Theory” by José Sasián in Chapter 10 [13]. These coefficients are determined solely by the slope and heights of the marginal and chief rays at each of the optical surfaces in an optical system. It is inappropriate to use these coefficients for optical designs that are not axially symmetric (i.e. off-axis designs, plane-symmetric designs, etc.). Alternative Seidel equations may be used for non-axially symmetric situations [15–17].

In regards to metrology, the Seidel aberrations can be related to the Zernike coefficients of an optical surface [18]. This analogy is useful when making corrections to wavefront. For example, a Cassegrain telescope that is Earth-bound may experience gravitational deflection in the support structure for the secondary mirror. This deflection may cause the secondary mirror to decenter from the optical axis, which introduces an on-axis coma term. Note, this system has broken axial symmetry, therefore the traditional Seidel aberrations do not adequately describe the behavior of the system. Nonetheless, the traditional Seidel aberrations can still be usefully applied. If the primary mirror were deformable, or better yet, if a deformable mirror were located at an image of the primary mirror (using some additional optical components), then introduction of the appropriate comatic term to the deformable mirror would help compensate for the wavefront error introduced by gravity. This is discussed in Chapter 6 and applied extensively in Appendix A.

## 1.6 Imaging Optical Designs

The Seidel formulas are generally used to describe the imaging characteristics of an optical system. The wavefront error (calculated by the Seidel formulas) describes the optical system spot characteristics. As written in “Introduction to Aberration Theory”, *“The normalized transverse ray error vector* $\Delta\vec{H}$*, normalized by the chief ray height* $\bar{y}_I'$ *at the Gaussian image plane, can be written to third order of approximation as*

$$\Delta\vec{H} = -\frac{1}{\text{Ж}}\vec{\nabla}_\rho W, \tag{8.3}$$

*where* Ж *is the Lagrange invariant…”* [13].

Therefore, the spot size and shape of an optical system is well described by the gradient of the wavefront error of the optical system. Meaning, a slope error in the wavefront will cause a deviation of ray slope such that when the ray travels from the exit pupil to the Gaussian image plane it is not located at the ideal Gaussian image point. Rather, it is located at a distance $\Delta\vec{y} = \vec{S}F$ from the Gaussian image point, where $\vec{S}$ is the slope error and $F$ is the distance from the Exit Pupil to the Gaussian image plane, which is usually the effective focal length. See “Field Guide to Geometrical Optics” for more information on Gaussian imaging equations [2].

Nothing new has been described in this discussion of imaging optical systems. Yet, understanding the basic principles given here is critical for understanding later materials. For example, the ideal shape of a solar imaging mirror is toroidal. This is because the off-axis aberration, astigmatism, causes significant blurring of images by a mirror. For a spherical mirror, the wavefront error introduced at off-axis angles is toroidal in shape. Therefore, an alteration in the shape of the spherical mirror to an ideal toroid leads to a correction of astigmatism and a nearly spherical wavefront is obtained (see section A.1).

Active optics is only one application for aberration theory. The ideal shapes of optical components can be precisely calculated for certain situations, using solely aberration theory. For example, the ideal shape for a lens with one surface as a conic and the other as plano depends only on the change in index of refraction (for on-axis imaging and working at one infinite conjugate). What does this mean? By making the convex surface of a plano-convex lens the ideal conic surface, spherical aberration can be perfectly corrected. This can be shown using aberration theory for aspheric caps. The contribution of an aspheric cap to the Seidel aberrations is given by $a = \kappa\phi y^4/R^2$, where $\kappa$ is the conic constant, $\phi$ is the power of the surface, $y$ is the marginal ray height, and $R$ is the radius of curvature. This value, $a$, describes all alterations to the 4th order aberrations by an aspheric cap. For spherical aberration, the change in spherical aberration by an aspheric cap is $a/8$. The spherical aberration for a conic plano-convex lens has contributions from traditional aberration theory and aspherical cap aberration theory. Thus, the spherical aberration for such a lens as shown in Figure 1.8 is given by

$$W_{040} = W_{040}^{0} + W_{040}^{Cap} = \frac{1}{8}\frac{n^2}{n'^2}\frac{\phi^3 y^4}{(n'-n)^2} + \frac{1}{8}\kappa\frac{\phi^3 y^4}{(n'-n)^2} = \frac{1}{8}\frac{\phi^3 y^4}{(n'-n)^2}\left(\frac{n^2}{n'^2} + \kappa\right), \tag*{Eq. 1-9}$$

which shows that to perfectly correct spherical aberration, set the conic constant

$$\kappa = -n^2/n'^2, \qquad \text{Eq. 1-10}$$

where $n$ is the refractive index in object space and $n'$ is the refractive index in image space.

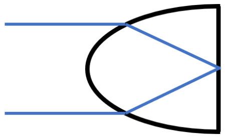

*Figure 1.8: A lens with refractive index, n, and conic constant, κ, such that the on-axis imaging is perfectly corrected.*

This is a powerful discovery of aberration theory. One application of this equation is found in injection molded plastics for LEDs. LEDs are often used in electronics as feedback for users, or back-lighting of interactive components. In order to create high visibility of the LED from desired viewing angles, the LED is often placed at the focal position of a lens like that shown in Figure 1.8. Since LEDs are small, the light emitted is reasonably collimated and sends more of the light in the intended direction (towards the eye of the user).

Another application is found in a potential design for the Breakthrough Starshot laser projector. The Breakthrough Starshot Initiative has a goal to send a small spacecraft to Alpha Centauri at 20% of the speed of light [19]. The basic idea involves a multi-kilometer array of lasers that are all phased directing a ~100 GW beam at a "light-sail" in space. In the space of several minutes the light-sail spacecraft is accelerated to $0.2 \times c$. In order to get the desired diffraction-limited spot on the light-sail the full aperture must be well filled and uniform [20].

A potential solution to the optical challenge is to create a series of rafts composed of lenslet arrays. Each lenslet is about 8" in diameter (the size of r0 for ideal atmospheric conditions). Behind each lenslet is a diverging lens placed in front of a laser. Together the diverging lens and the focusing lenslet comprise a beam expander. A less expensive solution to this problem would be to have the lenslet plano-convex with the convex side towards the light-sail (see Figure 1.9). In this arrangement, the convex side can be spherical, which makes the lenslet array less expensive. The potential issue with this arrangement has long been an issue for heliostat mirrors: soiling.

When being used, this laser array is exposed to the elements, thus soiling of the optics must be considered. Cleaning out the crevices between adjacent lenslets may prove to be time-consuming and expensive. It would be better if the plano side of the lenslet array were exposed to the elements, but this is not favorable for a plano-convex lens. According to aberration theory, the convex side of a spherical plano-convex lens should be directed towards the infinite conjugate. This minimizes spherical aberration. However, if the convex surface of the lens is a conic of any choice the lens can actually face whichever direction is most convenient for the application, according to Eq. 1-10.

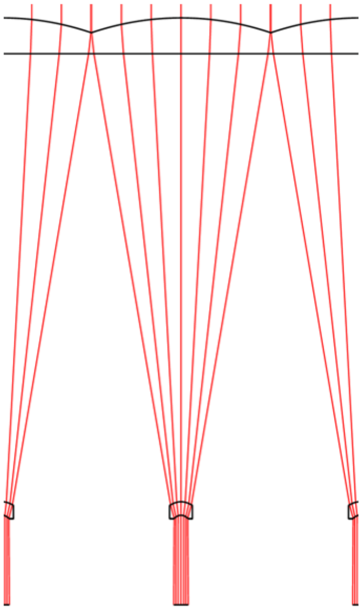

*Figure 1.9: Potential beam expander for Breakthrough Starshot laser array raft.*

So, we can have our cake and eat it too if we allow the convex surface to be a conic and direct it towards the laser. The major caveat is of course the lenslet array is much more challenging to manufacture. However, if a manufacturing process were adopted as suggested in US Patent Application No. 62/905,824, then this could prove to be a viable approach.

Knowing that there exists a solution with the plano side towards an infinite conjugate, Zemax OpticStudio can be used to find the solution. One other optimization parameter must be considered though, the beam shape output by a typical laser is gaussian. Expanding a gaussian-shaped beam will result in a gaussian output, which will significantly reduce the uniformity of the output beam, thus more light will be diffracted outside the airy-disk. A reasonably uniform output can be obtained by vignetting the outer parts of the beam and leaving only the relatively flat center, but this reduces the overall output from each lenslet. The additional optimization goal is then to change the beam from a gaussian input to a uniform (or flat-top) output. With the merit function properly established, optimization in Zemax OpticStudio leads to the design shown in Figure 1.10. The convex surface of the lenslet is an even asphere with a conic constant of -2.58. Assuming an index of refraction of glass of 1.5, the conic constant should be near -2.25 (hyperbolic) to minimize spherical aberration, so the optimized solution is very close to the prediction. The discrepancy is likely due to the additional requirement of changing the beam from gaussian to uniform and the balancing of spherical aberration between the lenslet and the diverging lens.

Additional changes to this design could involve a local change in tilt by displacing the diverging lens. This would allow for correction of atmospheric wavefront errors. Additionally, a beam splitter would need to be introduced either before or after the diverging lens so that these optics could also be used for wavefront sensing of the atmosphere. By no means is this a complete design for what is required of the Breakthrough Starshot laser projector, but it provides a direction to pursue, and shows the usefulness of aberration theory in guiding solutions towards a solution that satisfies system requirements.

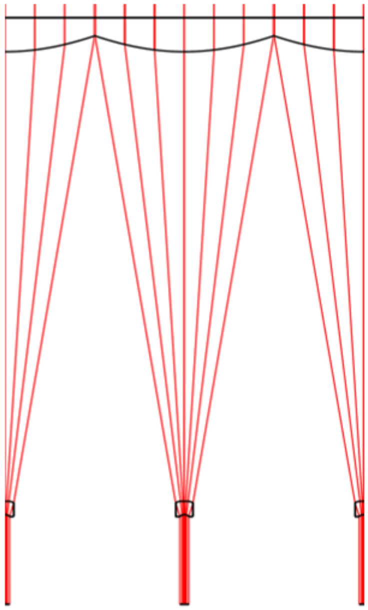

*Figure 1.10: Beam expander for Starshot laser array using an even aspheric convex surface for the lenslet.*

## 1.7 Null Metrology Systems

As discussed in section 1.3, if the returning light in a metrology system is in a similar form to the outgoing light, then the system can be categorized as a null metrology system. This definition is not accurate for many null metrology arrangements. In this section null metrology is defined more completely. Null metrology is generally associated with interferometry where a reference beam and test beam are overlapped resulting in a fringe pattern, which shows the difference in optical path (OPD) between the two beams. Fringe patterns are well described by

$$I(x,y) = I_1 + I_2 + 2\sqrt{I_1 I_2}\cos\big(\phi(x,y)\big), \qquad \text{Eq. 1-11}$$

where $I_1$ and $I_2$ are the two different beam nominal irradiances, $I(x,y)$ is the irradiance of the fringe pattern at a given $x, y$ position on the optic under test, and $\phi(x,y)$ is the phase difference between the two different beams. Note, the phase difference only depends on the position in the pupil of the optic under test.

In the past, interferometry has required tilt fringes to be present so that optical path differences can be measured by deviations of the fringe pattern from straight lines (see Figure 1.11). For a double-pass configuration, a quarter wave error (at 633 nm wavelength) would be associated with an eighth of a wave of surface height error, or about 80 nm. In contrast, phase-shifting interferometry has allowed for much higher accuracy in surface height errors in a fraction of the time.

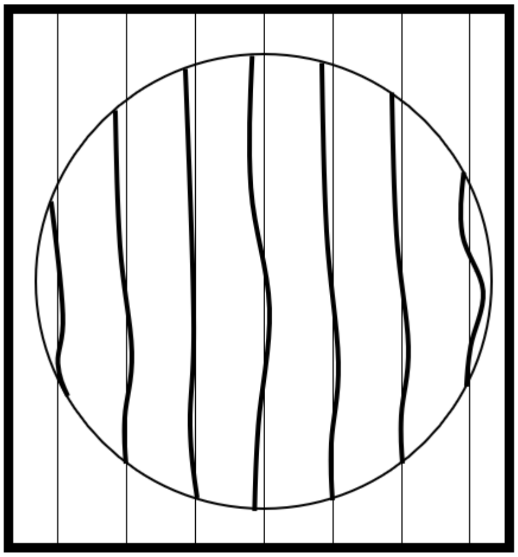

*Figure 1.11: Typical fringe pattern for a classical interferogram. The circular region with slightly wavy lines is the interferogram. The square box with the straight lines is used as a precise reference to observe the deviation of the fringes from straight lines. These deviations represent the optical path difference introduced by the optic under test (i.e. the surface height error).*

Phase-shifting interferometry has often been accomplished by inducing 90-degree phase shifts to one of the interfering beams, usually the reference beam. In Eq. 1-11, there are three unknowns, therefore at least three independent measurements are required to obtain the phase map across the surface of the optic under test. In practice, at least four measurements are obtained due to errors in phase stepping [21] and other sources of error [22,23].

Phase stepping is often accomplished by changing the optical path length of the reference beam by mechanical motion of the reference reflecting surface. Using 90-degree phase shifts, the well-known four-bucket algorithm can be derived to calculate the phase. The four different measurements are of the form:

$$I_1(x,y) = I_{DC} + I_{MOD}\cos\big(\phi(x,y)\big), \qquad \textit{Eq. 1-12}$$

$$I_2(x,y) = I_{DC} + I_{MOD}\cos\left(\phi(x,y) + \frac{\pi}{2}\right) = I_{DC} - I_{MOD}\sin\big(\phi(x,y)\big), \qquad \textit{Eq. 1-13}$$

$$I_3(x,y) = I_{DC} + I_{MOD}\cos(\phi(x,y) + \pi) = I_{DC} - I_{MOD}\cos\big(\phi(x,y)\big), \qquad \textit{Eq. 1-14}$$

$$I_4(x,y) = I_{DC} + I_{MOD}\cos\left(\phi(x,y) + \frac{3\pi}{2}\right) = I_{DC} + I_{MOD}\sin\big(\phi(x,y)\big), \qquad \textit{Eq. 1-15}$$

where $I_{DC} = I_1 + I_2$ and $I_{MOD} = 2\sqrt{I_1 I_2}$.

Combination of these four equations leads to

$$\phi(x,y) = \operatorname{atan}\left(\frac{I_4(x,y) - I_2(x,y)}{I_1(x,y) - I_3(x,y)}\right), \qquad \textit{Eq. 1-16}$$

which shows that the phase difference across the optic under test can be obtained without comparison of the fringe pattern to regularly spaced lines. In other words, tilt fringes are not required to obtain the phase, therefore the two beams can be aligned such that they form a null fringe pattern.

This type of measurement is only considered a null measurement if the optic under test returns the beam in a similar form to the reference beam (flat or spherical). Interferometers tend to output a spherically shaped wavefront; therefore, only spherical surfaces will return a null. However, if other optical components are placed in the beam path, aspheric surfaces can also be measured with a null test.

For example, an F/2 parabolic mirror can have large aspheric departure. A spherical wavefront input from an interferometer will be returned with significant spherical aberration. For a 400 mm F/2 paraboloid the aspheric departure is 0.40 mm, or ~600 waves. The mirror is tested in double pass; therefore, the interferometer would be attempting to measure ~1200 waves of OPD across the mirror. The number of camera pixels required to measure this is very large.

At the edge of the mirror, the slope departure is 8 mrad, which results in 16 mrad of ray deviation from spherical. Due to phase unwrapping requirements, the difference between adjacent pixels cannot be greater than $2\pi$ or there is ambiguity in the measurement. Thus, the ray slope deviation multiplied by the mapped pixel size must be less than one wave. In other words, the mapped pixel size on the optic under test must be smaller than $\lambda/Slope_{deviation}$, which is about 40 μm. This means >10,000 pixels in one dimension are required to avoid ambiguity in phase-unwrapping! Therefore, additional optics must be introduced to measure this mirror with an interferometer. A very useful trick for discovering the required optics for a null test is to trace the rays in reverse, forcing the rays to leave the surface under test at normal incidence. A departure from reality is required to accomplish this. By Snell's law

$$n_1 \sin(\theta_1) = n_2 \sin(\theta_2), \qquad \textit{Eq. 1-17}$$

with $n_1$ and $n_2$ as the indices of refraction before and after the refracting surface, and $\theta_1$ and $\theta_2$ the angle of incidence/exitance (relative to the surface normal) before and after the refracting surface, respectively. To obtain an angle of exitance that is normal to the surface, set $\theta_2 = 0°$.

Because the angles of incidence cannot all be 0, it must be that $n_1 = 0$. This is not physically possible, but it can still be done in ray tracing software, and it significantly reduces the time required to design corrective optics.

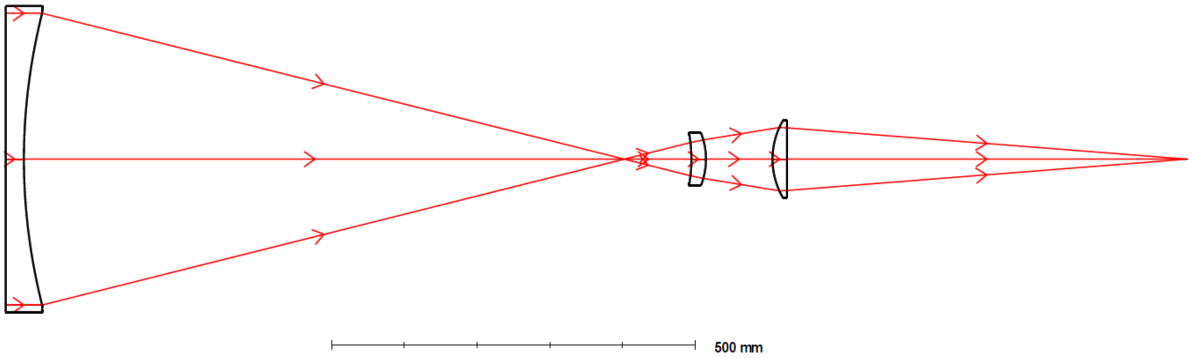

*Figure 1.12: Optical layout for null-corrective optics of an F/2 400 mm paraboloidal mirror. Rays are traced in reverse; thus, the resulting wavefront errors are half of what they would be in a real test.*

Using this ray tracing technique in Zemax OpticStudio®, a design for null corrective optics is readily attainable. An object is placed at infinity where the index of refraction until the surface under test is 0. Incidence upon the paraboloidal surface leads to refraction where all rays exit at normal incidence. A field-like meniscus lens is placed near the focus of the mirror and redistributes the rays onto a second plano-convex focusing lens, which counteracts the spherical aberration of

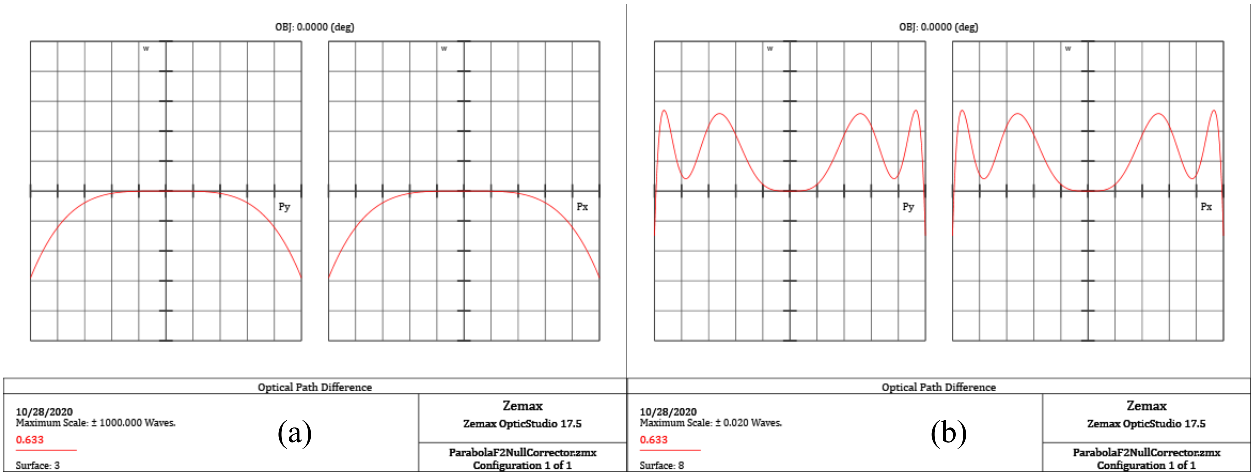

*Figure 1.13: wavefront errors for a paraboloidal F/2 mirror under test at (a) paraxial focus of the mirror and (b) paraxial focus after the focusing lens. Both wavefront errors are half of what they would be in a real testing configuration.*

the mirror and refocuses the light to a diffraction limited spot (see Figure 1.12). The wavefront error at the paraxial focus of the mirror is 581 waves PV. After the corrective optics the wavefront error is reduced to 1/100th of a wave PV (see Figure 1.13).

Both lenses are composed of N-BK7 and are less than 4” in diameter. Also, they both have spherical surfaces. Additional optimization could lead to smaller lenses, and ghost reflections may need to be examined, but this example illustrates how null testing can still be done for aspherical optics. More complicated corrective optics are required for specialized optics, such as gull-wing lenses found in cellphones. Introduction of computer-generated holograms (CGH) is often necessary to make the appropriate wavefront corrections. However, the principles illustrated here are applicable to a wide range of optical components.

## 1.8 Conclusion

In the coming chapters, the concepts discussed in Chapter 1 will be used in the exploration of designs and experimental results. All subjects rely upon an understanding of geometric optics, including imaging an object and imaging a pupil. Aberration theory is used to explain different optical design choices or metrology measurements, and a variety of other topics of the optical sciences are used in explaining the various designs and metrology techniques.

Chapter 2 is a presentation of a collection of concentrated photovoltaics (CPV) designs. Each design is intended to explore the different benefits provided by different approaches, especially the cost. Chapter 3 introduces concentration solar power (CSP). It is a chapter intended to provide motivation for using actively focused heliostats. Chapter 4 explores the mechanical and optical requirements for an actively focused heliostat. An experiment funded by Tech Launch Arizona is presented, which involved the manufacture of a prototype actively focusing heliostat and a unique metrology system for determining the heliostat shape. In Chapter 5 there is a deeper dive into null metrology systems, specifically for a unique 1.6 m diameter gull-wing lens. Additionally, a local curvature metrology system is proposed, which could enable full 3D measurements of free form surfaces without the need for interchanging optical components (i.e. switching out null corrector elements). Chapter 6 is like Chapter 2 in that it is a presentation of a collection of different telescope designs. The motivation for the telescope designs are not emphasized, though they are given in brief detail with some reference to published papers that provide more background.

Collectively the chapters of this dissertation show the various ways that the principles taught within the optical sciences can be applied to a large variety of scenarios. Solar concentration and telescopes are just two small areas in the world of optics, though there is much to say about both topics, especially when optical design and metrology are both considered.

# CHAPTER 2 : CONCENTRATED PHOTOVOLTAICS (CPV) DESIGNS

## 2.1 Introduction

Potential cost savings are the driving force for research and development of multi-junction (MJ) solar cells. Silicon cells have reached a conversion efficiency of over 25% sunlight to electricity [24]. In contrast, MJ cells have achieved conversion efficiencies of greater than 47% [25]. This increased efficiency of MJ cells is offset by the increased complexity to manufacture such a cell. A typical silicon solar cell is approximately $1/Watt whereas a multi-junction cell is around $300/Watt [26]. If that were the end of the discussion, then the conclusion would be to stick with silicon. Except perhaps in space applications where the cost of energy per weight make MJ cells more attractive. However, it is not just space where multi-junction cells have the potential to reduce cost.

Multi-junction cells are often called concentrated photovoltaic (CPV) cells. This is because many MJ cells have been designed such that ideal operating conditions are at greater than nominal Earth insolation. Many cells operate best at >100X solar concentration. This is accomplished by introduction of refracting and/or reflecting elements to concentrate sunlight onto the cells. At 300X concentration the CPV cell achieves a similar cost to a silicon cell for the same energy conversion. However, there is added complexity required for a CPV cell that is not required for a silicon cell. A CPV cell needs to track the sun in two dimensions. Otherwise sunlight will not be focused onto the cell. Additionally, the localized heating by concentration needs to be well dissipated or the efficiency of the cell is reduced [27]. Therefore, achieving just 300X concentration of sunlight is not enough to offset the cost disparity between silicon and multi-junction cells. Greater concentrations are required for modern CPV cells to compete.

## 2.2 Solar Concentration at 1000X

Achieving 1000X concentration reduces the cost of CPV cells to about 1/3 of a silicon cell. Therefore, this seems a worthy optical design goal. A recent paper by Hyatt *et al.* reports the results of a prototype design which achieved 500X concentration [28]. They obtained this concentration by using a dish collector mirror in the form of an off-axis paraboloid followed by a field lens near the focus, which concentrated sunlight at ~30X onto a fly's eye lens array. The field lens had the function of imaging the collector mirror onto the lens array. The lens array then divided the sunlight into equal portions and further concentrated onto a dome lens, which reimaged the pupil image onto the CPV cell at 500X (see Figure 2.1).

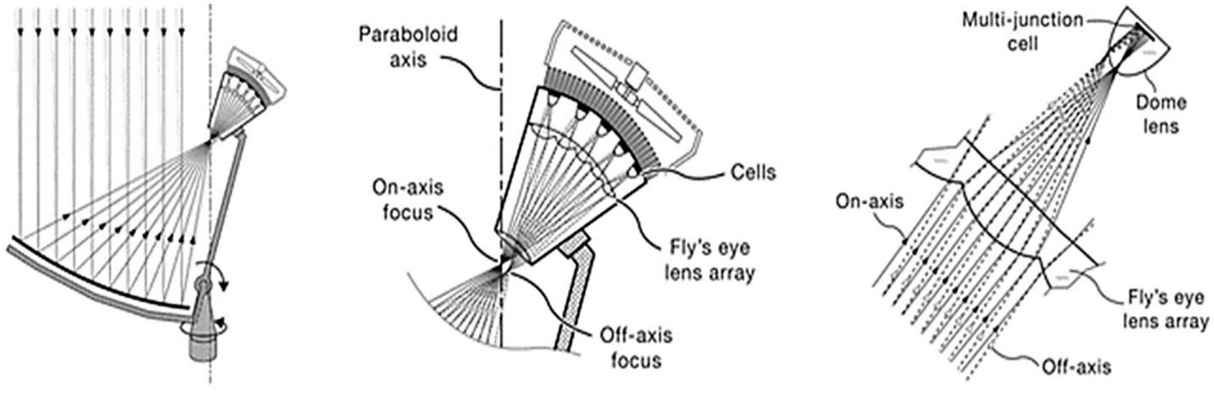

*Figure 2.1: Figure 1 from Hyatt et al.'s paper showing their optical design. The off axis paraboloidal dish collector concentrates sunlight just before a field lens (left), which images the pupil onto a fly's eye lens array (middle). The fly's eye lens array then divides the sunlight into equal amounts and further concentrates onto a dome lens, which reimages the pupil image onto the multi-junction cell (right).*

Beginning with this heritage, another design was developed for a reduction of mechanical complexity of the design by Hyatt *et al*. The design takes advantage of symmetry to reduce the number of unique components for manufacture. Additionally, a higher mispointing tolerance is obtained. This design was reported in a follow-up paper by Eads, Hyatt, and Angel, entitled “Optical Design for a Fly’s Eye CPV System with Large, On-axis Dish Solar Concentrator” (included in Appendix D) [29].

The goal of the design was to achieve a higher level of uniformity while pushing towards a geometric concentration of 1000X. The design process involved the creation of a custom merit function where minimization of the merit function occurred when the different field angles from the same pupil position imaged to the same position on the fly’s eye array (i.e. pupil imaging). Creation of such a merit function is a simple process. The following is an outline for how to do this.

Zemax OpticStudio will automatically generate a default merit function based on a variety of criteria: Image Quality, Type, Reference, Distortion, Pupil Integration, etc. The dish shaped reflector was chosen to be square for more simple division of the pupil into equal areas. Therefore, set the pupil integration to a rectangular array in the Optimization Wizard. The number of rays should be chosen to be larger than the number of divisions of the pupil, which in this design was 100 equal areas, or a 10 X 10 grid. A sampling of 40 X 40 should be suitable. Check the box for delete vignetted, set the image quality to be spot, and do not assume axial symmetry. Click apply and a merit function will be automatically generated. Copy and paste the merit function into an excel spreadsheet for further modification.

In excel, sort the rows by type so all the TRCX operands are grouped together followed by the TRCY operands. Replace all the TRCX and TRCY operands with the REAX and REAY operands, respectively. Using REAX and REAY will ensure rays are more accurately traced to the correct location (at the cost of time to optimize). Set the REAX targets to be the desired pupil

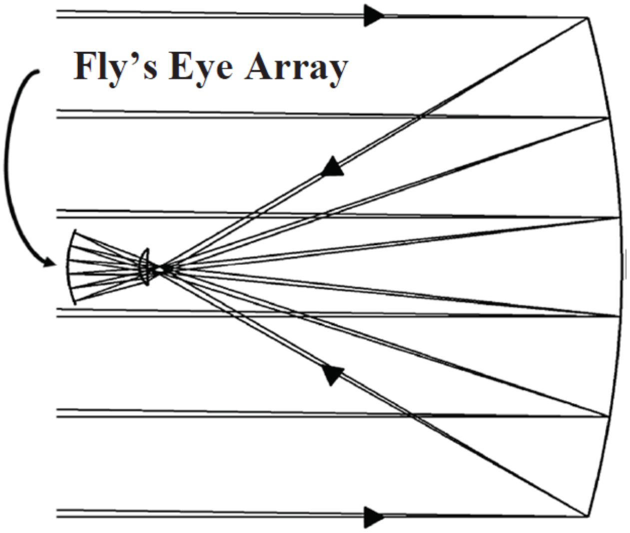

*Figure 2.2: Optical layout of design by Eads, Hyatt, and Angel in Figure 2 of their paper.*

image radius times the normalized x pupil coordinate (Px). Set the REAY targets to be the desired pupil image radius times the normalized y pupil coordinate (Py). Change all elements of the surface number column to imaging surface number (the column after the operand name). Note, the sign of the targets may need to be changed due to an inverted pupil image. Highlight the default operands in Zemax OpticStudio. Copy and paste the excel modified operands over the default operands in Zemax OpticStudio, and the design should be ready for pupil image optimization. If optimization is slow the sampling may need to be reduced. A chief ray height solve on the last surface may prove to be useful.

Using a merit function of this nature, the design by Eads, Hyatt and Angel was obtained. Optimization occurred at three different field angles: 0, 0.5, and 0.75 degrees. Wavelengths ranged from the optical to the near infrared. The size of the field lens was kept as small as possible to reduce weight and cost (see Figure 2.2).

The secondary stage concentration optics were designed using a similar merit function. These optics consisted of a fly's eye lenslet and a dome-shaped field lens (Figure 2.3). The optimized design was only required for the on-axis fly's eye. From the optimized design all other optical designs were obtained by variation of the fly's eye lenslet power, and the spacing between the lenslet and dome lens. These variations were determined by equations provided in Eads, Hyatt,

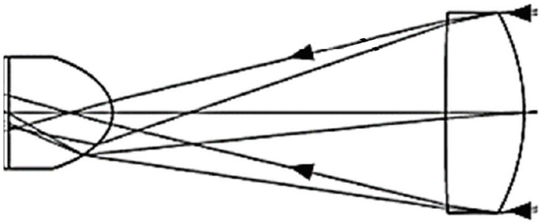

*Figure 2.3: Secondary concentration optics consisting of a fly's eye lenslet and dome-shape field lens for final imaging of pupil onto CPV cell.*

and Angel's paper [29]. The primary stage optics focus a pupil image onto the fly's eye array at ~35X concentration. The secondary stage optics concentrate the sunlight to a further ~1000X onto 5.4 mm size CPV cells.

The goal of this design was to achieve 1000X concentration so that the cost of solar cells is significantly reduced. Additionally, the cost of materials for the mirror and solar module is about the same since silicon solar cells are generally covered by glass for protection. The cost of dual-axis tracking is a significant factor that reduces cost benefits from concentration, but the greater challenge is the alignment of these optical components. In this design, there are 96 dome lenses that need to be properly centered on 96 CPV cells and then aligned to the 96-lens fly's eye array. The manufacturing of the fly's eye lens array may involve precision glass molding of four 4x6 arrays that each need to be aligned to one another and positioned relative to the field lens. Also, without proper AR coatings the dielectric losses reduce the concentration. In this design, the push for 1000X concentration led to the use of multiple optics, but this added a significant amount of complexity.

With an application of modern manufacturing techniques, the cost of these modules would approach the materials cost. Therefore, this design is still worth consideration. However, significant investment would be required to reach cost goals. Additionally, a low-cost, rapid alignment metrology would need to be implemented to verify correct manufacture of each module. Perhaps a lower concentration, yet simpler design, is a better option.

## 2.3 CPV at 300X Versus Silicon

Creating a CPV system with 300X concentration would place the cost of cells per watt at roughly the same as silicon solar. Thus, there appears to be no great advantage in creating a CPV system. However, silicon has the current advantage of mass production reduced cost. If CPV cells were produced at a similar level to silicon, then the cost per watt would be reduced, and CPV cells would be far more competitive. However, there is still the issue of the requirement for dual axis tracking in CPV applications.

Silicon solar cells do not see a great advantage in dual-axis tracking of the sun. However, single-axis tracking shows a significant improvement over a fixed tilted solar panel. A fixed tilted solar panel can receive about 6.5 kWh/m$^2$/day in Tucson, Arizona (see "Solar Radiation Data Manual for Flat-Plate and Concentrating Collectors" [30]). For single axis tracking the average yearly incident energy is 8.1 kWh/m$^2$/day. At the University of Arizona Tech Park, single-axis tracking is used to gain this 25% boost in produced energy (see Figure 2.4). In contrast, dual-axis tracking obtains only an 11% increase over single-axis tracking, which equates to 9.0 kWh/m$^2$/day. Single axis tracking mechanisms can be created in long strips, which reduces the mechanical

*Figure 2.4: Single-axis tracking solar panels at the University of Arizona Tech Park in Tucson, Arizona.*

complexity and cost. Dual axis tracking mechanisms require a separation of modules, and of course the added complexity of another axis of rotation.

Dual-axis tracking for silicon solar panels does not add much advantage. However, dual-axis tracking with CPV cells does show an advantage over silicon solar panels. Of the 9.0 $kWh/m^2/day$ that are collected with dual-axis tracking, 7.0 $kWh/m^2/day$ are the direct solar component, which is the only part that CPV cells use (the other 2.0 $kWh/m^2/day$ are the diffuse sky component). This is less than the 8.1 $kWh/m^2/day$ collected and used by a single axis tracking solar panel. However, the conversion efficiency of both cell types must be considered in both applications.

Commercial silicon solar cells have conversion efficiencies close to 20%. In contrast, commercial CPV cells have conversion efficiencies >40% (at operating temperatures). If well designed AR coatings are used on optical components, then the expected system conversion efficiency is reasonably 40%. This means that for single axis tracking silicon solar panels, the expected yearly average energy production is about 1.6 $kWh/m^2/day$. Using dual-axis tracking with CPV cells the expected energy production from the direct solar component is 2.8 $kWh/m^2/day$, a 75% increase over single axis tracking silicon solar panels. Clearly in Tucson, Arizona CPV cells show a great improvement in conversion efficiency of sunlight, perhaps enough to offset the added cost in dual-axis tracking. But in other parts of the USA the efficiency gains in CPV are not so significant.

In Seattle, Washington the yearly averaged collected energy for a single-axis tracking system is 4.3 $kWh/m^2/day$. The collected energy for dual-axis tracking is 4.9 $kWh/m^2/day$ with 2.9 $kWh/m^2/day$ being direct. Therefore, a single-axis tracking silicon PV panel predicted energy production averaged over a year is 0.9 kWh/m$^2$/day. A dual-axis tracking CPV system has a predicted energy of 1.2 kWh/m$^2$/day. The energy gain is only about 33%. An energy gain of this amount may be sufficient for the switch from fixed tilted silicon PV to single-axis tracking silicon PV, but the required switch from single-axis tracking to dual axis-tracking makes silicon PV more cost-effective than CPV in regions of the world like Seattle, and silicon PV in Seattle isn't that cost-effective anyway. So far, the decision has appeared to be either silicon PV or CPV, but what if the decision is not just between silicon PV and CPV? What if both technologies could be used together? Yunus Emre once said "Come let us be friends for once." Perhaps by combination of these two technologies there can be a greater gain than using only one. A different type of design would need to be studied. What is the efficiency gain made possible?

If all the direct sunlight were used by CPV and the remaining diffuse component collected by silicon PV, then the overall system efficiency is improved. In Tucson, Arizona the predicted energy production would be 3.2 kWh/m$^2$/day, twice that of single-axis tracking silicon PV! In Seattle, Washington the predicted energy production would be 1.6 kWh/m$^2$/day, over 75% more than single-axis tracking silicon PV! Of course, the cost per energy of such a system in Seattle would be twice that of Tucson.

The potential gain in solar conversion appears to offset by the increased cost per watt though. The cost of the cells is approximately doubled since both 300X concentration CPV cells and silicon PV cells are used. However, other effects may change this loss. If more CPV cells were manufactured, then the cost would be driven down. There wouldn't necessarily be a 100% improvement on cost per watt, but there would still be improvement. The major obstacle would then be a low-cost dual-axis tracker.

## 2.4 Ideal Hybrid Design

The use of silicon and CPV cells together involves a different way of thinking about solar concentration than shown in section 2.2. The geometry makes it challenging to use both the diffuse and direct component of sunlight with a reflective system, thus a transmissive system is more appropriate. For silicon solar panels a 4 mm protective glass layer is typically placed over the top of the silicon cells. Perhaps this glass layer could be switched out with a focusing element? It would need to be a collection of focusing elements to keep the thickness close to 4 mm, which means it would need to be a fly's eye lenslet array. Then of course there would need to be another focusing element behind each lenslet so that a pupil image could be formed on the CPV cells, thus ensuring mispointing is well tolerated while keeping local concentrations below ~1000X (i.e. no hotspots).

There is also the question of maintaining the panel (e.g. keeping the glass clean). If curvature is placed on the front surface of the glass, then grooves are exposed to the elements and it may be challenging to clean out collected dust and grime. Yet it is ideal for the front surface to have curvature so that spherical aberration of the objective is minimized. Unless the lenslet array were composed of plano-convex lenses with the convex surface being aspheric. Then the front surface could be flat and the back surface hyperbolic and spherical aberration would be well corrected.

Using a similar merit function as introduced in section 2.2, and following the parameters described above, an optical design for ~300X concentration was found (see Figure 2.5). A 1" square plano-convex objective element focuses light onto a dome lens, which images the objective

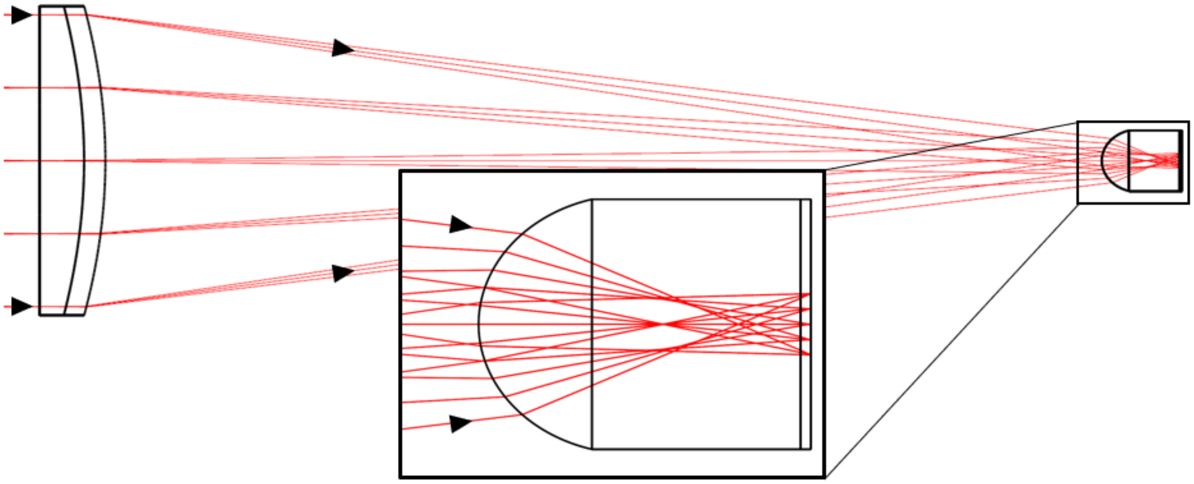

*Figure 2.5: Optical design for hybrid CPV application. The objective element is a 1" square plano-convex lens with the convex surface hyperbolic. The secondary element is an elliptical dome lens, which images the objective element onto the CPV cell at 300X concentration. Angles depicted are on-axis and +/- 0.75°.*

onto a 1.5 mm square CPV cell (i.e. 287X geometric concentration). The aperture size and thickness of the objective is chosen such that the average thickness is 4.2 mm (near the 4 mm thickness used in standard silicon PV panels). The glass chosen is N-BK7 due to its availability, but this design could easily be reoptimized to accommodate a cheaper low-iron float glass.

The distance from the glass plate to the CPV cell is kept less than 100 mm so the cost of the panel housing is not significantly increased. The conic constant of the convex surface is -2.295 ($\kappa = -n^2 = -1.515^2$) so that an interferometric null test could be used to measure each of the lenslets using a HeNe laser (see Figure 2.6). This provides more surface information and accuracy than what is generally needed for solar concentration, but the test is quite simple. The measurement would be performed in a double pass configuration with the light focusing from a Fizeau interferometer in front of the convex surface, refracting at the convex surface and reflecting from the flat back surface of the lenslet. The convex surface collimates the light, thus the second pass

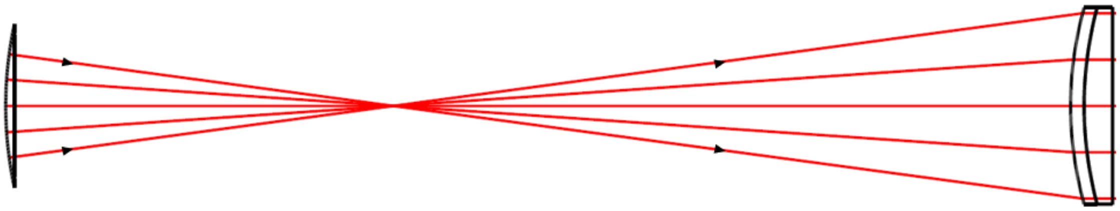

*Figure 2.6: Double pass testing configuration of hyperbolic convex surface. Light is focused by a Fizeau interferometer in front of the convex surface. The diverging light is collimated upon refraction by the hyperbolic surface and reflects from the flat back surface (dielectric reflection). The contrast of the fringes observed would not be noticeably affected by dielectric reflections from the convex surface.*

through the objective brings the light back through the same focus. Stray light reflected by the convex surface is diverged and is therefore negligible.

The optimization was performed for 0°, 0.5°, and 0.75° for wavelengths 400 nm, 633 nm, 1.0 µm, and 1.6 µm. The pupil imaging is achromatically blurred by about +/- 2.5%, meaning the size of each pupil image is similar within +/- 2.5% in diameter, or about +/- 5% in area. This leads to a highly uniform spot spread across the CPV cell, which is desirable [6]. The size of the spot is kept to about a 1.3 mm square to allow for misalignment errors of the CPV cell up to +/- 0.1 mm in manufacturing. Pupil images for solar disk angular positions of on-axis, 0.75° off-axis and 1.39° off-axis are provided in Figure 2.7. The optimization was only out to 0.75°, which is why a slight vignetting begins to occur for a solar disk position of 0.75°. Surprisingly, the vignetting does not reach >20% until the solar disk is 1.39° off-axis. Thus, the solar disk acceptance angle is nearly 2.8° before the relative total illumination drops below 80%! A quick look at the transmittance of an array of such lenses (in non-sequential mode of OpticStudio) shows that 9.4% of the light entering the array does not make it due to TIR. This is for angles ranging from 1.5 to 89.5 degrees, weighted by their cosine factors. Thus, most of the diffuse light is converted to electricity by the silicon.

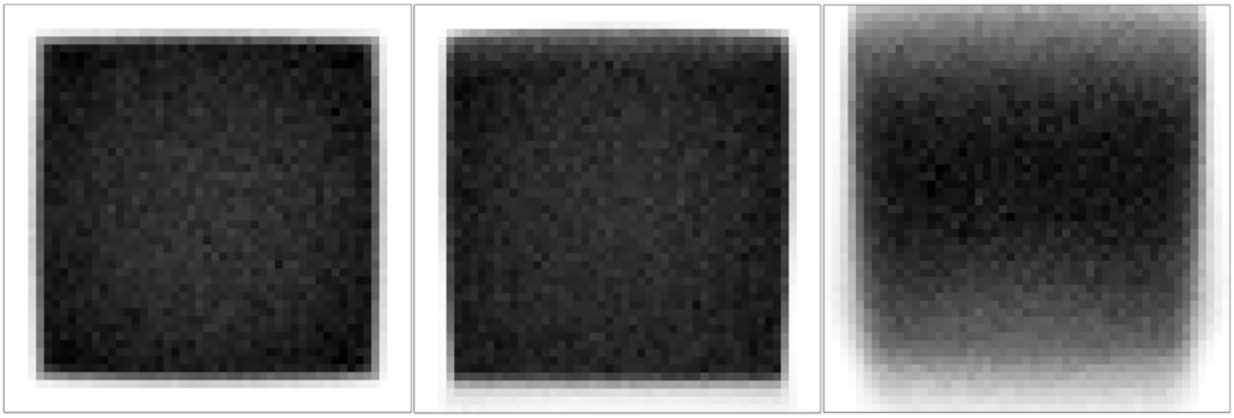

On-Axis Sun
100%

0.75° Off-Axis Sun
99.8%

1.39° Off-Axis Sun
79.7%

*Figure 2.7: Pupil images formed on a 1.5 mm square CPV cell beginning with on-axis sun (i.e. +/- 0.25° solar disk object) on the left and further off-axis positions towards the right. Total relative illumination is provided showing that performance of the optical system does not deteriorate to below 80% until the solar disk is located 1.39° off-axis.*

The main issue with this design is of course the use of aspheric surfaces (see the optical prescription in Table 2-1). However, in high volume the aspheric dome lenses could be injection molded at a cost similar to the cost of materials. The aspheric lenslet array is a more significant element. The cost could be quite significant, but recent ideas about the creation of such an array may allow for such a monolithic optic to be manufactured.

*Table 2-1: Optical prescription for the design shown in Figure 2.5. SYLGARD-184 would be used to glue the dome-lens onto the CPV cell for ideal optical contacting.*

| Radius | Thickness | Material | Semi-Diameter | Conic |
|---|---|---|---|---|
| Infinity | 5.400 | N-BK7 | 17.961 | 0.000 |
| -45.000 | 81.855 | AIR | 17.961 | -2.295 |
| 2.175 | 6.381 | N-BK7 | 2.485 | -0.288 |
| Infinity | 0.200 | SYLGARD-184 | 2.485 | 0.000 |

The recently filed patent, U.S. Provisional Application No. 62/905,824, entitled “APPARATUS AND METHOD FOR THE MANUFACTURE OF LARGE GLASS LENS ARRAYS” describes a method that could be implemented on a float glass manufacturing line.

Localized regions of high and low air pressure would be exerted on the top surface of float-glass as it moves along a bath of liquid tin. This is accomplished by "blowing" and "sucking" on the top surface in such a way that certain regions of liquid glass are raised, and other regions are depressed. In this manner a large "quilted" pattern of lenslets could be formed with virtually no added time in the manufacture of the glass sheet. Using this method, many types of surfaces could be imprinted on a glass sheet with the top surface having the desired pattern and the bottom surface obtaining the high precision flatness that naturally occurs in float-glass manufacturing.

## 2.5 Off the Shelf Hybrid Design

Until such a manufacturing process is implemented, a cheaper design to illustrate the performance of a hybrid system is needed. To reduce the cost of a prototype system, aspheric surfaces should not be used. The benefits of keeping the flat surface facing outward are still attractive, but the spherical aberration is too damaging when using solely spherical surfaces. Thus, for the following design the plano-convex objective was placed with the convex surface facing outward to minimize spherical aberration. A ball lens was chosen because of its cheap cost (especially if mass-produced soda-lime balls are used). Real off the shelf optics are used for this design.

The objective is a 1.5" diameter 75 mm focal length N-BK7 plano-convex lens from Thorlabs (part # LA1386). The lens would need to be cut to a 1" square by a process such as water-jetting and glued to other objective lenses to form a monolithic fly's eye array. The ball lens is made from N-BK7 and is 5 mm in diameter, readily available from Edmund Optics (part #43-712). 5 mm ball lenses are also available in large quantities from other online sources, though the quality of these lenses would need to be verified before use.

This design was optimized for the same fields of view and wavelengths as the ideal design in section 2.4. An extra dielectric loss was allowed, which improved pupil imaging by using the full power of the ball lens (see Figure 2.8). A CPV cell that is AR coated for air exhibits a slightly smaller conversion efficiency, but for the purposes of a prototype a 1-2% loss in efficiency is not too detrimental. If an optically contacted CPV cell is preferred then a SYLGARD-184 layer can be used, but it would need to be 1.4 mm thick, and the ball lens would need to be reduced to 4 mm in diameter. While this would save a couple percent in optical efficiency, the optical performance is degraded for off-axis imaging, which is why the extra dielectric loss is preferred. For the ball lens in air design, the chromatic pupil blurring is about +/- 2% in diameter on-axis but degrades significantly off-axis.

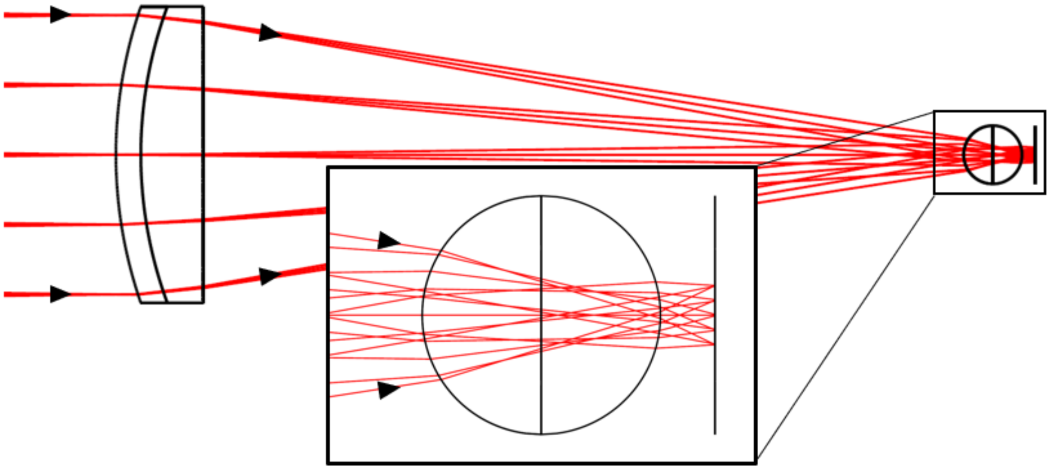

*Figure 2.8: Optical layout for an off the shelf 300X concentration design. The ideal cell size is 1.5 mm square, but a commercially available 3.3 mm CPV cell would be used for a prototype, making the global geometric concentration 60X. Angles depicted are on-axis and +/- 0.75°.*

The overall performance of this design is comparable to the design shown in Figure 2.5 except for loss of uniformity between different areas of the spectrum as the solar disk goes further off-axis (i.e. Chromatic change in magnification of the pupil image). Nevertheless, the performance is very good. The acceptance angle is boosted compared to the previous design. A 20% degradation in relative total illumination is not reached until the solar disk is centered at 1.49°, nearly double that of the optimized angles (see Figure 2.9)! A quick look at the transmittance of this array of lenses shows that 13.7% of the light entering the array does not make it due to TIR. This is for angles ranging from 1.5 to 89.5 degrees weighted by their cosine factors. This shows a worse performance for this design than for the design in section 2.4, but the majority of the diffuse light is still incident upon the silicon.

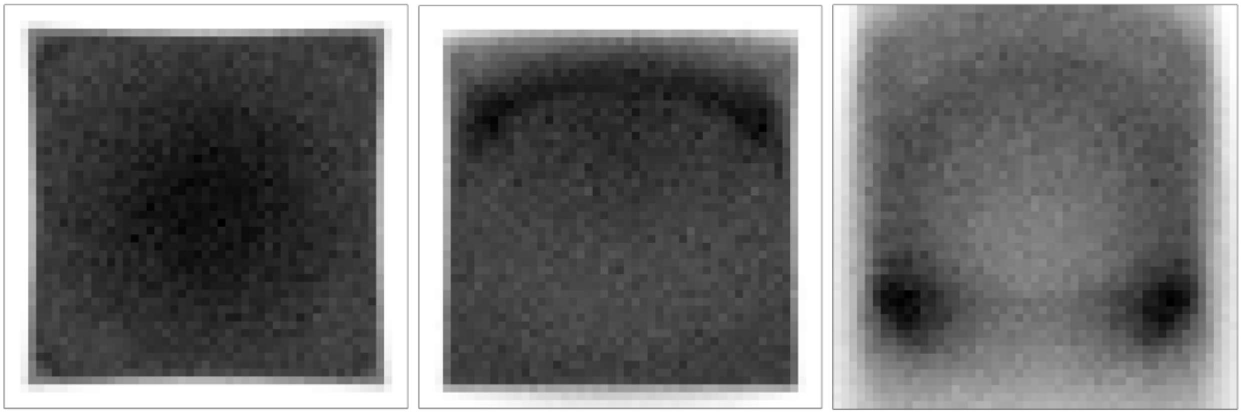

On-Axis Sun 100% | 0.75° Off-Axis Sun 100% | 1.49° Off-Axis Sun 79.7%

*Figure 2.9: Pupil images formed on a 1.5 mm square CPV cell beginning with on-axis sun (i.e. +/- 0.25° solar disk object) on the left and further off-axis positions towards the right. Total relative illumination is provided showing that performance of the optical system does not deteriorate to below 80% until the solar disk is located 1.49° off-axis. Chromatic aberration causes a noticeable loss of uniformity. The size of the actual CPV cell would be 3.3 mm, as this is commercially available.*

The design shown here has the advantage of using commercially available components. These optical components could be purchased today, and a prototype could soon be built. Additionally, this design exhibits a larger acceptance angle, allowing less money to be spent on a dual-axis tracking unit. Despite these advantages, this may not be the ideal long-term system. Having grooves exposed to the elements could lead to significant dust and grime build-up, reducing overall performance. Additionally, two extra dielectric losses reduce the optical efficiency of the system (the glass-air reflection from the back surface of the ball lens and the air-dielectric reflection from the CPV cell). Also, the TIR loss for diffuse light is worse, leading to an overall reduced energy production over the lifetime of use.

In contrast, the ideal design shows an overall better performance. In a commercial setting, large quantities of aspheric dome-lenses could be manufactured at a comparable cost to materials, and large quilted fly's eye arrays could be manufactured right off a float glass production line. The ideal design has fewer dielectric losses and better TIR performance for diffuse light. Additionally, the chromatic loss of uniformity is much less at large off-axis angles, and soiling of the exposed surface cannot accumulate in grooves. The acceptance angle for the ideal design is not as large, thus a slightly more expensive dual-axis tracker could be required. Additionally, the manufacture of large cost-effective aspheric fly's eye arrays would involve significant research and development.

Considering these arguments, the prototype approach may be best. Both the ideal and prototype designs have varying pros and cons. Perhaps a different design could split the difference between the two. It would take advantage of modern manufacturing techniques while still exhibiting similar pros to the ideal design. A balanced approach designing a hybrid concentrator would use elements that may not be off the shelf available. Rather, it would use optical elements that could be made within the next year or so for a reasonable price. A look at commercially available architectural glass introduces this alternative design.

## 2.6 Reed Glass Hybrid Design

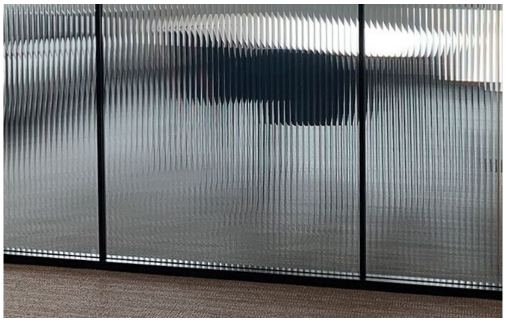

*Figure 2.10: Reed glass used in an office setting. Sold by companies such as Decorative Film, from which this photo was obtained.*

Reed glass is produced by manufacturers for architectural applications. The glass can be frosted or transparent depending on the desired look. This patterned glass consists of a repeating pattern of curved partial cylinders that can reach sizes over 2 $m^2$ (see Figure 2.10). Sunlight incident upon such a piece of glass would create a series of line foci. The cost of reed glass ~4 mm thick is sold at the consumer level for about \$70/$m^2$. This cost could reasonably be expected to be reduced by a factor of 2-3 for mass production, and the cost would be even less if low-iron soda-lime float glass was used.

The issue with using this glass is that focusing occurs in only one dimension. However, if a second sheet of glass were placed behind and rotated 90 degrees, then focusing occurs in both dimensions. An experiment was performed showing that this works. Two reed glass sheets were optically contacted with both flat faces in contact with each other. The patterns were set in orthogonal directions. The measured shape of the repeating cylinder, using a coordinate measuring machine (CMM), was 28.5 mm radius of curvature and -54.1 for the conic constant. According to Eq. 1-10 the ideal conic constants for the front and back surfaces are -0.44 and -2.25, respectively (for glass with an index of refraction of 1.5). Therefore, a conic constant of -54.1 causes a large amount of spherical aberration. In Figure 2.11 the observed effect of this incorrect surface shape is a grid pattern of square spots instead of circular spots.

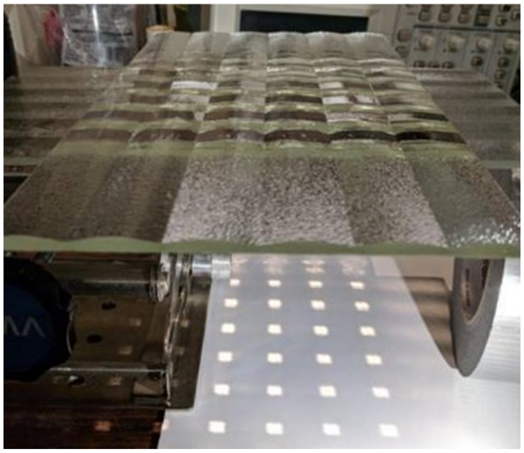

*Figure 2.11: Experiment using two sheets of reed glass with flat surfaces optically contacted and patterns set orthogonal to one another. Focus is accomplished in both directions, though the spot formed is square in shape due to an incorrect shape in the reed glass sheets.*

The thickness of the glass shown above is 4 mm for each sheet (8 mm total thickness). To keep the cost down, the total thickness of glass needs to be near 4 mm for the optimal design. This means that instead of optically contacting two pieces of off the shelf sheets of glass, as in Figure 2.11, a sheet of glass should be imprinted with orthogonal cylindrical patterns on the front and back with the appropriate conic constants. Using the pupil imaging merit function, a design was created with two orthogonal cylindrical patterns on the front and back, respectively. The cylindrical shape of the front and back were both allowed to be aspheric. A ball lens was used once again to reduce cost. The optical prescription is provided in Table 2-2. Note, the conic constant of the front surface is -0.41 and the back surface conic constant is -1.96, both very near to the predicted -0.44 and -2.25. Together the cross-cylindrical aspheric biconvex objective and a simple ball lens obtain 287X geometric concentration (see Figure 2.12). The advantage of cleaning a flat surface is still obtained by orienting the outward facing face of the array with the grooves vertical. Accumulation of dust and grime is then minimized.

*Table 2-2: Optical prescription for 300X concentration CPV design using aspheric cylindrical lenses on the front and back surfaces of the objective element with radii of curvature in orthogonal directions.*

| Y Radius | Y Conic | X Radius | X Conic | Thickness | Material | Semi-Diameter |
|---|---|---|---|---|---|---|
| 36.509 | -0.412 | Infinity | 0.000 | 6.500 | N-BK7 | 17.961 |
| Infinity | 0.000 | -35.204 | -1.958 | 62.717 | | 17.961 |
| 2.359 | 0.000 | 2.359 | 0.000 | 4.717 | N-BK7 | 2.359 |
| -2.359 | 0.000 | -2.359 | 0.000 | 1.066 | | 2.359 |
| Infinity | 0.000 | Infinity | 0.000 | 0.000 | | 2.121 |

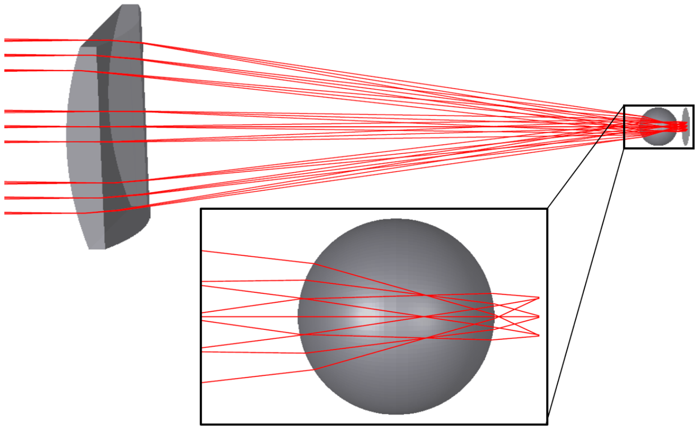

*Figure 2.13: 3D layout of 287X concentration CPV design using elements that could be readily obtained by working with patterned glass manufacturers.*

The objective element could be made by creating two cross-patterned rollers to press-mold glass on a patterned glass manufacturing line (see Figure 2.12). These rollers would need to be precision machined, which would have a large upfront cost. Metrology of the generated patterned sheets would require a combination of CMM measurements, interferometry with computer generated holograms (CGH), and/or potentially deflectometry. If multiple hybrid systems were made, it would likely be too costly to perform this measurement for every glass array, so the arrays would be randomly sampled and measured to ensure the rollers were not deformed over time (similar to what cell-phone manufactureres do for gull-wing lenses).

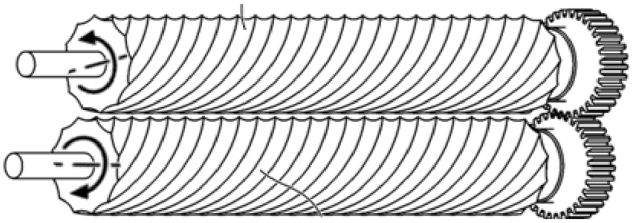

*Figure 2.12: Orthogonally oriented rollers for press-molding glass sheets according to the desired optical prescription.*

The solar pupil images obtained for this design are shown in Figure 2.14. The solar disk acceptance angle is a smaller +/- 1.38° before power collection drops below 80%, but the uniformity of this design is better than that for the off the shelf ball lens design. The time for production is longer than the off the shelf design, but less than the ideal design. However, for an alternative prototype, suitable architectural glass could be “sandwiched” together so long as the

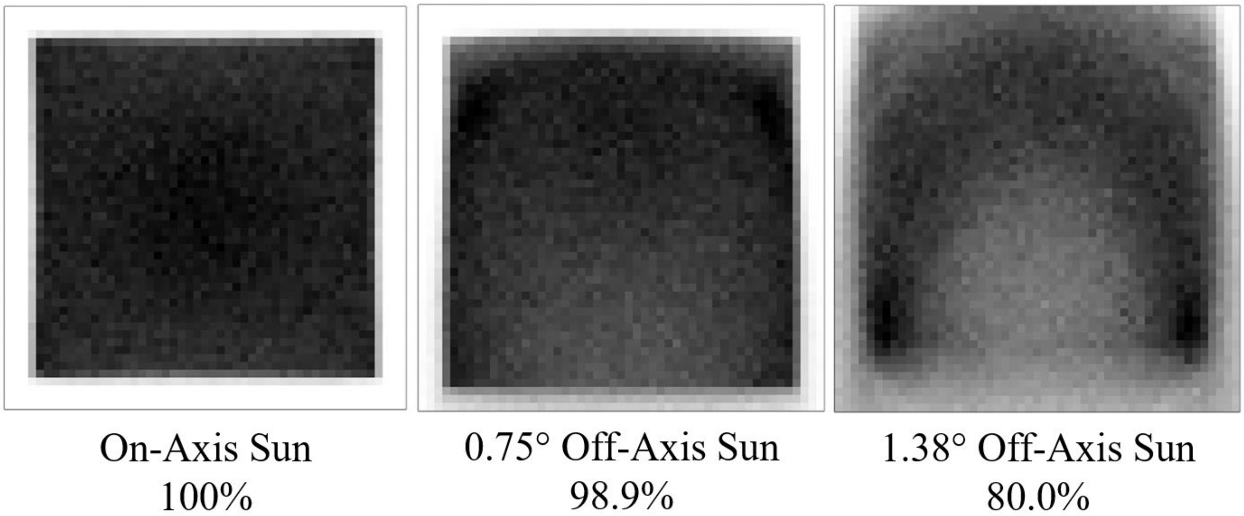

*Figure 2.14: Pupil images formed on a 1.5 mm square CPV cell beginning with on-axis sun (i.e. +/- 0.25° solar disk object) on the left and further off-axis positions towards the right. Total relative illumination is provided showing that performance of the optical system does not deteriorate to below 80% until the solar disk is located 1.38° off-axis. Chromatic aberration causes a slight loss of uniformity.*

cylindrical shapes were close to what is desired. The transmittance of this array of cylindrical lenses showed that 13.2% of the diffuse light entering the array does not make through due to TIR, which is slightly better than the off the shelf design.

Overall, a reed glass hybrid design appears to be the middle ground between a lower performance off-the-shelf

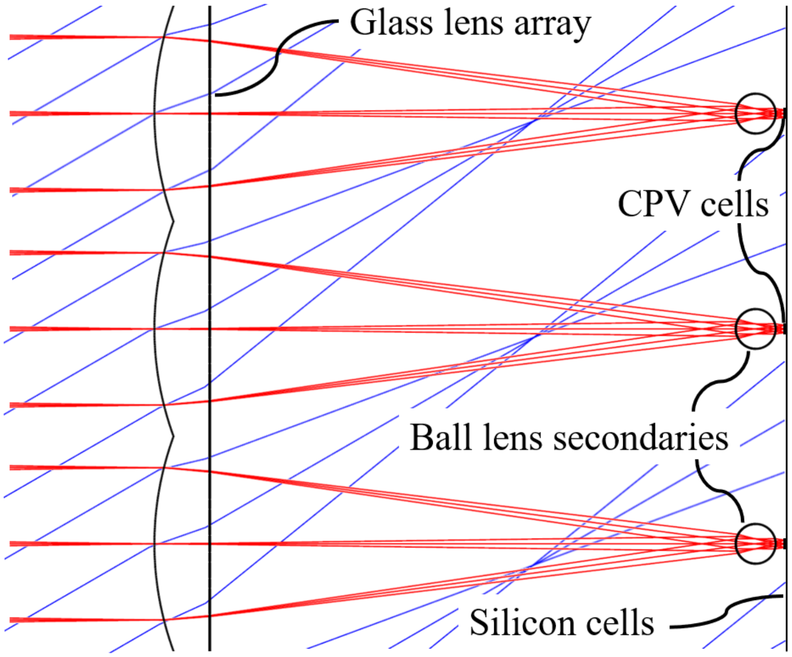

*Figure 2.15: A hybrid PV system consisting of a glass array where the front surface is composed of a series of long cylindrical lenses of elliptical shape and the back surface is composed of a series of long cylindrical lenses of hyperbolic shape. Thus, an array of lenses is formed, which each focus light onto a secondary ball lens. The ball lens forms a pupil image onto a high-efficiency CPV cell for direct sunlight (red). Diffuse light passes through the lenslet array (with a 13.2% TIR loss) and is converted by the silicon cells located on the back surface of the system.*

system and a costly ideal system. For a reed glass hybrid design the overall system would consist of a large monolithic array where the front surface consists of a series of long cylindrical lenses with an elliptical shape and a back surface consisting of an orthogonally oriented series of long cylindrical lenses with a hyperbolic shape. Incident direct sunlight would be focused and captured by an array of secondary ball lenses, which create an array of pupil images, each on a high-efficiency CPV cell (see Figure 2.15). The CPV cells would be mounted onto a surface consisting of silicon PV cells, which would convert off-axis diffuse light to electricity with roughly half the efficiency of the CPV cells. Together, the CPV cells and silicon PV cells would maximize the total energy conversion with the only significant added cost being a low-precision dual-axis tracking unit. Approximately the same amount of materials would be required for this system as for a silicon PV solar panel, which in high volume places the cost of this panel similar to a standard solar panel, but with up to twice the energy conversion.

## 2.7 Conclusion

The optical design for concentrated photovoltaics is driven by a need to obtain high concentrations of sunlight where the efficiency of CPV cells peak and the cost of the cells drops as the required area of cells is reduced. At approximately 300X concentration, the cost per watt of CPV cells is well matched to silicon cells. Reaching concentrations much greater than this (~1000X) leads to a lower cost for CPV cells, but this cost savings is offset by a need for more complicated optical layouts where multiple stages of concentration may be required.

At 300X concentration much simpler optics can be used. A general approach is to use a fly’s eye array with each lenslet followed by a secondary ball or dome lens, which images the fly’s eye array onto an array of CPV cells for high-efficiency conversion of sunlight. The weight of the glass needed in the optical components becomes similar to the weight of glass already used as a protective covering in solar panels. Thus, in high volume, the cost of a CPV panel as described is similar to the cost of a solar panel, with solely the added need for dual-axis tracking.

A significant benefit is obtained when the array of CPV cells is mounted onto a large region of silicon solar cells (see Figure 2.15). Then compared to single-axis tracking silicon solar panels, twice the amount of energy can be generated in regions like Tucson, Arizona, and 75% more energy can be generated in regions like Seattle, Washington (not considering optical losses). The benefits of a hybrid system could potentially outweigh the added cost of dual-axis tracking, especially with a large acceptance angle that reduces the required precision for dual-axis tracking.

A series of options are available to create such a hybrid system, the most promising of which involves a lenslet array where the front and back surfaces are composed of a series of long cylindrical surfaces (reed glass) that are orthogonally oriented so that focusing occurs in both the tangential and sagittal planes. An inexpensive ball lens serves as the secondary optic, which allows for high mispointing of +/- 1.39° of the solar disk before energy production drops below 80%. A system of this nature may be what is required to drop the cost of solar energy below current costs of electricity generated by fossil fuels.

In the next chapter, an alternative, yet complementary approach to photovoltaic solar energy is discussed: concentrated solar power. Instead of focusing sunlight onto photovolatic cells, mirrors are used to focus sunlight on a central receiver where the heat can be used to create steam or potentially provide heat for industrial processes. Companies, such as Heliogen, hope to obtain very high concentrations and reach temperatures greater than 1500 °C at which point hydrogen fuel can be generated [31].

# CHAPTER 3 : CONCENTRATED SOLAR POWER (CSP)

## 3.1 Introduction

Heliostats are used to concentrate sunlight onto a central power tower where the heat is often converted into electricity by a generator. This Concentrated Solar Power (CSP) approach to generating electricity is complementary to photovoltaics. Solar panels can generate electricity throughout the day. At the same time CSP can be used to collect heat throughout the day, which is stored and then used to generate electricity at night when solar panels are no longer useful, which is not a new concept [32].

Recent innovation in the CSP world has led to an interesting application of heliostats; the realistic possibility of creating hydrogen fuel [31]. Solar concentrations of 1,200X are required to achieve temperatures around 1,500 °C. At this temperature it becomes possible to create hydrogen fuel. The energy content of hydrogen is about 3 times as much as gasoline making it an ideal substitute for automotive vehicles [33]. Especially because using hydrogen does not involve the emission of $CO_2$. Clearly, it is very desirable to be able to create a high-density green fuel that can replace gasoline. A potential solution is a very high concentration of sunlight, and a lot of it.

In addition to hydrogen fuel, the temperatures made possible by high concentration heliostat fields could allow for industrial heating processes to use heliostats instead of fossil fuels to create heat. Industrial heating produces about 10% of the world's $CO_2$ emissions, and it is perhaps the most challenging area to replace fossil fuels with green fuels [34].

One great challenge for applying heliostat technology to industrial heating, such as a blast furnace, is the need for a continuous steady heat source. Variation of weather throughout the day may cause significant variation in the heat production of a field of heliostats. Thus, heliostats may not be directly useful in this sector. However, hydrogen fuel created by heliostats could prove to be a suitable substitute for fossil fuels.

## 3.2 A Conventional Power Tower

For a conventional power tower, typically, thousands of flat-mirror heliostats are used in concert all reflecting sunlight towards the same receiver. A heliostat consists of a supporting structure upon which a mirror is mounted. This structure can rotate in two different axes such that the mirror can be positioned to reflect incident sunlight towards a receiving tower. The geometry of a heliostat field is such that the light at the central receiver is spread out over a size not much larger than the image that would be formed by a pinhole camera. The heliostat itself often ranges in size from half the size of the pinhole camera solar disk image to about the same size. In the case of half the size of the pinhole camera solar disk, the diameter of the heliostat would be,

$$D = F\theta_{Sun}/2 \approx F/230, \qquad \textit{Eq. 3-1}$$

where $F$ is the focal distance to the central receiver and $\theta_{Sun}$ is the angular subtense of the Sun, which is approximately 1/115 radians. In the case of the Ashalim Power Station the furthest heliostat is 1.0 km from the central receiver and each heliostat is about 4.3 m in diameter, which is half the pinhole solar disk diameter. [35].

The solar images from heliostats at the edge of the field have an RMS diameter of about 7.0 m in diameter for heliostats at the edge of the field. This equates to about 70% of the reflected energy. To capture the geometric spot size (100% of reflected energy) the receiver would need to be about 12 m wide (see Figure 3.1). To account for surface errors and mispointing, the actual receiver for the Ashalim Power Tower is about 22 m wide. Perhaps a power tower manufacturer would want the heliostats to each act more like pinhole cameras. This would require a significant reduction in the size of the heliostats, and thus a significant increase in the required number of heliostats.

The number of heliostats required for the Ashalim Power Tower (50,000) was dictated by the goal of a large power capacity (121 MW), the use of flat heliostats, and the goal of getting the geometric concentration ratio to ~650X. The large number of heliostats is necessary because of the small concentration provided by each heliostat of ~1/25X. At this concentration ratio electricity can be generated with a steam boiler.

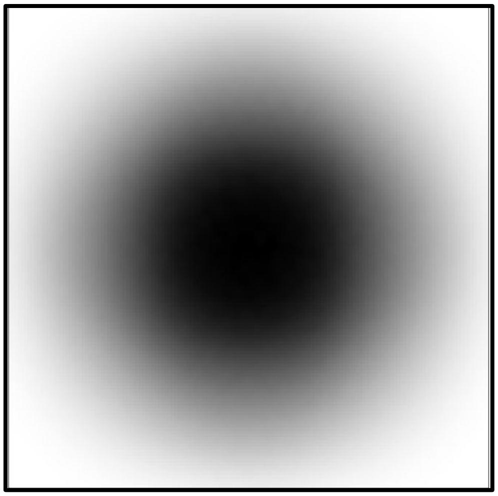

*Figure 3.1: Ray traced solar image formed by an Ashalim Power Tower heliostat located 1 km from the receiver. The size of the box shown is 12 m square.*

## 3.3 The Need and Potential for Higher Concentration

The ability to create Hydrogen fuel is well out of reach of the Ashalim Power Tower because 1,500 °C is necessary. To obtain 1,500 °C, 1,200X solar concentration needs to be fed into the power tower receiver [31]. At 1,200X solar concentration there is an acceptable loss of radiation. Relevant to this discussion is whether it is even possible to achieve 1,200X concentration? What is the maximum possible concentration?

Assuming the area of heliostats is about 1/3 of the land area (as is the case for the Ashalim Power Tower and other power towers to avoid shadowing and blocking), the total area of heliostats is given by

$$A_{Helio} = \pi R^2/3, \quad \text{Eq. 3-2}$$

where $R$ is the radial distance to the furthest heliostat (assuming a field of heliostats in a circular pattern centered on the receiver tower). The size of the receiver is a cylinder with a diameter and height matching the size of the solar disk image for the furthest heliostat. Thus, the area of the cylinder is given by

$$A_{Cyl} = \pi D_{sun}^2 = \pi R^2/115^2, \qquad \textit{Eq. 3-3}$$

where $D_{sun}$ is the diameter of the solar disk image, which is $R/115$. If each heliostat could form an ideal solar disk image on the tower receiver, then the maximum possible concentration is

$$C = \frac{A_{Helio}}{A_{Cyl}} = 4{,}400. \qquad \textit{Eq. 3-4}$$

This level of concentration is not reasonable though because the size of the receiver cannot be the exact same size as the solar disk image (due to mispointing). A good rule of thumb is to increase the diameter of the receiver by a factor of $\sqrt{2}$ compared to the size of the largest solar disk. *Thus, the maximum concentration possible is 2,200X.* It is the same maximum concentration whether a circular receiver is used, or a cylindrical receiver is used, though in the case of a circular receiver the solar angles of incidence tend to be more favorable. However, cylindrical receivers provide more energy production for a fixed size of receiver. Considering an average 10% loss in reflection, mispointing errors and an average cosine factor of perhaps 0.7, a geometric concentration of 2,200X quickly reduces to 1,200X solar concentration.

Thus, it is possible to obtain the concentration necessary to reach 1,500 °C, though this is near the limit of what is possible. This is most readily accomplished if the heliostats being used are similar in performance to a pinhole camera or if the heliostats have the appropriate curvature to focus sunlight. In the standard approach the number of heliostats required for a conventional powerplant goes into the tens of thousands and the cost grows excessively. Additionally, a high solar concentration of 1,200X is not possible. If instead of using flat mirrors, curved mirrors were used, then high concentrations would be possible with a smaller number of larger heliostats. However, the shape of the ideal heliostat is not static for focusing light throughout the day. For a fixed shape heliostat, high concentrations are possible for certain solar positions, but in the morning and evening astigmatism significantly reduces solar concentration. In this next section the effects of astigmatism are characterized.

## 3.4 Fixed Shape Heliostat vs Actively Focused Heliostat

Successful efforts have been made in the past to characterize spot size due to astigmatism [36]. The Coddington equations show that the effective radii of curvature of a spherically shaped mirror are changed at off-axis angles of incidence. Eq A-20 and Eq A-21 from Appendix A show that the tangential radius of curvature is effectively the physical radius of curvature times the cosine of the angle of incidence. Similarly, the sagittal radius of curvature is effectively the physical radius of curvature divided by the cosine of the angle of incidence.

Therefore, for a given angle of incidence on a spherical mirror, the optical power in the tangential direction is

$$\phi_T = \frac{2}{R\cos(I)}, \qquad \textit{Eq. 3-5}$$

and the optical power in the sagittal direction is

$$\phi_S = \frac{2\cos(I)}{R}, \qquad \textit{Eq. 3-6}$$

where $I$ is the angle of incidence and $R$ is the physical radius of curvature of the mirror. In this treatment, the solar disk is placed on-axis and the optical power of the mirror is given by Eq. 3-7 and Eq. 3-8. Using the first order equations for ray tracing (Eq. 1-1 and Eq. 1-2), the marginal ray heights in the tangential and sagittal planes are

$$y_T' = y_T(\cos(I) - 1) \text{ and} \qquad \textit{Eq. 3-7}$$

$$y_S' = y_S(1 - \cos(I)), \qquad \textit{Eq. 3-8}$$

where $y_T$ and $y_S$ are the marginal ray heights (aperture radii) of the heliostat, and $y_T'$ and $y_S'$ are the marginal ray heights at a focal distance of $R/2$ (i.e. the on-axis focal distance for the spherically shaped mirror). Some explanation is necessary for Eq. 3-9. $y_T$ is the physical aperture radius of the mirror, but the effective aperture radius is the physical aperture radius foreshortened by a cosine factor. In other words, the tangential marginal ray height must be multiplied by the cosine of the angle of incidence in order to take into consideration the shortened appearance of the mirror at off-axis angles. This treatment is ignoring any cosine factor that would occur by the sunlight being incident upon the tower at an oblique angle, as is the case when the cylindrical receiver is high in the air and vertical.

The chief ray heights are the same for both the tangential and sagittal planes, given by

$$\bar{y}' = \frac{\bar{u}_{sun}R}{2} \cong \frac{R}{458}, \qquad \textit{Eq. 3-9}$$

where $\bar{u}_{sun}$ is the chief ray angle made by an on-axis sun, which is about 1/229 radians. The maximum dimensions of the spot are then given by adding the absolute value of the marginal ray(s) to the chief ray and doubling that value, which gives

$$D_T = 2|y_T'| + 2|\bar{y}'| = 2|y_T|(1 - \cos(I) + |R|/229 \text{ and} \qquad \textit{Eq. 3-10}$$

$$D_S = 2|y_S'| + 2|\bar{y}'| = 2|y_S|(1 - \cos(I)) + |R|/229. \qquad \textit{Eq. 3-11}$$

Performing a ray trace in Zemax OpticStudio confirms the validity of these equations. For a 1.5 m diameter heliostat focusing at 40 m with sunlight at 45° angle of incidence the size of the spot in the tangential direction is 788.5 mm and the size of the spot in the sagittal direction is 788.4 mm. According to Eq. 3-12 and Eq. 3-13, the size of the spot in both directions is 788.7 mm, a 0.04% error compared to the sagittal spot size.

Note, a 45° angle of incidence happens for a northern heliostat about 10% of the time of the Sun being up (over a year in Tucson, Arizona with the tower height half the distance of the heliostat from the tower). For an eastern and western heliostat, it happens about 1/3 of the time. For a southern heliostat it happens close to half of the time.

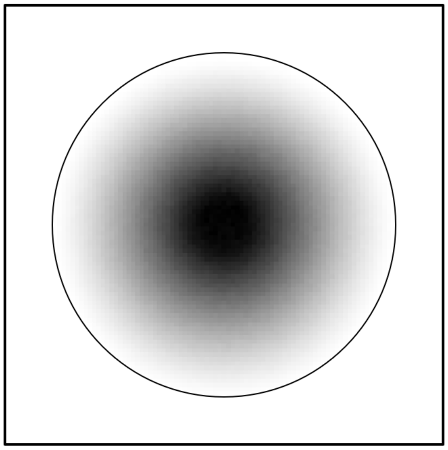

*Figure 3.2: Solar image formed by 1.5 m aperture mirror with 80 m radius of curvature at 45° angle of incidence, 40 m from the vertex of the mirror. The outer box is 1 m square. The irradiance follows a cone distribution with maximum irradiance at the center and zero irradiance at the maximum spot size (i.e. the black circle).*

While this method does predict the maximum dimension of the spot formed, it does not predict the variation in uniformity across the blurred solar image, which can be significant. A convolution of images formed by each point in the pupil is required to get this information. The result is simply a cone function with the peak at the center sloping down to zero irradiance at the maximum spot dimension (assuming a perfectly uniform Sun). This can simply be obtained by ray tracing (see Figure 3.6).

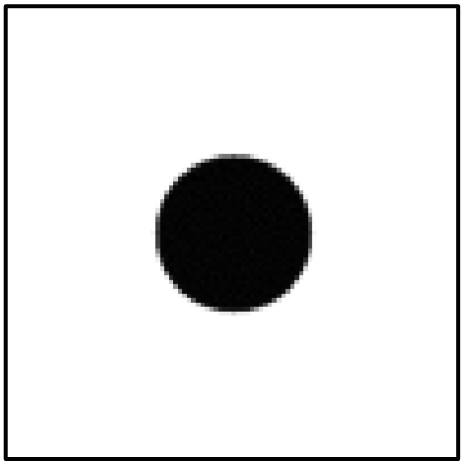

*Figure 3.3: Solar image formed by 1.5 m aperture mirror with different tangential and sagittal radii of curvature at 45° angle of incidence, 40 m from the vertex of the mirror. The outer box is 1 m square.*

In contrast, making the heliostat mirror surface biconic with the appropriate radii of curvature in the tangential and sagittal planes, a well-corrected solar image can be formed. The appropriate radii of curvature are

$$R_t = \frac{2F}{\cos(I)}, \text{ and} \qquad \textit{Eq. 3-12}$$

$$R_s = 2F\cos(I), \qquad \textit{Eq. 3-13}$$

with $F$ as the focal distance from the heliostat to the tower receiver, and $I$ as the angle of incidence.

The resulting ray trace from such a toroidal surface is provided in Figure 3.7. The solar disk image formed is 350 mm in diameter. Thus, a geometric concentration from a 1.5 m heliostat to a 0.35 m spot is about 18X. Comparing this to the solar image shown in Figure 3.6 reveals the benefits of correcting astigmatism.

The amount of energy inside a chosen radius for a cone shape irradiance distribution is approximately given by

$$P = \frac{3r^2}{R_s^2}\left(1 - \frac{2r}{3R_s}\right) \times 100\%, \qquad \textit{Eq. 3-14}$$

where $r$ is the chosen radius (the ideal solar disk radius) and $R_s$ is the maximum radius of the aberrated spot. Using Eq. 3-14 the amount of energy contained within 0.35 m is 41.7% of the total when a spherical surface is used. If the target receiver were a circular disk 1.5 times the size of the best solar disk image, 74% of the total reflected flux is the most that will make it onto the target receiver. Clearly there are some significant gains in correcting astigmatic aberrations.

If the goal is to maximize the amount of light reflected onto a target receiver while maximizing concentration, as is needed for high efficiency thermodynamic conversion, then one of two things needs to happen: a large number of pinhole camera heliostats need to be used (possibly in the millions), or focusing heliostats need to be used with the ability to correct astigmatism. Hundreds of actively focused heliostats seem far more reasonable than millions of pinhole heliostats. Therefore, actively focused heliostats are of high interest.

The most common mounting scheme for a heliostat is the altazimuth mount. Solving this problem using an altazimuth mounting scheme is a promising approach to creating a shift of mindset in the heliostat community concerning what is needed to meet the demanding energy goals of today. The first step towards being able to correct for astigmatism is then to see what shape the mirror surface needs to be based on the positions of the heliostat and Sun.

## 3.5 The Ideal Shape of an Altazimuth Mounted Heliostat

The ideal shape of a focusing heliostat varies throughout each day depending on the location of the heliostat relative to the receiver and the location of the Sun. The greater the angle of incidence of sunlight the less spherical the mirror should be. There are three variables in this situation that need to be solved for to obtain the three bending modes of the heliostat: the radius of curvature in the tangential plane, the radius of curvature in the sagittal plane, and the angle of astigmatism. In Appendix A: Derivation of the Ideal Heliostat Shape, a full mathematical treatment of the ideal heliostat shape is provided in the coordinate system of the heliostat mirror. Here only the results are stated.

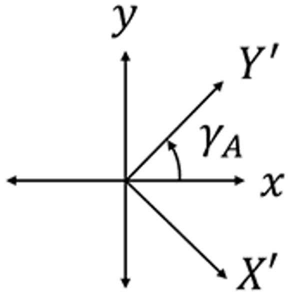

*Figure 3.4. Angle of astigmatism, $\gamma_A$, relative to the local x and y axes of the heliostat mirror.*

The three variables, the sagittal and tangential radii of curvature (Eq. 3-12 and Eq. 3-13) and angle of astigmatism (see Figure 3.4), involve a view of a toroidal surface that can physically be rotated about its optical axis. In an altazimuth mounting scheme this is not the case. Therefore, a different way of viewing the surface is more useful. The surface shape can be decomposed into three different modes: power, oblique astigmatism, and vertical astigmatism. These three modes are of the form

$$Z = a_1(X^2 + Y^2) + a_2 2XY + a_3(X^2 - Y^2), \tag{Eq. 3-15}$$

where $a_1$, $a_2$, and $a_3$ are the coefficients for power, oblique astigmatism, and vertical astigmatism, respectively. If the angle of astigmatism is zero, as is the case for a target aligned heliostat, then there is no oblique astigmatism and the surface can be expressed in terms of a biconic surface with

$$Z = (a_1 + a_3)X^2 + (a_1 - a_3)Y^2 = \frac{X^2}{2R_S} + \frac{Y^2}{2R_T}, \tag{Eq. 3-16}$$

where $R_S$ and $R_T$ are relative to the tangential and sagittal curvatures by

$$C_t = \frac{1}{R_T} = \frac{\cos(I)}{2F}, \text{ and} \tag{Eq. 3-17}$$

$$C_s = \frac{1}{R_S} = \frac{1}{2F\cos(I)}, \tag{Eq. 3-18}$$

with $F$ as the focal distance from the heliostat to the tower receiver, and $I$ as the angle of incidence.

Therefore, the biconic surface is a special case for an altazimuth mounted heliostat. Instead of viewing the mirror as something that can be physically rotated, the mirror can be considered fixed and the shape of the mirror can be rotated. Eq. 3-16 is the equation for the surface, but it is in a rotated coordinate frame relative to the coordinate frame of the mirror. This rotation angle is the angle of astigmatism.

Rotating the biconic surface into the coordinate frame of the mirror leads to the coefficients for power, oblique astigmatism, and vertical astigmatism with

$$a_1 = \frac{1}{4}(C_t + C_s), \tag{Eq. 3-19}$$

$$a_2 = \frac{1}{4}(C_t - C_s)\ \sin(2\gamma_A), \tag{Eq. 3-20}$$

$$a_3 = \frac{1}{4}(C_t - C_s)\ \cos(2\gamma_A), \tag{Eq. 3-21}$$

where $C_t$ is the tangential curvature (the reciprocal of the tangential radius of curvature), $C_s$ is the sagittal curvature, and $\gamma_A$ is the angle of astigmatism relative to the local x-axis of the mirror.

These three simple coefficients completely describe the surface required to correct for astigmatism on an altazimuth mounted mirror. Note, coma is still present in the solar image, but this is small compared to the solar disk size (see section A.1)

The real challenge in this derivation of ideal shape is calculating the angle of astigmatism. This involves taking a vector that describes the position of the Sun in global coordinates and projecting it onto the surface of the heliostat. The surface of the heliostat is rotated in the global frame, which makes this projection a multi-step process (see Eq A-28 through Eq A-38). Once the solar vector is projected onto the surface of the heliostat and defined in the local coordinate frame it is a simple matter to calculate the angle of astigmatism. Appendix B and Appendix C together contain MATLAB® codes that can calculate the surface shape coefficients for a heliostat. This requires a specific geographic location relative to a target receiver on a desired day of the year at the specified time. Just the code from Appendix C is required if the solar azimuth and elevation angles are known along with the position of the heliostat relative to the target receiver.

## 3.6 Heliostat Mounting Schemes

As previously stated, a fixed shape focusing heliostat exhibits large amounts of astigmatic aberration at off-axis angles of incidence. This causes a large amount of spillage in the early morning and late afternoon, unless the manufacturer settles for a lower geometric concentration so that more of this light is captured (i.e. increase the receiver size). At ideal times of day (+/- a few hours around solar noon) the astigmatic aberration of each heliostat in a power tower field is relatively small for spherically shaped heliostats. A high solar concentration is possible during these times. But for the other 6-8 hours of a 12-hour day it is more challenging to obtain the high solar concentrations required to generate hydrogen fuel. A solution to the ideal shape of a heliostat has been provided for an alt-azimuth mounted heliostat. An exploration of this mounting scheme and other mounting schemes provides the groundwork for understanding how an actively shaped heliostat could be created.

There are a variety of ways that a heliostat mirror can be mounted with two orthogonal rotation axes that allow the mirror to be oriented such that sunlight is reflected towards a central tower receiver. Most heliostats are on an altazimuth mount where the elevation axis is always parallel to the ground and the azimuth axis points straight up (see Figure 3.5). The advantage of this mounting scheme is the mechanical simplicity and the range of motion. The mirror can be oriented in any desirable direction including a horizontal stow position for high winds. The mirror is tucked in close to the mounting pole so that there is a reasonably small moment exerted on the pole. The disadvantage to this mounting scheme is the challenge of compensating astigmatic aberration. This challenge will be discussed in more detail later.

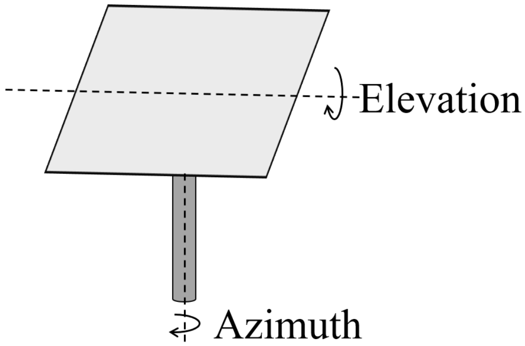

*Figure 3.5: Schematic of altazimuth mounted heliostat. Elevation (altitude) and azimuth axes are always orthogonal allowing for the mirror to be oriented in any desired direction.*

Another mounting scheme is found in the target-aligned heliostat. In the target-aligned mounting scheme one axis of rotation is pointed at the target receiver, the target axis, and the other points orthogonal to the target receiver, the “elevation” axis. Just like the altazimuth mounting scheme where the pointing of the elevation axis depends on the rotation angle of the azimuth axis, the pointing of the elevation axis of the target-aligned mount depends on the rotation angle of the targeted axis (see Figure 3.6). Elevation axis may be a misnomer because while at times this axis will tilt the mirror up and down, if the target axis is rotated by 90 degrees then this axis tilts the mirror left and right.

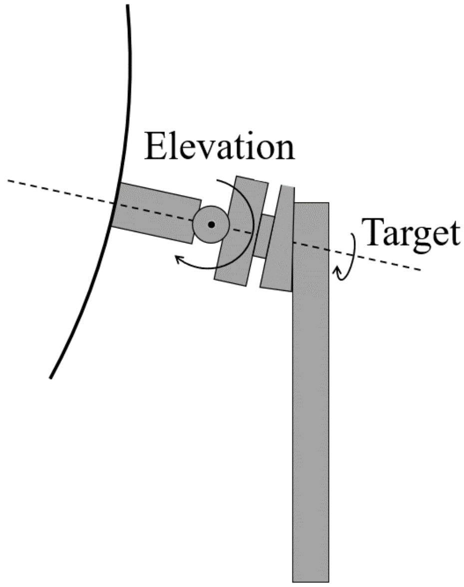

*Figure 3.6: Target-aligned mounted heliostat. The target axis of rotation is pointed at the target receiver and the elevation axis points in and out of the page. The black curved segment is the mirror.*

This type of mounting scheme has been suggested to compensate for astigmatic aberration because the tangential axis of the mirror is always in the tangential plane of reflection [37,38]. Meaning, the plane that contains the vertex of the mirror, the Sun, and the receiver will always bisect the mirror at the same position. If the radii of curvature in the tangential and sagittal planes of the heliostat are set appropriately, then astigmatic aberration can be well corrected for larger angles of incidence at the cost of blurring at small angles of incidence.

This mounting scheme adds some mechanical complications. There is a greater moment on the mounting pole due to the mirror being further away. This can be reduced if the mirror is tucked in closer at the cost of a reduced range of motion. This reduced range of motion may prevent the mirror from being able to go into a horizontal stow position during high winds. A clever mechanical engineer could work around this. However, there are other challenges with this mounting scheme. Another complexity for the target-oriented mounting scheme is that each heliostat in the field has a uniquely oriented target axis. Therefore, each heliostat needs to be made such that the orientation of the target axis can be varied (so that it always points at the receiver), or the mounts need to be divided into groups of heliostats with the same radial distance from the tower (and elevation). The target-aligned mounting scheme has not been widely implemented in the industry. Likely, this is due to the reasons discussed above.

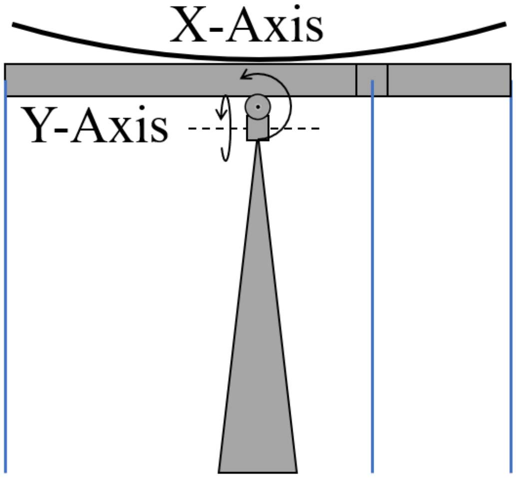

*Figure 3.7: Cable drive mounted heliostat. The y axis is always parallel to the ground and the x-axis changes its pointing depending on the rotation of the y-axis. The two axes always remain orthogonal. The cables are in blue, with the center blue line being two separate cables.*

A final mounting scheme to consider is a cable-drive mount, currently being researched by Heliogen [39]. In this layout a minimum of four points on the heliostat mount frame are attached to cables with each cable under tension. Change in length of the cables causes the mirror to pivot about a dual-rotation mechanism with one axis of rotation always parallel to the ground, the y-axis, and the other axis, the x-axis, with pointing dependent on the rotation angle of the y-axis (see Figure 3.7). Since there are two always orthogonal axes, this type of mounting scheme has a full range of motion. Also, there is very little torque applied to the mounting pole by the mirror. However, the need for a high tension in the cables requires a thick supporting beam to mount the mirror onto. Additionally, correction of astigmatism may be complicated.

For a target-aligned mount, the manner of correcting astigmatism is obvious. Make the surface biconic with different radii of curvature in orthogonal directions, the radii of curvature determined by the Coddington equations (Eq. 3-17 and Eq. 3-18). Because of how the mirror is rotated in space the tangential plane always intersects the mirror in the same cross section of the mirror. For an altazimuth mounted mirror or a cable-drive mounted mirror the correction is not so obvious. The tangential plane does not always intersect the mirror in the same cross section. Rather it rotates about the vertex of the mirror. Thus, as the Sun moves throughout the day and the heliostat rotates in space to reflect the sunlight onto the tower receiver, the angle of astigmatism of the mirror needs to rotate independently either by physically rotating the mirror with an added axis of rotation, or deforming the shape of the mirror. Such a requirement appears drastic and expensive at first, but in the next chapter a simple and powerful modification to an alt-azimuth mounted mirror makes active focusing possible.

## 3.7 Conclusion

The current arrangements for power towers make it unfeasible to have both high-power generation capabilities and very high concentration. Either very large numbers of small heliostats acting as pinhole cameras are required, or a smaller number of larger actively focusing heliostats. To achieve the high concentration required for processes like synthesis of hydrogen fuel many small pinhole camera heliostats is required, in the tens of thousands. In contrast, only hundreds or thousands of focusing heliostats are required.

Previous attempts have been made to correct astigmatism of focusing heliostats, but solutions have been cumbersome and expensive. A common approach has been the target aligned heliostat where the mirror is set to a toroidal shape, which can rotate in space such that the tangential curvature is always in the tangential plane. The complexity of such a mounting scheme has kept it from being widely used.

A better step in the right direction is to fix astigmatism for an altazimuth mounted mirror. The requirement is then to rotate the shape of a desired toroid relative to the local axes of the heliostat mirror. Equations for this rotated shape are simple and straightforward. The next challenge is whether such shapes can be bent into a mirror, not just for setting the mirror shape. Active shape change is required for astigmatism to be corrected throughout the day.

# CHAPTER 4 : A PROTOTYPE ACTIVELY FOCUSING HELIOSTAT

## 4.1 Introduction

In this chapter the results of a real experiment show that the desired heliostat shape changes for actively focusing are possible on an altazimuth mounted heliostat. This was accomplished by mounting the mirror on a stiffening truss structure. Truss members could be lengthened or shortened in pairs by three linear actuators to bend the mirror into the desired shapes. Of course, this was not done without first knowing the shape of the mirror. Therefore, a non-null metrology system was designed and implemented for measuring the shape of the mirror for a variety of situations where the sag was changed by several millimeters. This metrology system has the potential to be used in situ (i.e. from a power tower). Additionally, a complementary in situ null metrology system is introduced.

Now that we have seen that an actively controlled shape heliostat is desirable for high solar concentration, a metrology technique for measuring that shape change is necessary. Existing methods for heliostat metrology have been concerned with measuring canting of flat mirror segments. Typical heliostats consist of many flat segments that are tilted in an overall concave shape. Though, shape change due to gravitational deflection is also of great concern. If there is concern about heliostat mirror shapes, this is generally measured in the factory by deflectometry or a laser array [11,40]. Canting a heliostat involves tipping and tilting the different facets (generally flat in shape) across the structure of a heliostat so that they form overlapping solar images (ideal canting).

Photogrammetry is a common technique for measuring the canting of a heliostat. Images of the heliostat are taken from a variety of orientations and by correlating the images the tilt of the facets relative to each other can be determined. This technique has reasonable accuracy (<1 mrad) and can even be used to measure gravity sag deflection. However, photogrammetry requires the camera to be relatively close to the heliostat being measured, and thus can be a lengthy process for a large field of heliostats. In contrast, edge detection techniques can obtain heliostat pointing and surface errors in a fraction of the time, though measurement uncertainties are often >>1 mrad [41].

Faster and more accurate measuring techniques are still an area of research for heliostat fields. A minimum absolute accuracy of 0.2 mrad is desirable. This number is somewhat arbitrarily provided. Taking a measurement with this accuracy, the ideal heliostat shape error of 1 mrad RMS is attainable. The shape error provided by heliostat manufacturers is generally defined for flat facets or curved facets in different manners. In the case of flat facets, 1 mrad shape error is associated with the pointing of the facets and the deviation from flatness of each facet. Similarly, curved facet users are concerned with deviation from the desired curvature and pointing errors. These errors together are ideally less than 1 mrad RMS. If these shape errors were defined relative to the ideal shape as defined in section 3.5, the surface errors are much greater. For example, a focusing heliostat that is reflecting light at 45° angle of incidence will have significant blurring of the solar image due to astigmatism. To make the example more quantitative, a 1.5 m diameter circular heliostat with 40 m focal length will have the spot shown in Figure 3.2. The effective shape error of the heliostat is like that shown in Figure 4.1. Assuming the spherical shape is perfect, and the pointing is perfect, the minimum RMS slope error for such a heliostat is 2.4 mrad, and the error budget is already used up.

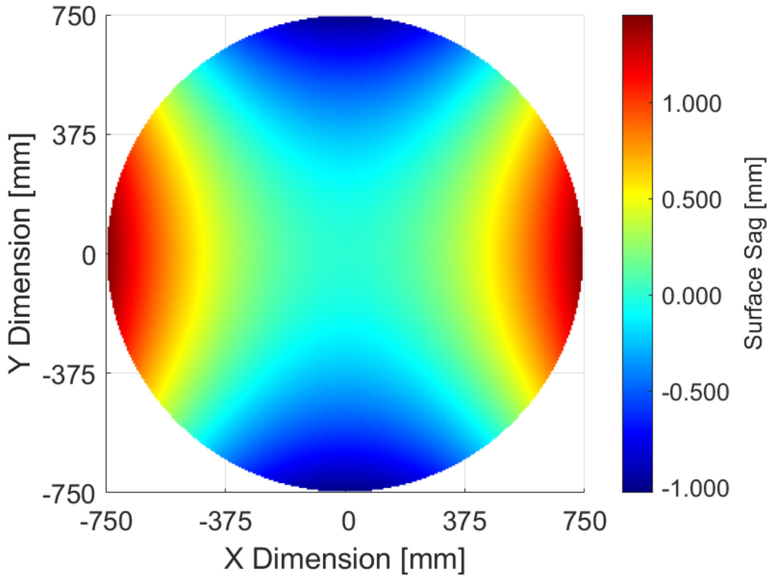

*Figure 4.1: Surface sag error for a fixed shape heliostat. The nominal radius of curvature is 80 m and the angle of incidence is 45°. The RMS slope error is 2.4 mrad.*

In the previous chapter an altazimuth mounted heliostat with adjustable shape was introduced. A project funded by Tech Launch Arizona led to the manufacture this heliostat along with a unique low-cost metrology system. In combination, the adjustable shape heliostat and metrology system were used to bend a flat piece of glass to the ideal toroidal shape with <1 mrad RMS absolute surface slope error, meaning the surface error relative to the ideal toroidal surface.

## 4.2 Adjustable Shape Heliostat on an Altazimuth Tracker

According to Eq. 3-15, three coefficients are required to define the ideal toroidal surface of a heliostat. Therefore, an adjustable shape heliostat must be able to change its shape in at least three ways. Additionally, the ideal heliostat shape is composed of functions which each have symmetry. Curvature is axially symmetric, oblique astigmatism is double-plane symmetric about a 45° axis and 135° axis, and vertical astigmatism is double-plane symmetric about the local x and y axes. Thus, it is possible to perform shape adjustment in three pairs, where the shape adjustment mechanism of each pair exhibits single-plane symmetry.

To preserve symmetry, each of the shape adjustment modes should be equally separated. In this manner, the ideal mechanism for shape adjustment is for a hexagon shaped heliostat where shape adjustment occurs at each of the 6 corners. The 6 corners are divided into 3 pairs, each with corners at 180° orientation, each pair adjusted with the same sag change. The performance of such a design was verified using ANSYS.

What is attainable from a heliostat mirror supplier is piece of flat back silvered glass. The average toroidal shape was bent into such a glass mirror by adjustment of 19 pad actuators, separate from the bending mode actuators. The bending mode actuators were used to bend the shape throughout the day relative to the preloaded shape.

An FEA model in ANSYS was created by Nick Didato where a flat piece of 3 mm thick glass was mounted on the 19 pads attached to a frame. Force was exerted on the 6 corners of the mounting frame such that the shape of the glass was bent towards each of the three required modes in turn. The maximum sag for each mode was set to 1 mm. The sag data for each type of bending was exported and further processed in MATLAB. A sag plot of each of the modes is shown in Figure 4.2 along with the sag errors for each mode. The RMS slope error in each case is close to 0.2 mrad RMS, well within 1 mrad RMS slope error.

The forces are exerted on the 6 corners of the frame by attaching a variable length strut to each corner with the other end of each strut attached to a back-center node. This back-center node consists of three linear actuators where each pair of 180° oriented struts attaches to one of the actuators, thus providing the means for changing the length of two struts in concert. In this manner a truss structure is formed. This structure is dual purpose. First, it allows the frame to be bent in the three independent modes, and second it stiffens the frame so that gravitational deflection is minimized. A linear combination of the bending of opposing corners in pairs can be used to obtain any of the three independent modes (see Figure 4.3).

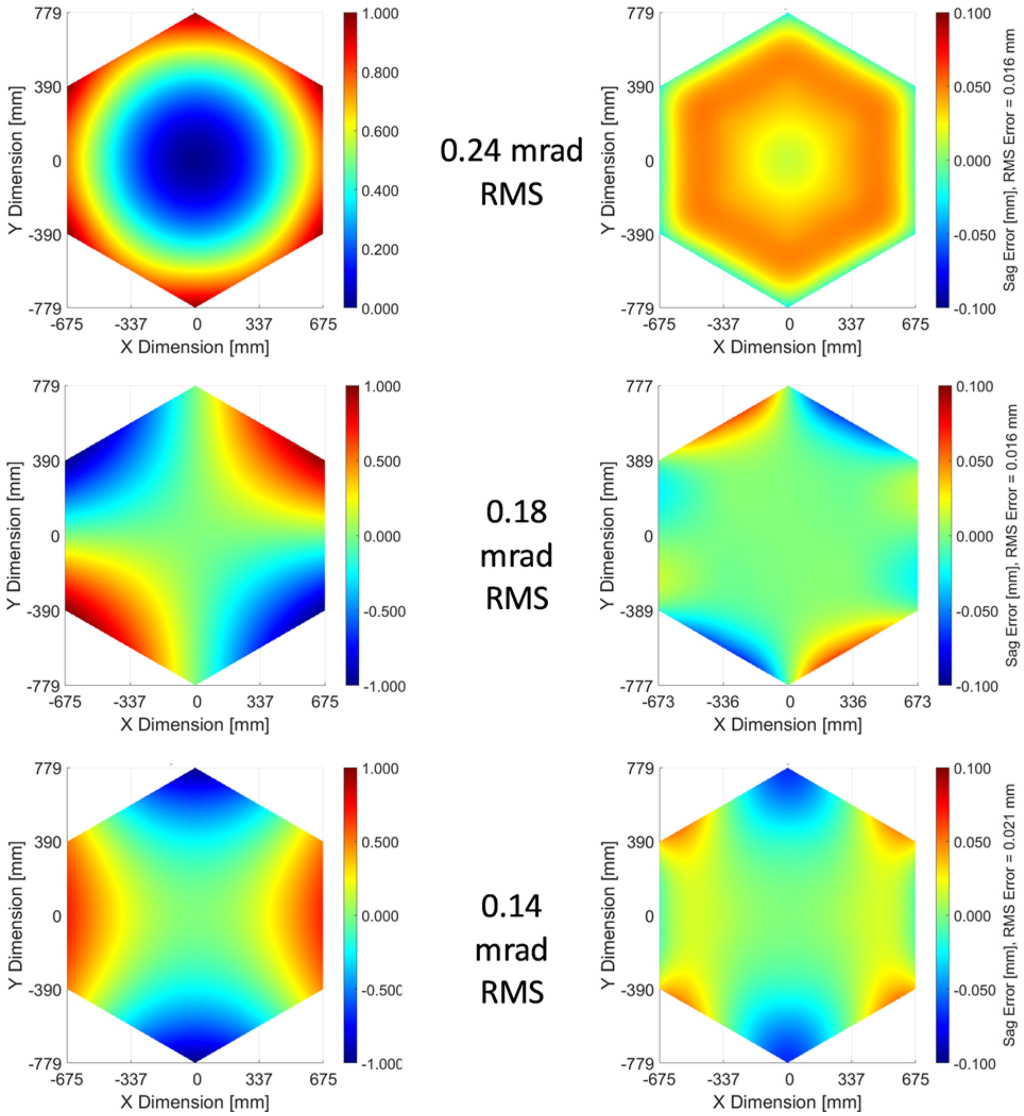

*Figure 4.2: ANSYS model of bending modes of a 3 mm hexagon shaped piece of glass mounted on 19 pads each attached to a hexagon shaped frame. Forces were exerted on the 6 corners of the frame in pairs. Each of the 6 corners needed to be adjusted in concert to obtain each of the desired bending modes independently. For the case of 1 mm maximum sag the RMS slope errors are close to 0.2 mrad for each of the bending modes. The left column is the net shape change, and the right column is the error in net shape change from the pure mode. The top row is for curvature ($X^2+Y^2$), middle row for oblique astigmatism (2XY), and bottom row for vertical astigmatism ($X^2 - Y^2$).*

As previously mentioned, the glass is mounted onto the frame with 19 pads, 18 of which were used to set the average toroidal shape. This is desirable for two reasons: the RMS slope error is less when the shape of the mirror is adjusted by the 18 pads, and the total shape change possible is greater when the initial shape of the mirror is near a median surface shape. This second reason

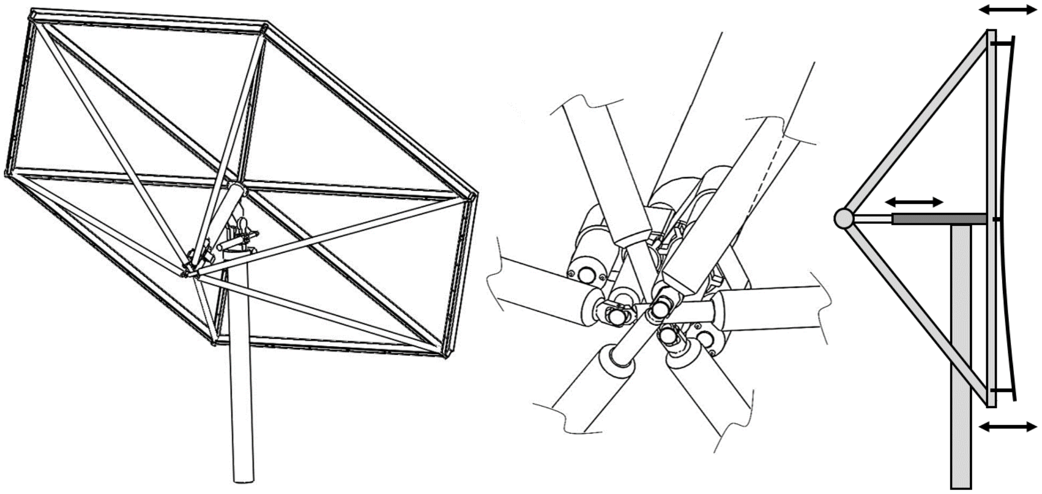

*Figure 4.3: Schematic of deformable shape heliostat mounted on an altazimuth tracker (left). Three pairs of struts are attached to the 6 corners of the heliostat and each pair attached to one of three linear actuators (middle). Cross section showing motion of one linear actuator causing the attached two corners to move by approximately the same change in linear actuator length (right). In this manner the 6 corners can be deflected by adjustment of the linear actuators, thus allowing curvature, oblique astigmatism, and vertical astigmatism to be induced into the surface independently.*

is because the linear actuators have a maximum force that they can exert. The maximum sag surface could not be achieved if the 3 linear actuators had to force the surface into the right shape beginning with a flat mirror. Therefore, a median surface shape was set by the mounting pads, and active adjustment of the mirror was accomplished with the 3 linear actuators, where the full range of desired surfaces was within the force limitations of the linear actuators.

A back view of the final structure is shown in Figure 4.4. The 6 struts are clearly visible along with the 3 linear actuators. The series of wires shown each go to motors attached to the 18 pads that were used for adjusting the initial shape of the mirror. This was chosen to increase the speed and accuracy of the initial shape adjustment but would not be required for a commercial version of this heliostat.

*Figure 4.4: Back view of prototype heliostat structure. The altazimuth tracking mechanism is visible along with the 18 adjustable pads and the 3 linear actuators, each attached to a pair of struts.*

This prototype heliostat should be viewed as a proof of concept. Many aspects of this design may make it too expensive for commercial heliostats, such as the slewing bearing dual-axis tracking mechanism, or the requirement to manually adjust the initial shape of the heliostat with an array of motors. With additional research into a commercial application of this heliostat the potential for a low-cost heliostat is there. For example, the use of a truss structure to stiffen the frame requires less steel than the traditional fish-bone structure. Cost is also less for the mirror since there is no need to make a curved surface via thermal slumping or grinding and polishing. Only a flat mirror is required, which is bent into the appropriate shape.

Having the heliostat structural requirements well defined led to the requirements for the metrology system. First, the heliostat shape change requirements were on the order of many millimeters. An interferometric null test was thus impractical, considering the shape errors that were inherently part of the mirror because of the type of structure used for mounting and bending the flat mirror into shape. A deflectometry non-null system could have been used for measuring the mirror shape, but this would have required a large distance from the mirror to keep the measurement near the center of curvature, or possibly a very large display used at a closer distance. The accuracy of a deflectometry measurement would have been very good, perhaps too good. Such a metrology system may have been like purchasing an airplane to fly from your house to the grocery store. What this heliostat needed was something far less accurate, only 0.2 mrad!

Defining the surface information needed for a successful prototype is helpful for determining the type of measurement. First, the beginning surface is a piece of flat glass. This heliostat used glass provided by Rioglass Solar with <1.0 mrad RMS flatness. The additional surface errors caused by bending the glass could then only occur at the pads and between pads because the beginning surface was continuous. To properly sample the spatial changes of the surface, the frequency of the measurement needs to be higher than the frequency of the pads. The hexagon with three pads on a side then needs to be measured by at least four lasers on a side, thus requiring 37 lasers (see Figure 4.5).

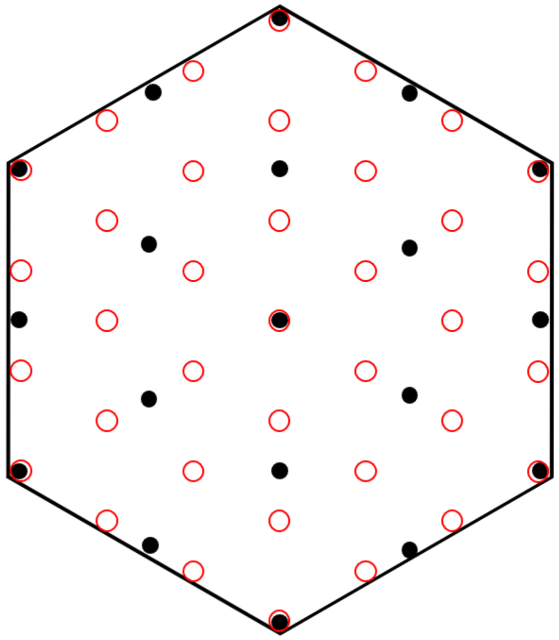

*Figure 4.5: Minimum number of sampling points required to determine sag shape. The mounting pads are shown as black filled circles and the sampling points are shown as red outline circles. This sampling is determined by the ways the shape can be adjusted. The sampling needs to be at least twice the frequency of the pads.*

In order to fit the approximately cubic curves formed along three pads, the surface needs to be sampled at a minimum of the pad frequency. However, this is similar to sampling at the Nyquist frequency of an optical system, therefore a higher sampling frequency is ideal. At much higher spatial frequencies more surface information is gained, though the ability to correct for such higher spatial frequency errors is not possible using the adjustable pads alone. Therefore, for the purposes of this experiment, only 37 sampling points were required. Thus, the idea of a laser Hartmann measurement was implemented.

## 4.3 Preliminary Laser Hartmann Measurement

The traditional Hartmann method involves placing a point source near the center of curvature of a concave mirror and covering the aperture of the mirror so that light reflects only from an array of holes. Thus, the pupil is sampled over a collection of discrete points. Two photographic exposures are taken near the focus of the mirror, one before the focus and the other after. Traditionally a well collimated light source has been used for Hartmann measurements, thus for a parabolic mirror there is ideally no spherical aberration observed [42]. However, measurement from the center of curvature is also possible. By correlating pairs of spots on the photographic plate the wavefront slope error at a particular hole (i.e. pupil position) can be measured (see Figure 4.6).

The problem with the Hartmann method is a significant loss of incident light, which leads to a lower signal to noise ratio. Additionally, creating an aperture mask with holes to cover meter class optics is rather cumbersome. Using the so-called Laser Hartmann method, these challenges of the traditional Hartmann method are overcome by using an array of lasers to sample the pupil. A high signal to noise ratio is then attainable and there is no need for a large covering for meter-class optics.

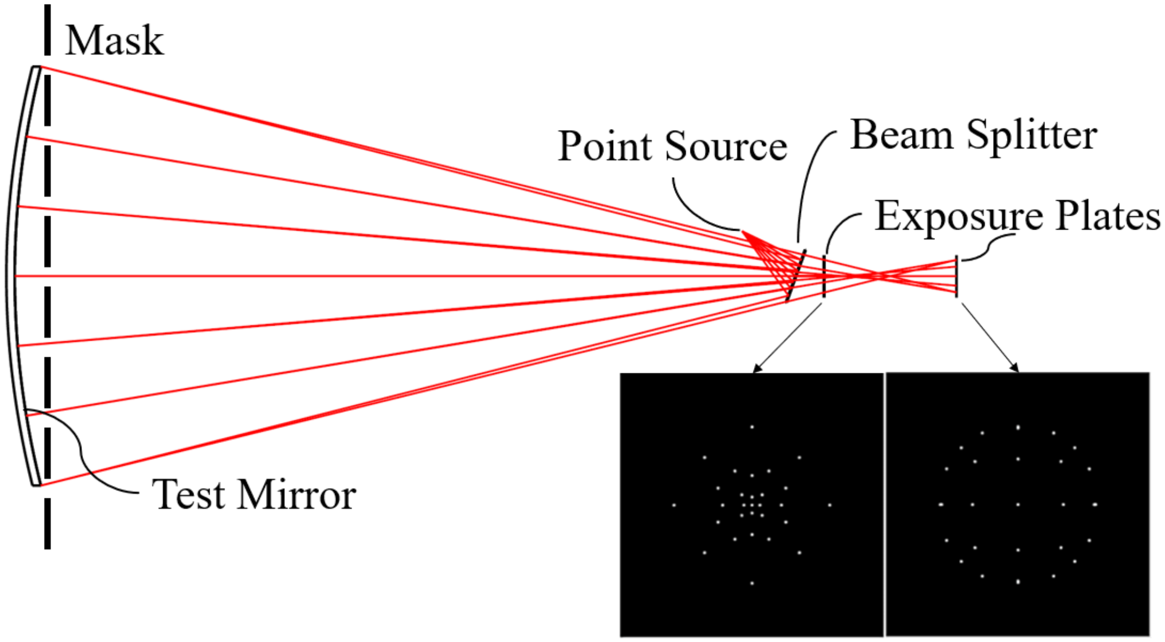

*Figure 4.6: Center of curvature Hartmann measurement layout. A point source is reflected into the beam path by a beam splitter. Light is reflected only across an array of holes due to a mask covering the test mirror. This reflected light then passes through the beam splitter and passes through two different exposure plates. By correlation of pairs of spots between the plates the surface slope error can be determined. In this case, a parabolic surface is being tested, thus spherical aberration is present.*

There are two different approaches to the laser Hartmann method. The first approach involves steering a single laser across the aperture and measuring the reflected spot location for each aperture position. The second method involves creating an array of lasers that are precisely positioned and passing each beam through an imaging lens to image the laser array onto the test mirror. An initial experiment was performed using this first method. A single laser was placed near the center of curvature of a mirror (150 m). A screen was placed close to the laser. Based on the reflected laser spots each associated with a pupil position, the slopes across the mirror were calculated, and the surface integrated (see Figure 4.7). The results of the experiment revealed a few important reasons why a fixed laser array was more desirable.

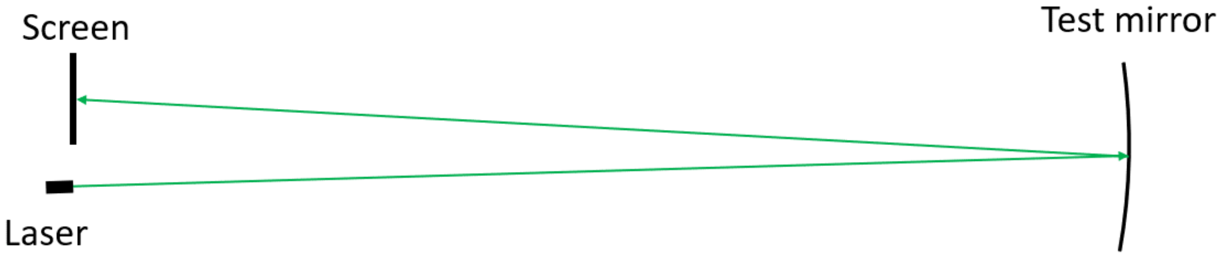

*Figure 4.7: Initial experiment with laser Hartmann metrology. A laser was steered to direct the beam to positions across the test mirror, and the reflected spot was measured at the screen. The distance from the laser to the mirror was 150 m.*

First, steering the single laser was time consuming. Each position required >20 seconds and two people. A measurement with 37 lasers would then require >10 minutes. This amount of time was not unreasonable, but the process was quite cumbersome. Second, a high level of mechanical precision was required (<1/4 of an arcminute). This involved using screw actuators on large cantilever beams held in place by springs. Making such a system that was automated would have been ideal but would have required additional time and funding. Third, the size of the free-space propagating laser beam expanded significantly over 150 m.

By gaussian beam propagation theory, the laser has approximately a spherical wavefront as it expands towards the test mirror. The laser used was 550 nm with a beam waist size of approximately 1 mm, found inexpensively online. The Rayleigh range of a gaussian beam laser is

$$Z_0 = \frac{\pi w_0^2}{\lambda}, \qquad \textit{Eq. 4-1}$$

where $w_0$ is the initial beam waist diameter and $\lambda$ is the wavelength. The Rayleigh range of a laser is associated with the distance at which the beam size has expanded to twice the area of the initial beam spot. When propagating a laser beam over a greater distance, the beam waist diameter is determined by

$$w(Z) = w_0\sqrt{1 + \left(\frac{Z}{Z_0}\right)^2}. \qquad \textit{Eq. 4-2}$$

In our experiment, the Rayleigh range of the laser was 5.7 m. Thus, the beam waist size can be approximated by

$$w(Z) = \frac{w_0 Z}{Z_0} = \frac{\lambda Z}{\pi w_0}, \qquad \textit{Eq. 4-3}$$

which shows that the beam waist size grows in proportion to the distance traversed when that distance is much greater than the Rayleigh range.

In the actual experiment the beam expanded from approximately a 1 mm spot to 1”, close to the prediction of gaussian beam theory of 20 mm. If the mirror had been perfectly flat, then the beam would have been ~52 mm when it reflected back to the screen. If the mirror had been perfectly spherical then the beam should have been near 1 mm, the same as the output. However, the mirror was mounted in a similar fashion to the final heliostat, glued on a series of pads, which bent a flat mirror into the ideal shape. This naturally introduced errors into the surface.

Using a FARO arm the initial shape of the mirror was set. Based on surface measurements, there was a periodic ripple across the surface of the mirror with a PV amplitude of approximately 0.4 mm. Modelling this in Zemax (using Chebyshev polynomials) shows that the geometric spot size (see Figure 4.8) is much greater than the ideal return beam size of 1 mm. The beam grows to ~40 mm. Yet in the measurement process, the observed laser beam size was even larger (see Figure 4.9). The core of the spot was about 1 foot in diameter surrounded by

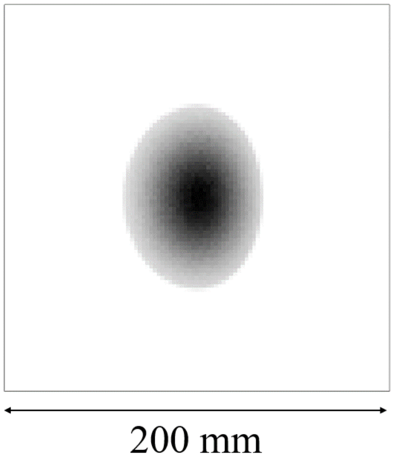

*Figure 4.8: Geometric spot for 150 m radius of curvature heliostat with periodic ripple. The ripple was modelled using Chebyshev polynomials. The maximum size of the beam grows from 1 mm at the laser to ~40 mm at the screen.*

many fluctuations. This is much greater than what was expected, and thus deserves some explanation.

The heliostat mirror for this experiment was a piece of glass that was intended for architectural use. Therefore, high frequency ripples could have been present across the surface. This is the most likely reason for the beam spread. Additionally, there was dust covering the mirror because it had been outside for several days. This caused the fringes observed in the laser spot because the screen was located at the ideal focus of the mirror (i.e. the Fourier transform of the aperture was located at the screen). One other explanation is wind. The wind was blowing, which caused the heliostat to vibrate during each measurement and caused deviations in the laser beam path. Thus, parts of the laser beam refracted away from the core.

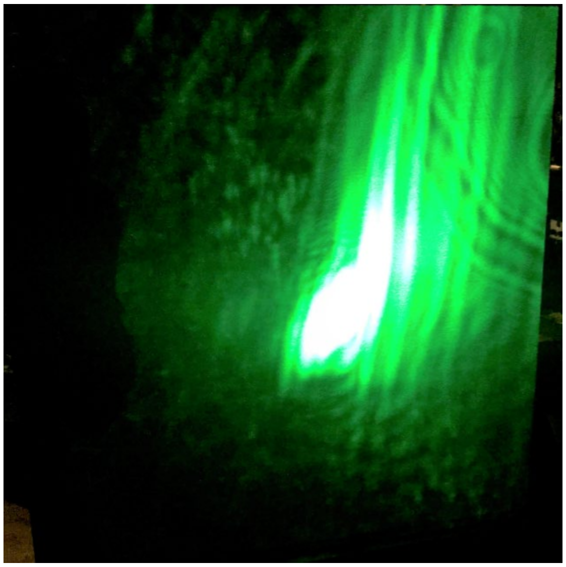

*Figure 4.9: Laser spot formed near center of curvature of a heliostat mirror. The picture is approximately 4 feet square.*

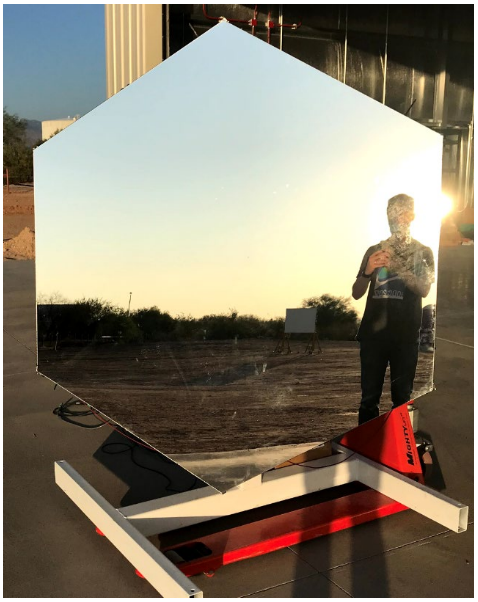

*Figure 4.10: Front view of prototype actively focused heliostat.*

Despite this large spot size, it was possible to measure the surface of this heliostat using this laser Hartmann metrology method. Low order surface errors were measured to within 0.5 mrad, which was less than the desired 0.2 mrad. Given the large increase in spot size and the tedious nature of moving the laser beam manually, modifications were made to this experiment to increase the speed and reduce the environmental factors affecting the measurement. Thus, a fixed array of lasers was used to measure the final heliostat (see Figure 4.10).

## 4.4 Changes to Laser Hartmann Measurement

The traditional Hartmann measurement involved photographic exposures a few minutes each, also requiring very careful placement of the films so that the measurement was accurate. The time for measurement can be optimistically approximated as ~10 minutes, most of which was idle. This is of course the physical measurement only, not the time to setup the experiment. The mechanical laser Hartmann measurement required >10 minutes for a full aperture measurement, most of which was active, though the process could be automated. In contrast, using a laser array controlled by a computer, it is possible to obtain a Hartmann measurement of a heliostat mirror in a couple seconds. In addition to changing the movable laser to a fixed laser array, a few beneficial changes were made to the experiment.

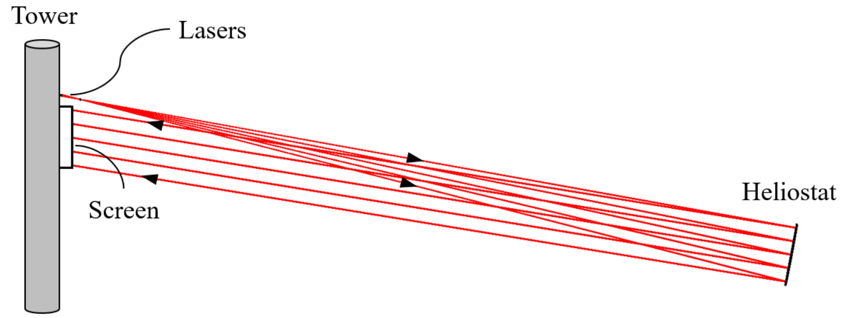

*Figure 4.11: In situ metrology system using the laser Hartmann technique. Lasers, mounted to a power tower, are near the focus of a heliostat, and direct beams onto the heliostat. Light is reflected from the heliostat and is incident upon a screen. Positions of the spots on the screen are recorded and slope errors of the heliostat can be calculated.*

One change to this experiment was making it truly in situ. Heliostats reflect sunlight towards a central tower. Therefore, an in-situ measurement involves measuring the shape of the heliostat from the tower. Thus, the lasers for this Hartmann measurement would ideally be placed at the focus of each heliostat (see Figure 4.11). For a spherically shaped heliostat the returning beams would then be collimated and spread across an area similar in size to the heliostat.

In reality, shape errors spread the beams even more and the ideal screen should be twice the size of the heliostat. The addition of a large screen is not ideal, but there are significant advantages to this geometry. By placing the lasers at the focus of a heliostat, the effects of any shape errors are reduced by a factor of two (traversing half the distance compared to a center of curvature measurement). Thus, the spot size increase due to high frequency slope errors is less. Also, all the heliostats in a field can be measured from the same location. An additional advantage is that the spot on the screen is no longer the Fourier transform of the pupil (i.e. fringes from dust particles are not observed). Clearly, this geometry is more favorable provided the screen does not become too large.

In this experiment, there were still complications with using high quality lasers alone. First, the total cost of a laser array composed of 37 high quality lasers is in the thousands of dollars. Second, each laser needs to be angularly positioned with high accuracy. Third, using such an array on a heliostat field would require motion of each laser when measuring heliostats at different distances.

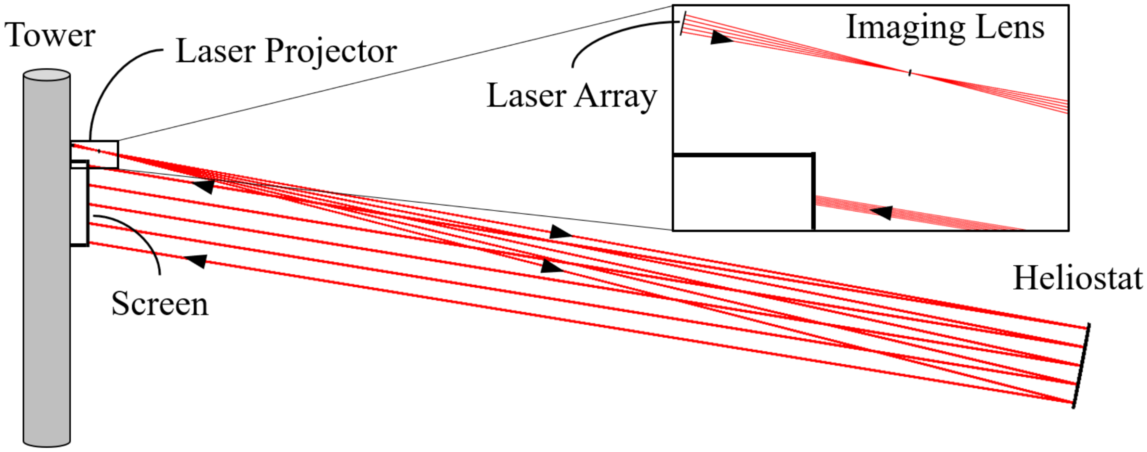

*Figure 4.12: For the in situ laser Hartmann metrology system, an imaging lens acts as a projector to focus the laser beams onto the surface of the heliostat. In this manner the gaussian beam expansion of the laser is reduced, and the only precision required is in the placement of the lasers.*

A simple optics trick was used to get around these problems by using a lens to image an array of cheap diode lasers onto the heliostat (see Figure 4.12). The advent of the diode laser has led to the high-volume production of monochromatic, reasonably collimated, bright, and inexpensive light sources (Figure 4.13). The laser size is 3 x 1 mm and the divergence varied between 1 and 5 mrad.

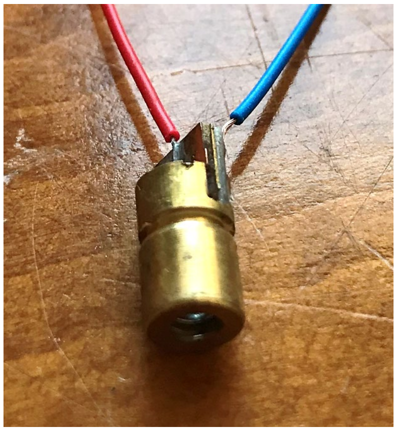
*Figure 4.13: $0.67 diode laser, 635 nm*

Aiming an array of lasers at a lens is straightforward and does not require high precision. In fact, using a lens means the laser does not even need to be well-collimated! Thus, the array can be composed of laser diodes and the cost can be significantly reduced. The only precision needed is in the machining of the laser array.

The imaging lens is essentially acting like a projector lens, where the selection of the lens is determined by the desired magnification. For a good sampling, the spot size of each laser would ideally be similar to the size of the output laser. However, if this were the case then any angular divergence in the initial laser beam would be similarly present in the beam reflecting from the heliostat. Étendue is the name of the game. Some of the purchased diode lasers had a beam divergence of ~5 mrad. Across distances >100 m such a beam would expand to > 0.5 m and the spot would be challenging to detect. Of course, there is also the practicality issue associated with using a lens with a >25 m focal length, which would be required for one to one imaging. Therefore, it is advantageous to select a lens that magnifies the size of the spots.

For example, magnifying the laser size by a factor of 20 with a lens reduces the divergence of the beam by the same factor. Thus, for the worst-case laser (5 mrad divergence), the beam divergence would be 0.25 mrad and the beam would expand by about 1” across 100 m rather than half a meter. This comes with the cost of a much coarser sampling of the heliostat, but sampling across ~1” sections on the heliostat mirror was all that was required for this experiment. Due to gaussian expansion this is in fact close to the best that could be done with a 1 mm aperture higher quality laser.

This smaller divergence of the laser beam can also be explained by gaussian beam propagation theory. Imaging the lasers onto the mirror creates the equivalent situation of a series of large lasers emitting from the heliostat mirror with the angular direction determined by the local slope of the heliostat mirror. In this manner, the initial gaussian beam waist is 1”. Thus, the Rayleigh range is >5 km. The gaussian beam expansion is very small across distances of a few hundred meters. The only added expansion of the laser beam is associated with the surface error of the mirror.

The initial experiment used architectural mirrors with large high frequency slope errors. The final experiment used mirrors from Rioglass Solar, which are intended for heliostat use. With an initial slope error <1 mrad, the laser beam would in the worst case expand by 100 mm across 100 m. The low order slope errors associated with the bending of the heliostat mirror only change the direction of the beam, not the size. There is of course a caveat to that statement. The locally induced curvatures across the mirror are generally toroidal due to the ideally toroidal shape of a heliostat at large angles of incidence. Therefore, local astigmatism in the surface causes the beam shape to be altered slightly, but this effect tended to reduce the spot size rather than increase it.

## 4.5 The Laser Array

For the actual measurement of the fully functional heliostat, the focal length of the heliostat was chosen to be 40 m. According to FEA analysis by Nick Didato, this was a good focal length for high concentration while minimizing surface errors. Thus, the laser beam expansion in the worst case was 40 mm (if the high frequency errors in the heliostat mirror were 1 mrad), and essentially nothing due to gaussian beam propagation.

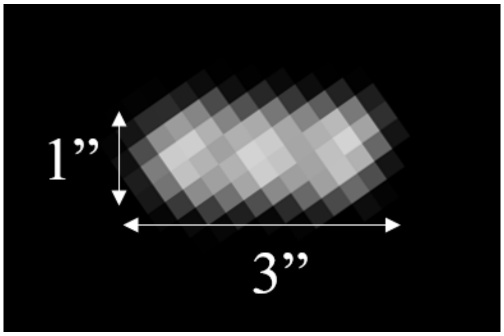

*Figure 4.14: Spot size at the mirror. Note, pixels with values less than half the maximum pixel value were filtered to reduce the effects of stray light. Thus, the full size of the spot is not shown.*

The diode lasers used in this experiment were of an interesting form where the spot size was rectangular in shape with 1 mm by 3 mm diameter at the laser, though the laser aperture was axially symmetric and about 3 mm in diameter. The imaging lens was imaging the laser aperture; thus, the size of the laser spots was determined by the laser aperture, not the size of the laser spot. Somewhat arbitrarily, to obtain 20X magnification of the lasers the ideal focal length lens was 2 m and the beam sizes at the mirror were roughly 2.5” (see Figure 4.14). This was not a problem because the Hartmann slope calculations rely upon the centroid of the spot.

Concerning the focusing lens, in the worst-case beam expansion of 5 mrad a laser spot is ~1” in diameter, thus a 1” diameter lens was suitable. Most of the lasers were roughly the same size at the lens as when they exited the laser (~3 mm). Thus, the lasers needed to be positioned only with ~1/3 of a degree precision, almost two orders of magnitude less precise than in the mechanical laser Hartmann experiment. In this manner, the lasers were placed in precision machined holes and glued in place with UV curing glue, all by hand (Figure 4.15). The distribution

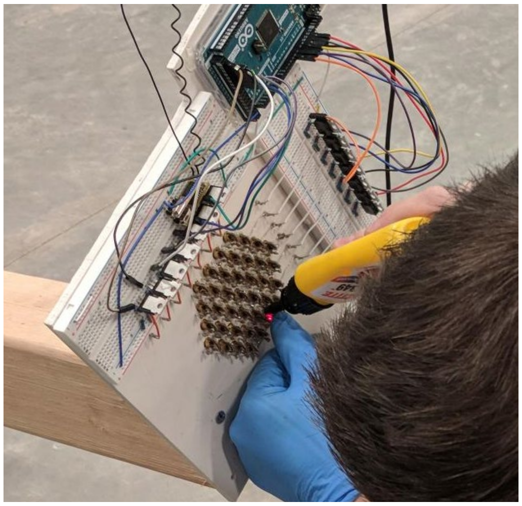

*Figure 4.15: Picture showing the process for aligning laser diodes and gluing them in place.*

of the holes was determined by the magnification of the imaging lens and the shape of the heliostat, which was hexagonal.

Simply turning on each of the lasers in turn via the laser controller and observing their location within the lens was all that was needed to verify alignment. Turning on all the lasers together showed that most of the laser light was passing through the clear aperture of the lens. Additionally, a projected pattern of the lasers onto the heliostat mirror, made visible by an array of overlaid Lambertian surfaces, showed that the image of the laser array was properly formed on the heliostat mirror (see Figure 4.16).

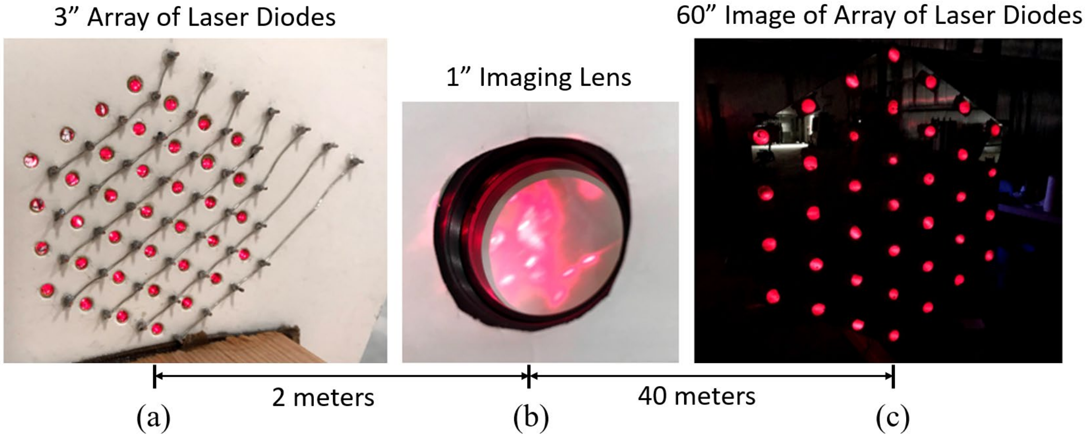

*Figure 4.16: Laser projector detail. (a) Laser array composed of diode lasers each turned on. (b) Laser spots with most of the light passing through the clear aperture of the lens. (c) Projected laser spots incident upon the heliostat mirror. The distribution of diode lasers was chosen according to the shape of the heliostat mirror and the magnification provided by the imaging lens.*

Creation of the laser controller presented unique challenges itself. First, it was determined that to uniquely identify each spot for a measurement, each laser needed to be turned on sequentially. This was necessary because in many situations the laser spots were intersecting on the screen. Thus, it was important to be able to quickly turn on and off each laser in a precisely timed manner. An Arduino Mega 2560 was suitable for this, especially since the diode lasers only required 5V to function. Therefore, an Arduino by itself could control the lasers by turning on and off digital output pins. However, controlling 37 lasers each with their own circuit would have been very messy. It was determined that N-type MOSFETs should be used in an array controlled by the Arduino.

An N-type MOSFET is essentially a variable resistor dependent on the input voltage to the “gate” pin of the MOSFET. FQP30N06L N-type MOSFETs were used because when applying a 5V voltage to the gate, the resistance of the MOSFET is nearly zero, and when no voltage is applied to the gate (0V) the resistance is very large (see Figure 4.17). If used as a supply to a laser, the “source” pin is connected to the 5V voltage supply of the Arduino and the “drain” pin is connected to the positive lead of the laser. If used to close the circuit, the “source” pin is connected to the negative lead of the laser and the “drain” is connected to ground. The number of lasers that can be controlled then goes as the square of the number of pairs of MOSFETs.

*Figure 4.17: FQP30N06L N-type MOSFET*

This is illustrated in Figure 4.18. This figure represents an example circuit showing how to control 25 lasers with 10 digital input pins of a microcontroller. Five positive lines in red are created, each activated by their own MOSFET. Five negatve lines in blue are also created each with their own MOSFET. The red circles in the 5x5 array are each connection points for the

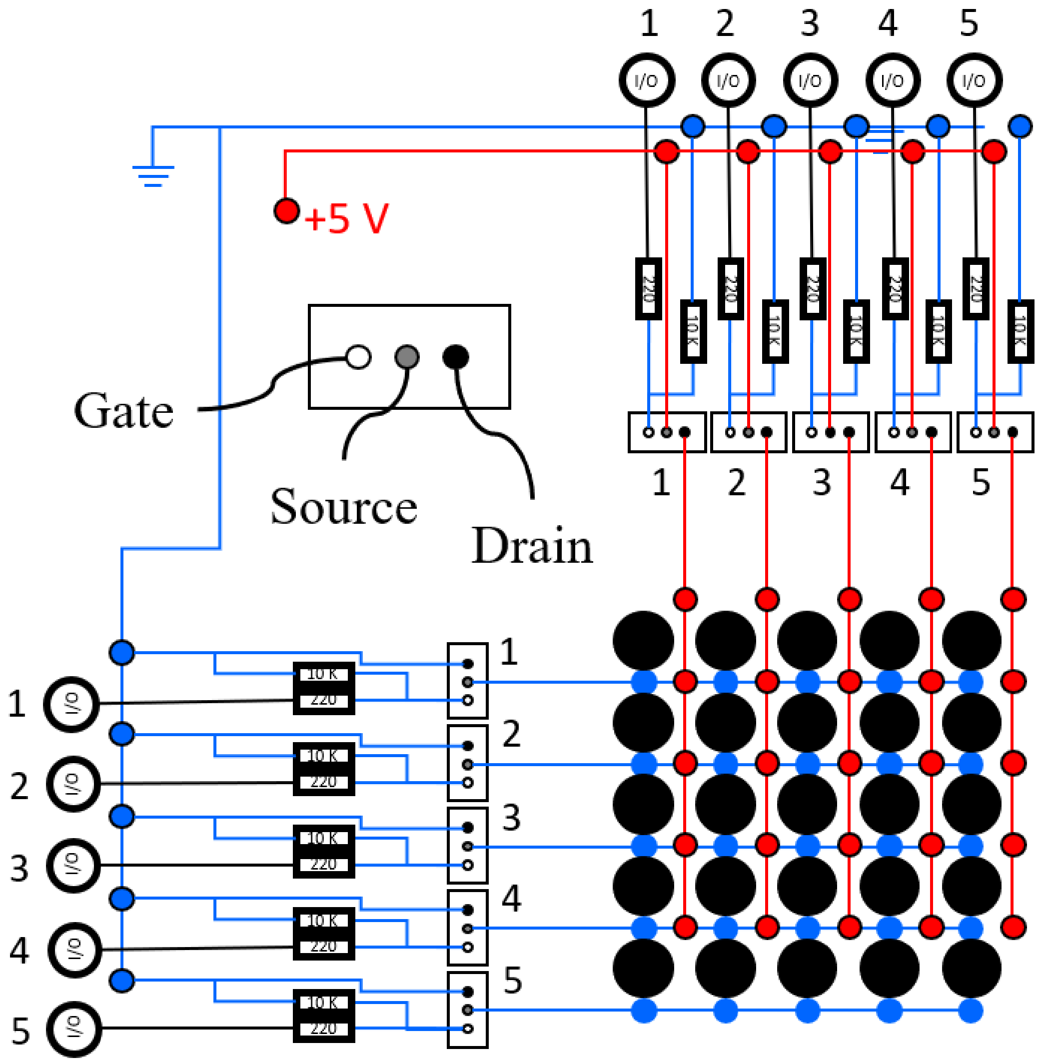

*Figure 4.18: Example circuit showing how to control 25 lasers with 10 digital input pins of a microcontroller. Resistors are used to ensure digital pins are not overdrawn on current, and to ensure the gait voltage drops to zero when the digital pin turns off. Five "hot" lines are created, each activated by their own MOSFET. Five "cold" lines are also created each with their own MOSFET. The red circles in the 5x5 array are each connection points for the positive lead of a laser diode, and the blue circles in the 5x5 array are each connection points for the negative lead of a laser diode. If the pin in column 2 turns on, then the red wire in column 2 becomes hot, but no current can flow because the resistance on all the blue lines is "infinite". If the pin in row 5 is then simultaneously turned on, the resistance in the blue wire in row 5 drops to nearly zero and current can flow through the laser diode.*

positive lead of a laser diode, and the blue circles in the 5x5 array are each connection points for the negative lead of a laser diode. If the pin in column 2 turns on, then the red wire in column 2 becomes hot, but no current can flow because the resistance on all the blue lines is "infinite". If the pin in row 5 is then simultaneously turned on, the resistance in the blue wire in row 5 drops to nearly zero and current can flow through the laser diode in row 5 column 2.

Using this type of arrangement, the number of lasers that can be controlled is equal to the number of row pins times the number of column pins. Thus, if a laser array were made for a large 36 $m^2$ heliostat, and 400 lasers were needed to obtain the desired sampling, only 40 pins would be required, and the laser array could be controlled by one Arduino Mega 2560. In the actual arrangement only 37 lasers were needed, thus only 13 pins would have been required. However, to simplify circuitry 14 pins were used, which could have controlled 49 lasers. Due to the geometry of the heliostat (i.e. the heliostat being hexagonal), the corner lasers were unnecessary and only 37 lasers were required. The gridded approach was still used due to its clean wiring.

## 4.6 Measurement Calculations

The laser array was only one part of the full metrology system. The rays reflected from the heliostat mirror needed to be sufficiently visible on the receiving screen so that a scientific camera could capture an image of each spot. A Mako U 1.3MP monochrome camera was chosen using a 35 mm F/1.65 fixed focal length C series lens from Edmund Optics.

The size of the screen was 8 ft by 8 ft, close to twice the size of the hexagonal heliostat (1350 mm flat to flat). The separation of the heliostat and screen was close to 120 ft with the screen and laser array near each other (see Figure 4.19). A retroreflective material was used for the screen so that spots were very visible when the camera viewed the screen from the heliostat direction. Mapping the screen onto the camera sensor gave a resolution of about 2.4 mm per pixel; plenty of resolution to measure the >2” laser spots. The maximum speed of a single measurement was throttled by the maximum frames per second of the Mako U camera, which was ~160 FPS.

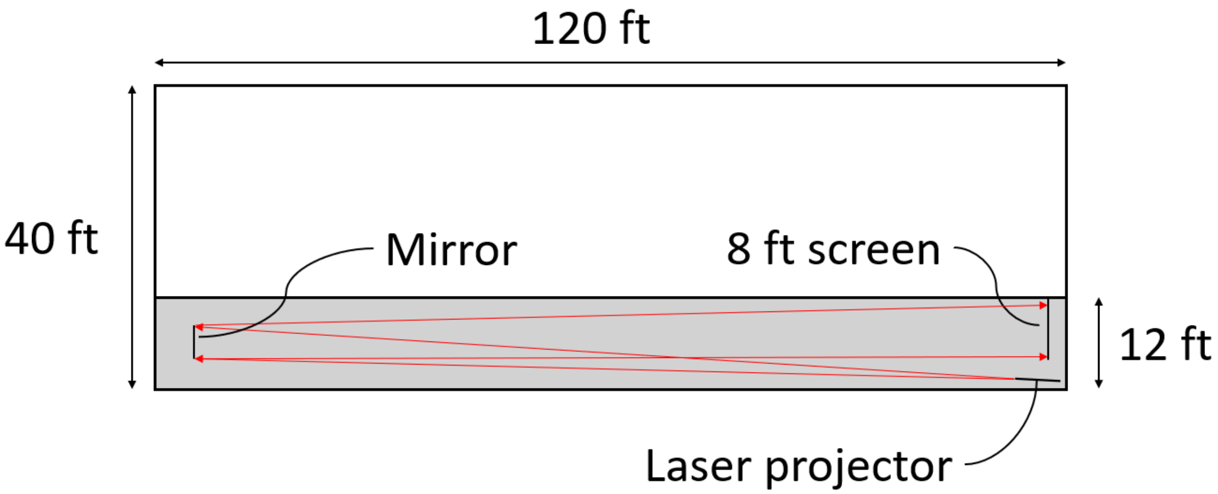

*Figure 4.19: System setup for laser Hartmann measurements.*

Additionally, the camera operated with significant fluctuations in FPS. Due to the poor timing of Windows 10, the camera needed to take two pictures for each laser flash to guarantee an image was captured when one of the lasers was on. Thus, for 37 lasers a minimum of 74 images was required. At such a speed, the physical measurement took less than one second. Note, the Arduino laser controller could flash lasers at >1000 times per second, but this would require a poorly timed camera to take images at 2000 FPS. The exposure times would then be ~1/2000th of a second, perhaps too short to obtain good data.

To calculate the local slope across the aperture of the heliostat a knowledge of the geometry of the laser array, heliostat, and screen were necessary. The calculation then involved referencing the positions of all the spots relative to the center spot position. In order to measure the center spot positions, the centroid of each spot was calculated. This involved a weighted sum of the pixel values where the weighting factor was the pixel position. Converting the pixel positions to real space distances then provided the physical location of the laser spots on the screen. These centroid calculations for the x and y dimensions were simply

$$Cx = \frac{\sum P(x_i)x_i}{\sum P(x_i)} \text{ and} \qquad \textit{Eq. 4-4}$$

$$Cy = \frac{\sum P(y_i)y_i}{\sum P(y_i)}, \qquad \textit{Eq. 4-5}$$

where $x_i$ and $y_i$ are the pixel numbers/positions and $P$ is the pixel value at the associated pixel positions. Thus, the laser spot locations on the screen were measured, and the slope could be calculated.

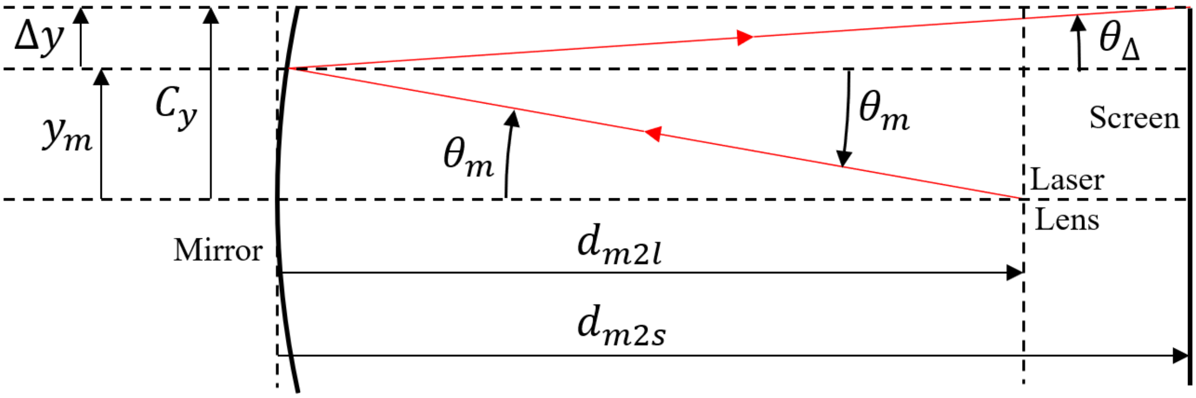

*Figure 4.20: Geometric illustration of the laser path from the laser lens to a pupil position in the mirror to the screen. This path forms a triangle with an apex angle that is twice the slope of the mirror.*

The slope calculation was performed in two dimensions independently. In Figure 4.20, a beam leaving the laser lens traverses the distance from the laser lens (imaging lens) to the mirror. This distance is very large compared to the sag of the mirror; thus, the sag can be neglected (especially since all that was needed is 0.2 mrad precision). The laser then reflects from the mirror and traverses the distance from the mirror to the screen, which is not necessarily the same distance as from the lens to the mirror. The laser is incident upon the screen and measured and the location of the laser spot is calculated. A triangle is formed by this path with an apex angle that is twice the slope of the mirror at the reflected location. Therefore, the equation for the slope of the mirror at a given pupil position is

$$S_y = \frac{y_m}{2d_{m2l}} + \frac{\Delta y}{2d_{m2s}}, \qquad \textit{Eq. 4-6}$$

where $y_m$ is the marginal ray height, $\Delta y$ is the change in height of the laser from the marginal ray height, $d_{m2l}$ is the distance from the mirror to the lens, and $d_{m2s}$ is the distance from the mirror to the screen. Due to the need to separate the lens from the return laser beam path, the actual geometry involves offsetting the screen and laser lens, and the marginal ray heights and change in ray heights are all referenced relative to the central beam (see Figure 4.12).

With the slopes calculated, the RMS slope error for a given measurement was readily apparent. However, this RMS slope error was only for the low frequency shape errors in the mirror. The initial high frequency errors of the mirror were neglected. Knowing the slope error did not make it easy to know what the sag error in the mirror was. Knowledge of the sag error was necessary for knowing how to change the actuators' settings. Therefore, software from Brookhaven National Laboratory was integrated into the software to take the slopes in x and y and their associated positions on the mirror. From this information the slopes were integrated to form a full surface map [10]. Due to the low sampling of the mirror, the software did not provide accurate results. To fix this, the slopes were cubic interpolated using MATLAB's built in function, griddedInterpolant, before being integrated.

## 4.7 The Laser Hartmann Measurement

The laser Hartmann measurement thus consisted of the following steps: establish the geometry, align the laser array to the mirror, adjust the tip and tilt of the heliostat mirror to reflect the laser beams onto the screen, calibrate the camera, send a remote signal from the computer to the Arduino to run a preestablished program that flashes the lasers in sequence with a precalibrated timing, capture images with the camera, process the images to identify relevant data, calculate the laser spot centroids, calculate the slopes in two dimensions for all 37 laser spots, integrate the slopes with BNL software, compare the measured sag to the ideal sag, and calculate surface errors.

The setup time for a given measurement was in the vicinity of 30 minutes to an hour. This included determination of the ideal shape by entering a date, time, and geometry for the Heliostat on Sun. The ideal shape was thus automatically calculated in MATLAB. With everything properly setup in the software and hardware a single click initiated a measurement. From that click to obtaining the surface error took less than 30 seconds, most of which was spent in establishing connections with the computer to the camera, connecting to the signal transmitter, sending a transmission, and post processing the data. The time over which the lasers flashed was less than 1 second. After connections were established the first time, additional clicks led to surface error measurements in less than 15 seconds.

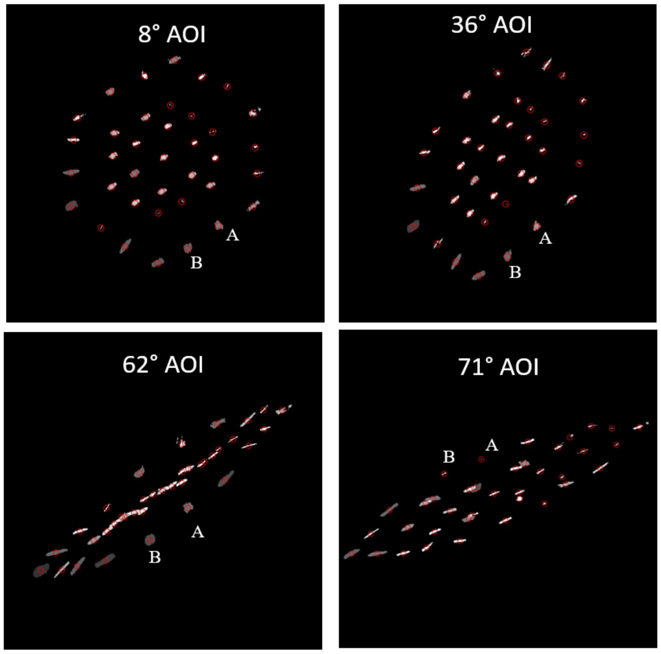

*Figure 4.21: Laser spot patterns on the screen for four different heliostat shapes.*

The process of adjusting the heliostat towards the ideal shape then became the bottleneck. The initial shape setting was the lengthiest process since all 18 pads needed to be adjusted sequentially. This would have taken >2 hours using the mechanical laser adjustment method. Using the laser array, the process took less than 30 minutes.

After establishing the initial shape of the heliostat, other shapes for different times of day were obtained by adjusting solely the three linear actuators. Again, the laser Hartmann measurement was used to quickly determine shape errors. This process was much faster than the initial shape setting. In this manner, the heliostat was set to four different shapes for four different

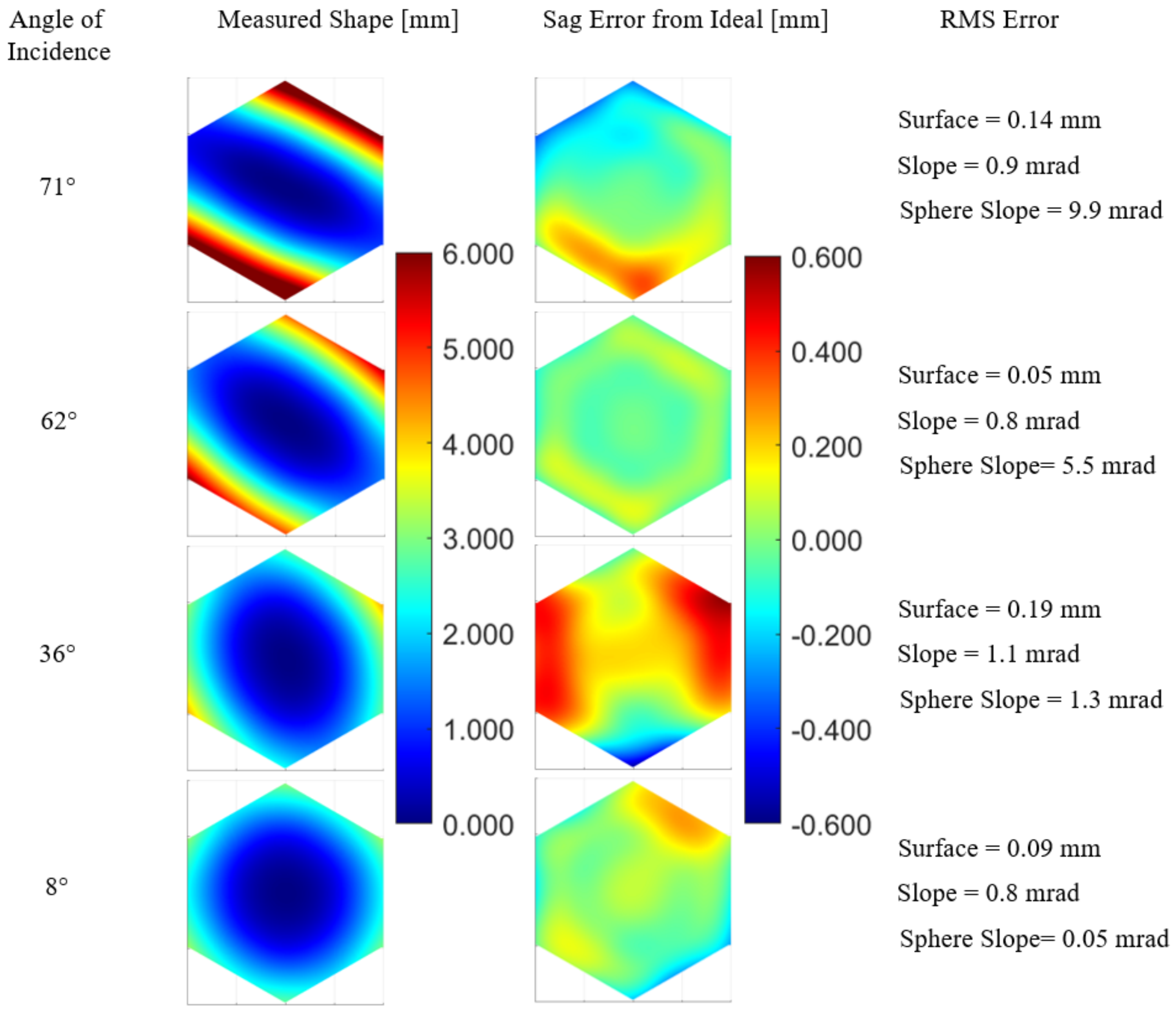

*Figure 4.22: Matrix of surface measurements showing the final adjusted shape of the heliostat for four different solar positions after iterations towards the ideal shape. Left column is angles of incidence, which vary from nearly on-axis to >70 degrees. The second column is the measured surface shapes, which vary from highly toroidal to nearly spherical. The third column is the surface shape errors. The fourth column is the RMS errors of the heliostat mirror for surface sag, surface slope, and the slope error if a perfect sphere were used.*

solar angles of incidence. The spot patterns on the screen for each of these shapes is shown in Figure 4.21 and the integrated surface shapes and errors are provided in Figure 4.22.

Three out of the four heliostat surface shapes had less than 1 mrad RMS slope error relative to the ideal surface shape (determined by Eq. 3-15 and Eq. 3-17 through Eq. 3-19). If the surface had not been actively bent into shape, and instead had been a perfect sphere, the RMS slope errors would have been as bad as 9.9 mrad. Even at a moderate angle of incidence of 36° the slope error of a perfect sphere is 1.3 mrad and the ideal error budget has been used up. Note, the surface slope errors consist of a coupling of the slope errors in x and y. All RMS errors were calculated by square rooting the mean of the square values minus the mean of the values squared, as in

$$\sigma_x = \sqrt{< x^2 > - < x >^2}, \qquad \text{Eq. 4-7}$$

where $x$ is the quantity under consideration. The total RMS surface slope error was then calculated by taking the modulus of the RMS slope errors in x and y.

After setting the heliostat surface shape as close as possible to the ideal shape, the next test was taking the heliostat out into the sunlight and focusing the light onto a target 40 m away. In this experiment the target was to the East. The Sun reflected at angles varying from 8 degrees to 71 degrees. The resulting solar images were well corrected and obtained concentrations of >90% ensquared energy into 0.5 m, a geometric concentration of nearly 6X over a large range of angles (see Figure 4.23). The heliostat was bent close to the ideal shape, and then allowed to relax to the initial set shape. In this manner, the benefits of bending a heliostat were manifest.

The solar images were each measured using the same scientific camera used for measuring the laser spots. A neutral density filter was placed in front of the lens so that the exposure did not

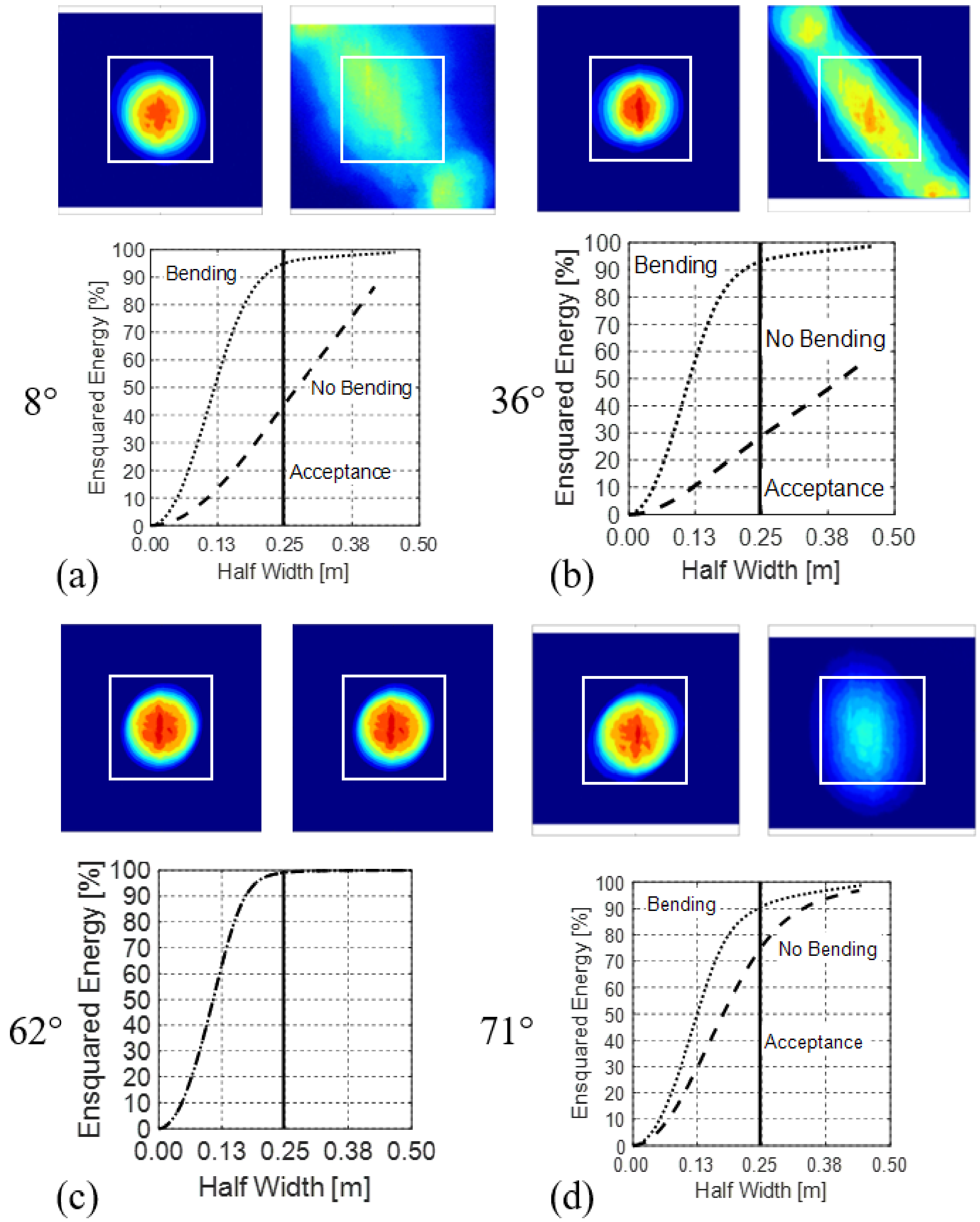

*Figure 4.23: Solar images for each angle of incidence considered categorized by subsections: (a) 8°, (b) 36°, (c) 62°, and (d) 71°. The left solar image of each section is what is obtained by bending the heliostat frame with the three linear actuators. The right solar image of each subsection is what is obtained when no bending is induced by the three linear actuators. Below each set of solar images is their approximate ensquared energy in both the bending and no bending scenarios. The white box is 0.5 m square and represents a potential region of acceptance.*

saturate the sensor. The ensquared energies shown in Figure 4.23 should be considered approximate since the measurement method and calculations did not consider precise radiometric quantities. An attempt was made to measure the screen with and without the solar image incident upon the screen, but due to a poor mounting scheme for the neutral density filter the background images could not be properly subtracted from the solar image measurements. Thus, a global subtraction of detector values was implemented where the subtracted value was determined by the average of a section of the target screen that appeared to not have any energy from the solar image.

The results of the laser Hartmann measurement clearly show that this method works. High solar concentrations were made possible by bending a heliostat mirror close to ideal toroidal shapes, active bending made possibly with only three linear actuators. It is possible to use this laser Hartmann metrology system in situ, opening the possibility for a power tower field of actively shaped focusing heliostats. Using such a field would allow for high concentration of sunlight using only a few hundred to a few thousand heliostats, thus making it possible to generate hydrogen fuel or increase the efficiency of power plants.

## 4.8 Future Metrology

The future of actively focusing heliostats is currently limited by heliostat metrology. If a rapid and sufficiently accurate metrology system(s) could be implemented, then the possibility of actively focusing heliostats becomes more concrete. In this section, a discussion of two commercial type heliostat metrology systems are proposed. The first is simply a modification of the metrology system already tested in a prototype setting.

A commercial laser Hartmann metrology system would need to be able to measure each heliostat in a large field, perhaps covering distances from ~50 m to ~200 m. Since it is ideal to keep the lasers all fixed in their pointing, such a system could use a zoom lens, where the outer elements act as a zoom beam expander (Donders telescope) and the back elements are fixed in relation to the laser array, acting as a telephoto lens. In the actual light path, a reverse telephoto

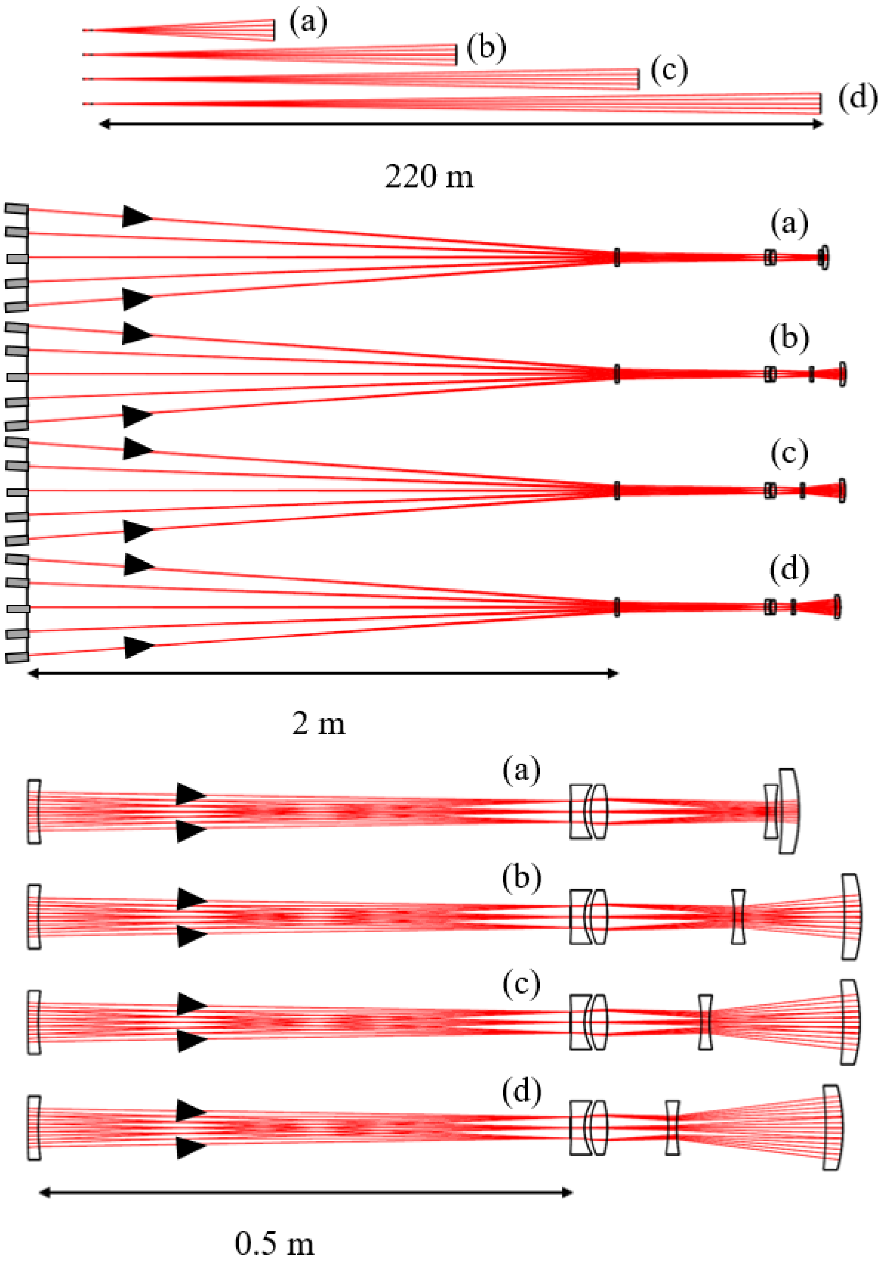

*Figure 4.24: Zoom lens used for laser Hartmann metrology at four different distances (a) 55 m, (b) 110 m, (c) 165 m, and (d) 220 m. The top images show the heliostat mirrors at the various distances in relation to the laser Hartmann metrology system. The middle set of images shows the laser diodes with positioning unchanged for each distance. The bottom set of images shows in detail the alterations to the lens between zoom positions. The only element distance that changes is between element 3 and element 4 and element 4 and element 5. A reverse telephoto lens is thus formed followed by a variable beam expander.*

lens images the laser array to a distant position followed by a variable beam expander that keeps the magnification constant for heliostats at varying distances (see Figure 4.24). The heliostat mirrors then reflect the laser beams to a screen near the laser array (perhaps mounted to the tower).

An inexpensive camera could then be mounted near each heliostat for measuring the laser spots, or a zoom lens mounted onto a drone could quickly move between heliostats for rapid measurements. In either scheme the measurement process would ideally occur at night where stray light is less likely to corrupt surface measurements.

A weakness of the laser Hartmann method is that it does not measure the gravitational deflection of the heliostat mirror, which varies with elevation angle. Ideally, the shape of the mirror should be measured when the heliostat mirror is oriented correctly to the Sun. Thus, a second metrology system is herein proposed, a solar wavefront metrology system (see Figure 4.25).

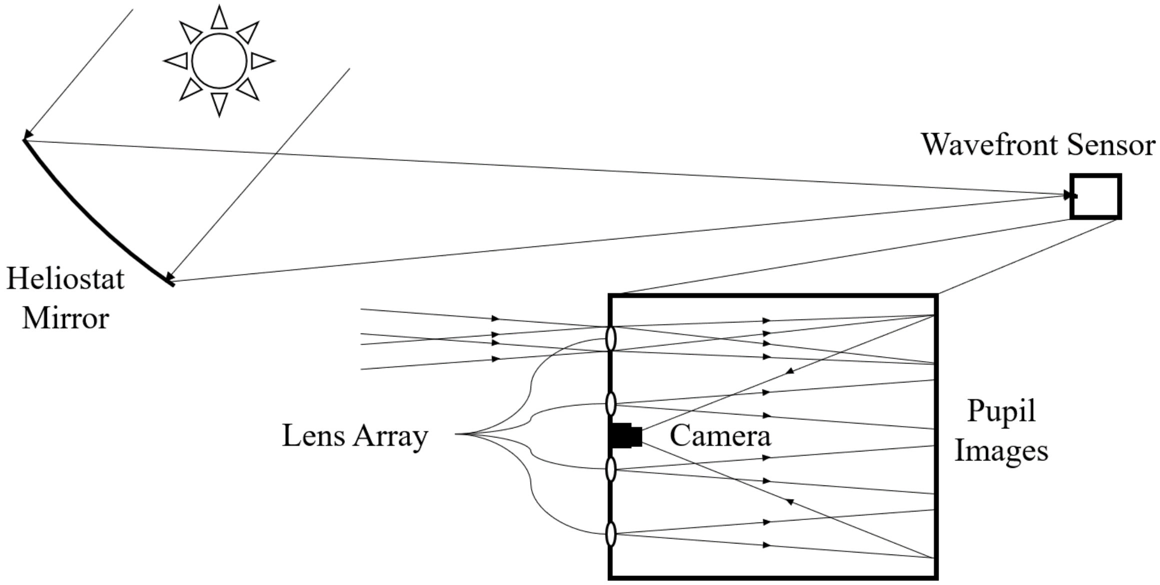

*Figure 4.25: Solar wavefront metrology system using sunlight to measure the heliostat shape in its operating condition where gravitational deflection comes into play. A solar image is formed by a heliostat on a distant wavefront sensor, at the tower near the receiver. The wavefront sensor consists of an array of lenses where each illuminated lens forms a pupil image. Measuring these images and processing the data leads to a slope error map, in a similar manner to a Pyramid scheme wavefront sensor.*

In the proposed metrology system, an array of small lenses is distributed throughout the focus of a heliostat mirror, where each lens illuminated by the heliostat forms an image of the heliostat. To do this, at the tower receiver this fly's eye array is placed just below the receiver to measure any heliostat by tilting the heliostat to reflect sunlight to this lens array. A camera is then used to measure the array of pupil images and dissects the images to form a slope error map across the heliostat in a similar manner to a Pyramid wavefront sensor (see section 5.2). This method of measurement is well explained visually (see Figure 4.26).

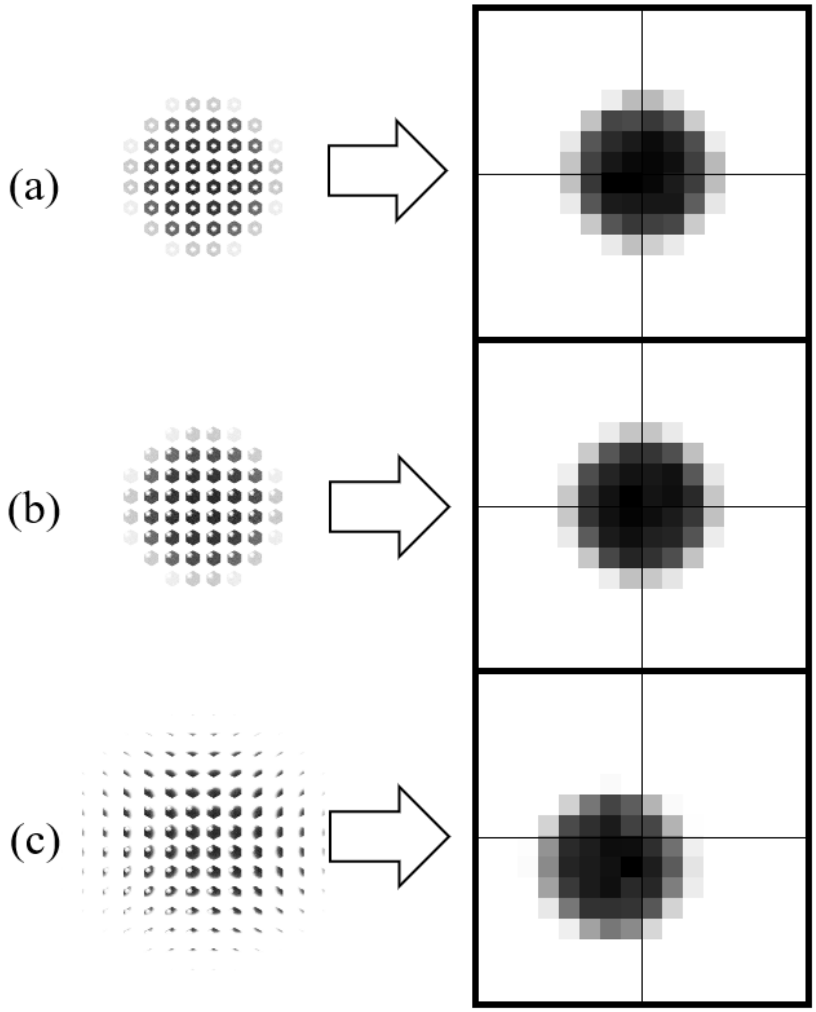

*Figure 4.26: An array of pupil images formed where an ideally shaped heliostat is used in (a) and (b) and an astigmatically aberrated heliostat is used in (c). Sampling the pupil image array in (a) at the center of each pupil image recreates a low-resolution solar image. Similarly, in (b) sampling an off-axis pupil position forms a low-resolution solar image that is centered at the same location. For (c) the same off-axis pupil location forms a solar image that is offset due to astigmatism in the surface. Thus, the slope error across a heliostat mirror can be measured one pixel at a time.*

If a heliostat were covered with a large mask so that only the central region was exposed, then that central region would act as a pinhole camera and form a dim solar image on the lenslet array. Each illuminated lenslet would then form a pupil image, which would be essentially a dot (i.e. the exposed region of the heliostat). This array of dots could be directly correlated to the solar image. Thus, a low-resolution solar image could be recreated for that pupil position.

Now consider a mask where only an off-axis section of the heliostat mirror is exposed. If the heliostat mirror was the correct shape, this off-axis section would form a solar image centered at the same location as the on-axis solar image. The slope error for this off-axis section would then be zero. Perhaps the shape of the mirror had some incorrect astigmatism. Then an off-axis section of the mirror would form a pupil image that was offset from the on-axis solar image. Thus, this off-axis section would have a slope error.

Instead of sampling the heliostat slopes by blocking out everything but one small section at a time, obtaining an image of an array of pupil images provides the same information in one capture. By sampling an array of pupil images with the heliostat not covered, the location of the solar image formed by each pupil position can be measured. Using the centroid of each of these solar images, a slope error map can be formed relative to the on-axis pupil position, and these slopes can be integrated to form a surface map (see Figure 4.27).

This second method is a null metrology measurement because it directly measures the shape error from ideal. In contrast, the laser Hartmann metrology system measures the absolute slope of the surface, therefore it is a non-null metrology measurement. Together these measurement methods play complementary rolls that determine the surface shape of a heliostat. The zoom Hartmann metrology system could measure the low frequency shape errors of heliostats at night with good fidelity, and the Solar wavefront metrology system could measure the mid

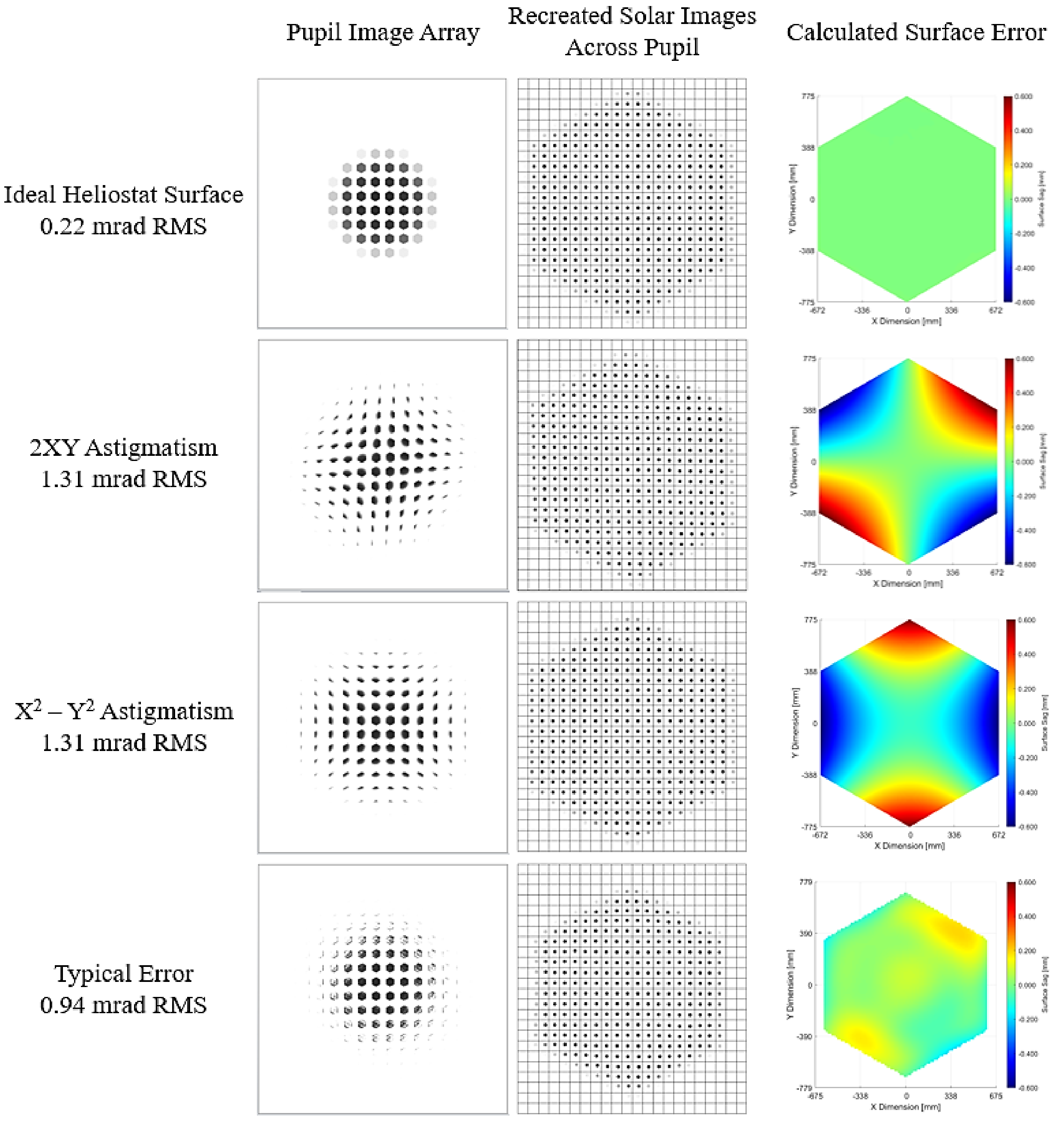

*Figure 4.27: Simulated measurements using Solar wavefront metrology. The top row is for an ideally shaped heliostat, second row for a heliostat with oblique astigmatism, third row for a heliostat with vertical astigmatism, and the fourth row for one of the heliostat surfaces measured in the laser Hartmann measurement. The minimum measurement error is about 0.2 mrad RMS, enough for heliostat metrology.*

frequency shape errors while a solar plant was in operation. Also, the Solar wavefront metrology system could be implemented using the Moon or the stars, though some modifications to the system shown above would be required. Starlight would require a larger number of lenses to obtain the necessary resolution.

## 4.9 Future Application

The potential for the prototype presented in this chapter to move power towers forward towards green hydrogen and biofuel generation is very promising. For all angles of incidence for the prototype experiment, ~6X geometric concentration was obtained. Scaling up this heliostat to a larger size would preserve the geometric concentration while increasing the total collected energy.

Heliostat mirrors that are readily available have a maximum width of 2 meters. Scaling up this prototype heliostat to have a width that is a multiple of this maximum width of 2 meters is thus a logical choice. A size that would push the limits of this design while remaining feasible is a 6 meter flat to flat regular hexagonal heliostat (see Figure 4.28).

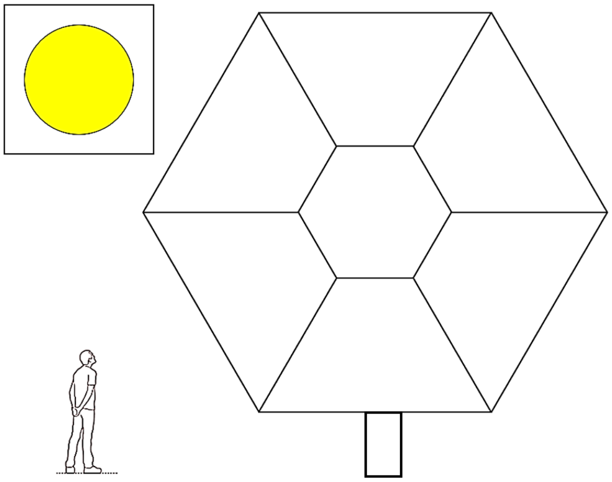

*Figure 4.28: Scaled up version of prototype heliostat that would use 2 meter width readily available heliostat mirrors cut into 6 trapezoids and 1 hexagon. The collecting area is 31 m$^2$.*

At this size the heliostat has a collecting area of 31 m$^2$. The scaling factor is 4.44, meaning the furthest distance for this heliostat to focus would be 180 m rather than 40 m, and the receiver would be 2.2 m square. The geometric concentration is then still 6X. Arranging hundreds of these heliostats into a power tower field makes it possible to obtain very high concentrations. In order to minimize cosine factor effects as well as the maximum sag change required to obtain the correct toroidal surface for each heliostat, heliostats are arranged North of the receiver within +/- 45° of North (see Figure 4.29).

In the proposed power tower field, heliostats are distributed within 50 meters to 180 meters of the power tower. Due to the lower RMS surface slope errors required for heliostats closer than 180 m, it is reasonable to state that all the light from closer heliostats will fall within the 2.2 m square receiver area. Therefore, each heliostat will be operating at ~6X concentration. In order to minimize blocking and shadowing, the ratio of heliostat area to land area is under one third.

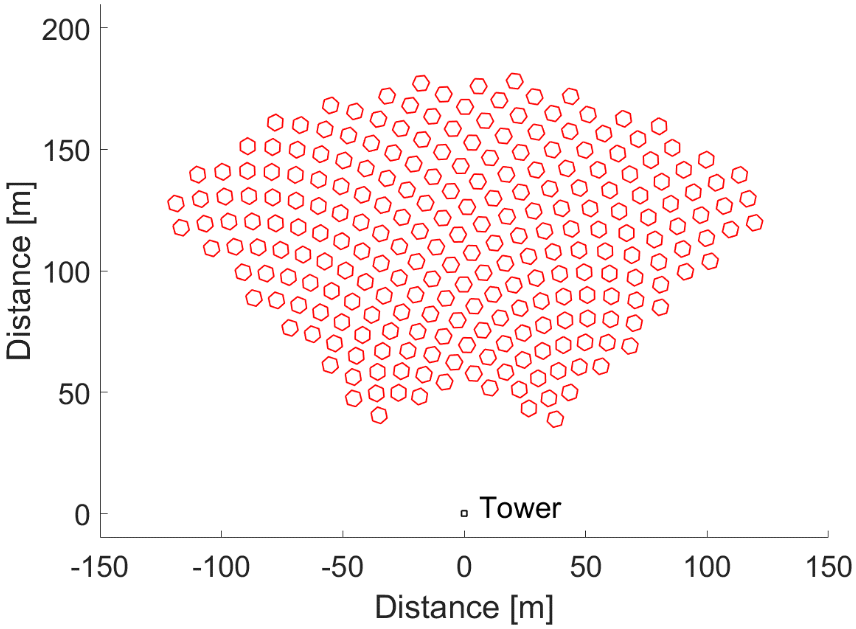

*Figure 4.29: Biomimetic power tower distribution using 243 actively deformable focusing heliostats with 31m$^2$ collecting area each. Each heliostat operates at ~6X concentration, thus the field operates at ~1,500X geometric concentration. This equates to 7500 m$^2$ of collecting area, or a 7.5 MW power tower.*

This particular arrangement follows a biomimetic pattern, which naturally reduces blocking and shadowing. The total number of heliostats is 243, meaning the geometric concentration of this proposed power tower is ~1,500X. The total collecting area is 7500 m$^2$, making this is a 7.5 MW power tower. In this particular arrangement, 95% reflective heliostats and an average cosine factor of 0.84 (i.e. 30° angle of incidence) makes it possible to achieve 1,200X solar concentration and the associated 1,500 °C, which enables the production of green hydrogen.

## 4.10 Conclusion

Actively focusing heliostats have the potential to achieve high solar concentrations using in the hundreds or thousands of heliostats. This high concentration can be achieved throughout the day by actively changing the heliostat shape in three different modes: curvature, oblique astigmatism, and vertical astigmatism.

The metrology required for measuring the surface shape of such heliostats is beyond the modern state of the art in terms of in situ measurement fidelity and/or speed. Two metrology systems were herein presented, one of which was made and implemented for the measurement of a 1.58 $m^2$ hexagonal heliostat with active shape change capabilities. This first method involved the use of a laser array, which was imaged onto a distant heliostat. Laser beams were reflected from the heliostat to a retroreflective screen, and a scientific camera measured the laser spot location. After a series of calculations, a slope map and a surface shape were generated. The calculated surface errors were fixed by actuation of the heliostat.

A laser Hartmann metrology system performs non-null slope measurements and can be used in situ on an entire power tower plant so long as a zoom lens is used to image the laser array, and a camera is located close to each heliostat being measured. Additionally, the measurement screen needs to be sufficiently large to receive reflected spots from each heliostat mirror, perhaps twice as big as the heliostats in use.

A second metrology system was proposed that involves placing a wavefront sensor at the focus of a heliostat (i.e. in situ). This Solar wavefront sensor performs null slope measurements of a heliostat surface. A series of pupil images are formed by a lens array, the pupil images being dissected together to form a collection of solar images. The relative overlap of each solar image is determined, and a slope error map is directly calculated. Integration of the slopes provides the surface sag error.

Together these metrology systems play complementary roles that make it possible to obtain the fantastic shapes necessary to focus sunlight from on-axis to greater than 70° angle of incidence. A measurement using the laser Hartmann method takes <15 seconds to obtain surface shape errors, though the physical measurement takes ~1 second. A measurement using the Solar wavefront method takes a similar amount of time, though the physical measurement is only the exposure time of one image (1/100th of a second perhaps).

The true limitation for a focusing heliostat is how well the surface shape can be corrected by active bending. This shape correction need only be to ~1 mrad RMS slope error, which was obtained for the 1.58 $m^2$ hexagonal heliostat. Future developments may involve creating a larger heliostat, thus allowing for fewer heliostats in a power tower field while still obtaining a high solar concentration of 1,200X. One additional benefit to larger and fewer heliostats is the reduced time to measure all the heliostat mirror surfaces in a field, allowing for more time spent generating hydrogen fuel.

# CHAPTER 5 : NULL METROLOGY DESIGN

## 5.1 Introduction

This chapter addresses four different types of null metrology techniques in some detail. Null metrology was briefly discussed in Chapter 1 and has been used wherever applicable in other chapters. Null type measurements are so powerful because they are directly measuring the error of an optical component from the ideal. The optical fabricator does not care so much what the shape of an optic is, but instead the optic error from the ideal. Thus, a null measurement is exactly what is desired.

Null measurements are often obtained using interferometry or wavefront sensing, though a "virtual" null measurement is possible for deflectometry [43]. For interferometry a single wavelength light source is generally used with a long coherence length. Thus, wavefront errors imparted by an optic are compared to an ideal wavefront, which generally has traversed a shorter distance. For wavefront sensing, a guide star is used to directly measure the wavefront errors imparted by the atmosphere or even system errors in the telescope. This is generally accomplished with a Shack-Hartmann wavefront sensor a pyramid wavefront sensor. A pyramid wavefront sensor is of some special interest because of its similarity to the Solar wavefront sensor of section 4.8.

Each of the measurement techniques herein discussed rely on either interferometry or wavefront sensing, except for the last topic. The last topic introduces a technique similar in applicability to the virtual null deflectometry, but it is a true null test that does not require interchanging components for free form surface measurements (i.e. what is needed for aspheric measurements for interferometry). This measurement device is dubbed the Chromatic Local Curvature (CLC) sensor. It builds on the heritage of the Chromatic Confocal Sensor, which will be discussed as an introduction to the CLC.

## 5.2 Pyramid Wavefront Sensor

In Chapter 4 two different metrology systems were discussed, one of which could perform null measurements. The null type test involved the use of the Sun to perform wavefront sensing. By examining the solar image formed by each part of the pupil, the local slope error across a heliostat mirror could be determined, and active correction of the mirror with at least three linear actuators would modify the mirror shape towards the ideal. An interesting and comparable measurement is found in pyramid wavefront sensors. By looking at a pyramid wavefront sensor the Solar wavefront sensor perhaps makes more sense in how it works.

Starlight can be heavily aberrated as it transmits through the atmosphere. Large aperture telescopes are unable to obtain diffraction limited imaging due to ~1 arcsecond blurring by the atmosphere. However, for small fields of view, diffraction limited imaging can be obtained if adaptive optics are used. A deformable mirror compensates atmospheric wavefront errors. At a separate plane conjugated to the deformable mirror, a Shack Hartmann wavefront sensor is placed, which forms an array of star images. According to the displacement of the star images, local slope errors can be measured, and the wavefront error calculated by slope integration so that the shape change of the deformable mirror can be determined.

An alternative to a Shack Hartmann sensor is a pyramid wavefront sensor. Interestingly, the tip of the pyramid for a pyramid wavefront sensor is placed at the star image. The image of the guide star is well centered and generally close to diffraction limited in a closed loop adaptive optics system. The pyramid wavefront sensor then splits the star image into four parts, either by reflection or transmission. Four pupil images are then formed on four separate sensors (see Figure 5.1). Ideally the light from each section of the pupil will be equally divided among the four pupil images.

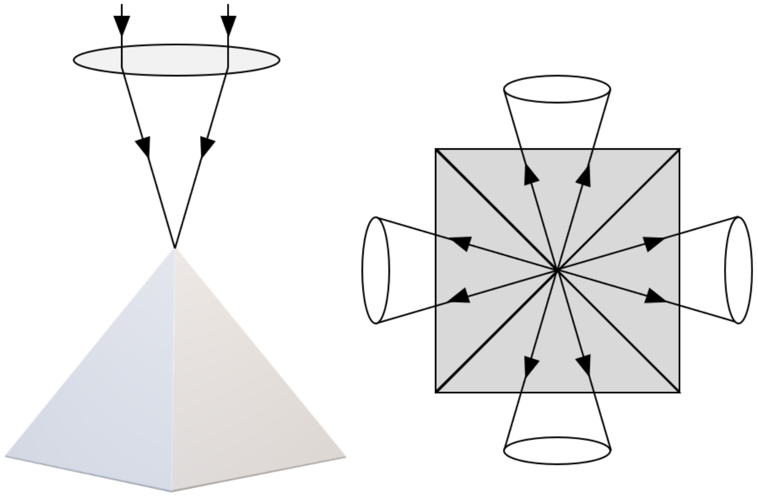

*Figure 5.1: Pyramid wavefront sensor. Light is focused on the pinnacle of the pyramid (left) and split into four parts with each part forming a pupil image (right).*

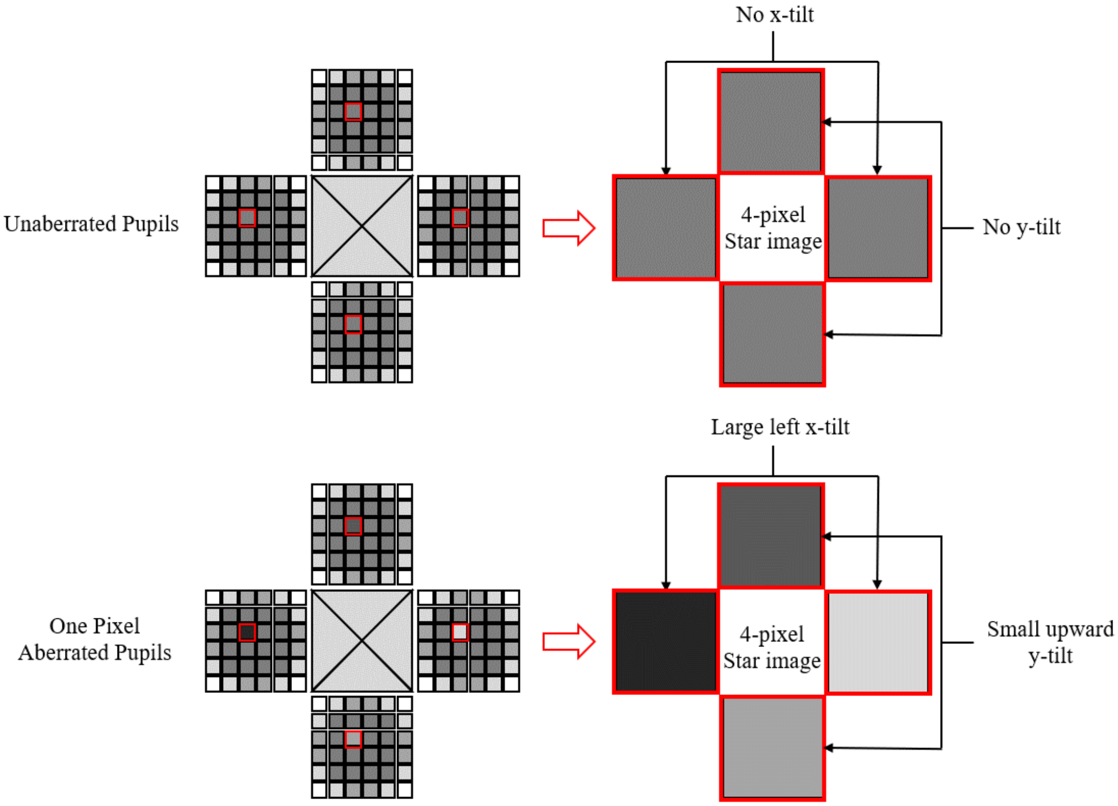

*Figure 5.2: Two examples of pupil images formed by a pyramid wavefront sensor. In the top row, an ideal situation is shown where each pupil image is equally bright. Looking at the same pixel from each pupil image shows there is no x-tilt or y-tilt in the 4-pixel star image. In the bottom row, one area of the wavefront has been aberrated and one-pixel position shows a deviated star image.*

Generally, fluctuations from the atmosphere will cause the light to be offset relative to the pinnacle of the pyramid. A global tilt will cause the entire star image to shift and perhaps two of the pupil images will be brighter, and two will be dimmer. A centroiding calculation would show that the star image had shifted, and a tilt in the deformable mirror would readily correct the measured global tilt. Local tilts across the aperture cause the correlated pixel to appear oppositely bright and dark in the pupil images (see Figure 5.2). Calculating the "centroid" of the star imaged formed by each pupil position (i.e. pixel position) allows for calculation of slope errors across the pupil. These errors can be corrected by locally changing the deformable mirror.

Thus, a Solar wavefront sensor and a pyramid wavefront sensor are used to measure surface slope errors in a similar manner. A Solar wavefront sensor is a generalization of a pyramid wavefront sensor. For the Solar wavefront sensor, the "star image" of the Sun is much larger and not diffraction limited, therefore the light should not be divided by a pyramid. Instead, a large fly's eye array can be placed at the focus with each lenslet forming a pupil image.

## 5.3 Sub-Aperture Fizeau

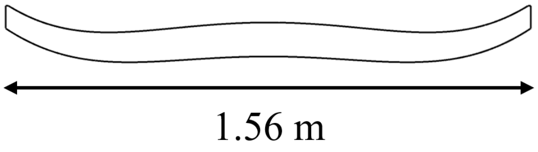

*Figure 5.3: Gull wing lens for a 6.5 m spectroscopic telescope with a 3° FOV.*

In the paper, "6.5 m telescope for multi-object spectroscopy over a 3° field of view" by Eads and Angel, published by Applied Optics, a large 1.56 m diameter gull wing lens is part of the design (see Figure 5.3) [44]. During the telescope design process, the shape of the lenses tended towards a gull wing. This is because the design was optimized for a large field of view and a highly constrained geometry. Cell phone cameras have similar requirements imposed upon them, which is why gull wing lenses are standard. The power of a gull wing lens to push a telescope to achieve design requirements, especially for large fields of view and constraining geometries (e.g. the size of lenses), is very impressive. These types of lenses should continue to be investigated to enable the improvement of future telescopes. This telescope design is discussed in greater detail in Chapter 6. In this section, metrology for the gull wing lens required for the design is discussed.

Proposed metrology for this lens involved the implementation of two techniques: a sub-aperture Fizeau test and a full aperture transmission test. Both techniques would require the use of computer-generated holograms (CGH). In this first section is a detailed description for how a sub-aperture Fizeau test could be performed.

A Fizeau interferometer can be one of the simplest interferometers. Its functionality is readily explained by two pieces of glass with wedge. Light passing through the top piece of glass is reflected from the bottom surface, and light that passes through the top piece of glass reflects from the top surface of the bottom piece of glass. If light with a reasonably long coherence length is used (i.e. mercury source or laser), then these two beams will interfere where the optical path difference (OPD) between the beams is directly related to the thickness of the gap between the pieces of glass (see Figure 5.4). The equation for the OPD is

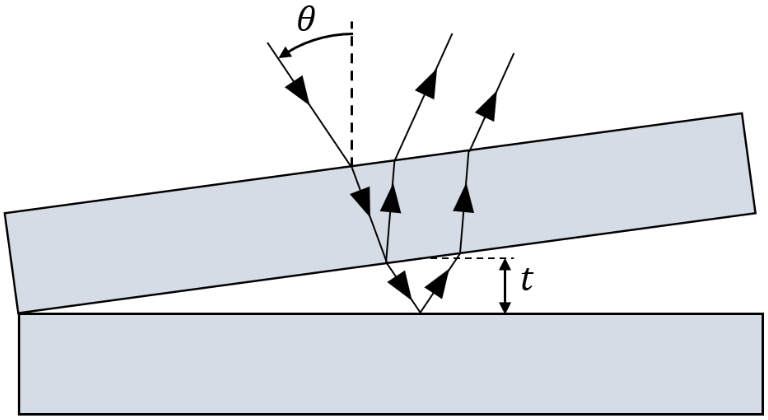

*Figure 5.4: Basic Fizeau interferometer. Two beams are interfered, one reflecting from the bottom surface of the top slab of glass and the other reflecting from the top surface of the bottom slab of glass. The initial beam comes in at some angle $\theta$ and the gap between the glass slabs has variable thickness t.*

$$OPD = \frac{2nt\cos\theta}{\lambda}, \tag*{Eq. 5-1}$$

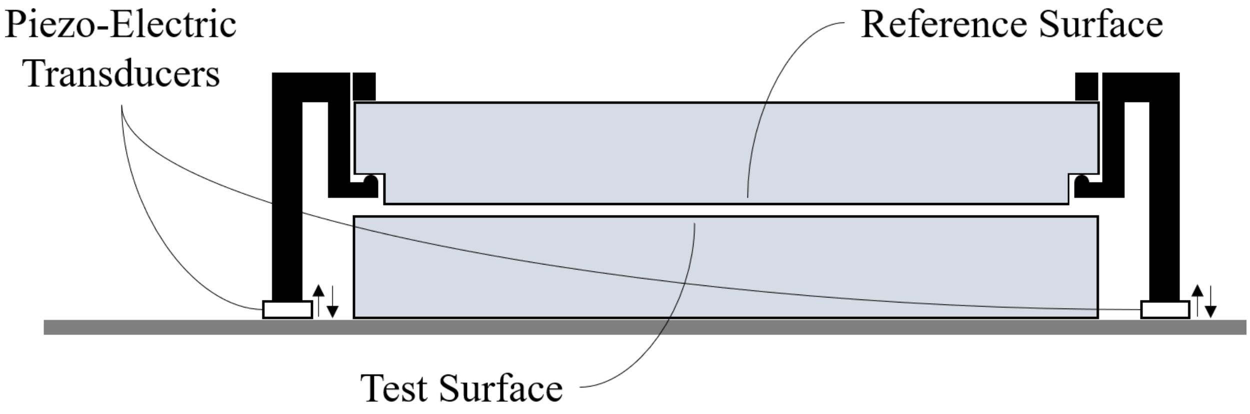

*Figure 5.5: A schematic for mounting a reference plate above a test plate. The reference surface can move very close to the test surface and fine adjustments via piezo-electric transducers makes phase-shifting possible.*

where $n$ is the index of refraction between the glass slabs (usually 1 for air), $t$ is the local separation of the glass slabs, $\theta$ is the incoming angle of the light, and $\lambda$ is the wavelength. The light reflected from the top slab would perhaps be the reference beam and the light reflected from the bottom slab would be the test beam.

The basic Fizeau interferometer is generally more qualitative in measurements due to the lack of phase shifting. However, phase shifting of a basic Fizeau interferometer can be made possible by mounting the reference glass in an adjustable height mechanism. This mount could either be standing or attached to a commercial interferometer (see Figure 5.5). Piezo-electric transducers, which can move with steps less than 30 nm, would be suitable for phase shifting [45]. Phase-shifting interferometry generally requires surface motions of λ/8, or 79 mm.

Returning to the gull-wing lens, if a very small reference plate were able to be precisely moved to different positions above the lens, then interferomertic measurements could be taken to obtain a full 3D surface map. Over a small region, the gull-wing lens is approximately flat, thus a basic Fizeau interferometer is created.

If a larger reference plate were used, there would be a toroidal departure of the test surface from the reference surface. The test would no longer be null, though perhaps the surface shape would still be measureable. If the reference plate were increased in size, eventually the departure from flat would be significant enough that fringe spacing would be of a higher frequency than the Nyquist frequency of the detector. Phase-unwrapping algorithms would no longer be correct, and a false measurement would be made. In the case of the gull-wing lens, interferometric measurements in this fashion would take a significant amount of time.

This process could be significantly faster if instead of having a reference flat, a best fit reference toroid were used. A CGH could even be written on the reference surface to correct for residual aberrations, making the test truly null. This method was suggested in the previously mentioned paper by Eads and Angel. However, a way to perform phase-shifting was not addressed. A real experiment may consist of a toroidal reference surface suspended above the gull wing lens. Piezoelectric stepper motors would be used for phase shifting, and an extended mercury lamp would be used as a source. This would ensure that fringes were visible across the surface.

Great care would need to be taken to ensure the toroidal reference surface did not scratch the gullwing lens. The reference optic would perhaps need to be removed from the gullwing lens each time the gullwing lens was rotated for a different subsection measurement. In this

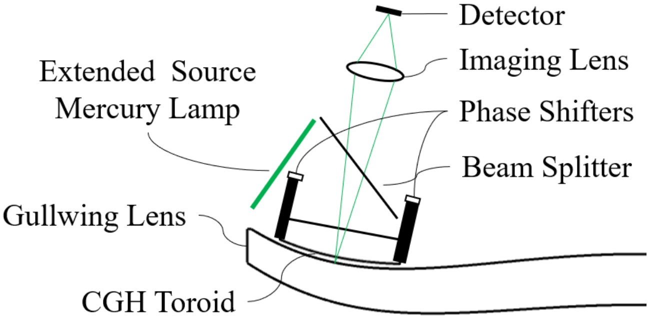

*Figure 5.6: Schematic of interferometric measurement of a large gullwing lens. A toroidal reference surface is suspended above the gullwing lens. Phase shifting is induced by piezoelectric transducers. An extended source mercury lamp is used so that fringes are visible across the aperture of the reference surface. An annular ring would be measured by rotating the gullwing lens, and stitching measurements together.*

manner a series of annular rings would be stitched together to form a full surface map. A schematic view of this system is shown in Figure 5.6. Eight 100 mm square toroidal plates would need to be made to measure the full clear aperture of this optic [44].

## 5.4 Full Aperture Gullwing

After one surface of the double gullwing lens was made to the desired precision and measured using the sub-aperture Fizeau tests, the other surface could be tested in a similar manner. However, grinding and polishing the other surface using perhaps swing-arm metrology would allow the said surface to be within a few microns of the ideal shape. Then, a full aperture transmission test could be used instead of the sub-aperture Fizeau test. This would make the final polishing steps quick and would ensure the two surfaces were well aligned. Note, a transmission test appears possible due to the low-power appearance of the gull-wing lens. The thickness appears nearly constant, thus light transmission through the lens may not significantly refract light beyond testing capabilities.

The setup for this experiment is shown in “6.5 m telescope for multi-object spectroscopy over a 3° field of view.” A point source from perhaps a Fizeau type interferometer is reflected by a beam splitter into the gullwing lens. Light transmits through the gullwing lens and reflects from a large spherical mirror. Light then transmits again through the gullwing lens, passes through the beam splitter, and a focusing lens. A CGH is then introduced to clean up residual wavefront errors before the light comes to a focus. In order to return the light to the interferometer, a high precision steel ball could be placed centered at the focus after the CGH. Light would then return through the system to the interferometer (see Figure 5.7).

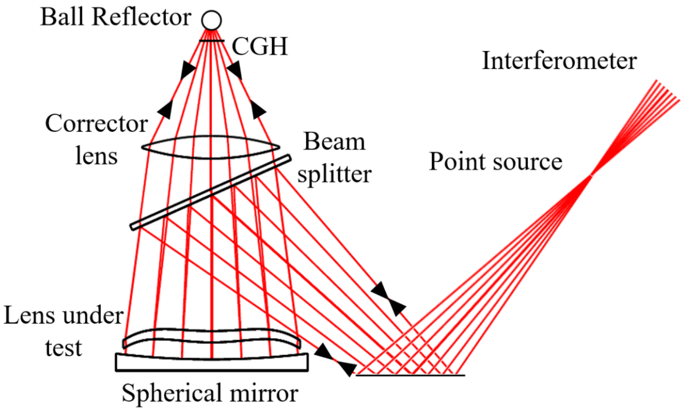

*Figure 5.7: A potential arrangement for a full aperture transmission test of a large gullwing lens. A beam splitter reflects light from an interferometer into the gullwing lens. A spherical mirror reflects the transmitted light, which returns through the gullwing lens and transmits through the beam splitter. The aberrations in the beam are significantly reduced by a corrector lens and then a final wavefront cleanup is performed by a CGH near the focus. A ball reflector is centered at the focus so that light will return to the interferometer, thus making a second double pass on the gullwing lens.*

This optical design reduces the wavefront error to be corrected by a CGH to 240 waves, well within the capabilities of a CGH. The issue with this experiment is that the beam splitter, spherical mirror, and the corrector lens need to be made with high precision so that only the error in the gullwing lens is measured. However, this cost may be comparable or less than the cost of making 8 toroidal test plates, each with a CGH imprinted upon the toroidal surface. Also, it is important to consider that the time to take a measurement is significantly reduced by a full aperture test.

Methods for measuring large gullwing lenses push state of the art metrology and manufacturing techniques to the limit. It is certainly feasible that this gullwing lens could be manufactured within the desired specifications, though the cost may be significant. Future developments in metrology may make such lenses much cheaper to measure.

## 5.5 Confocal Chromatic Sensor

Another metrology technique of interest is found in the confocal chromatic sensor (CCS). The CCS uses chromatic aberration (chromatic change in focus) to perform high precision surface measurements with a large dynamic range. These devices are commercially available and have been useful in measuring highly aspheric surfaces as well as surfaces with steep height changes (step surfaces). Current methods involve laterally moving surfaces underneath the sensor at a known speed, or perhaps rotating a lens element while laterally shifting the CCS, creating a spiral measurement of the surface. The result is usually a low spatial sampling, but high accuracy height measurement (<1µm precision).

It is relevant to understand the working principles of a CCS. A CCS uses chromatic change in focus to create a continuous range of focal planes. Placing a reflective surface at one of these focal planes will cause only the wavelength that focuses at the reflective surface to return through the CCS with a high signal. A spectrometer then analyzes the returned beam to see which color returned (see Figure 5.8). Based on the callibration of the sensor, a given color is associated with a certain distance from the sensor.

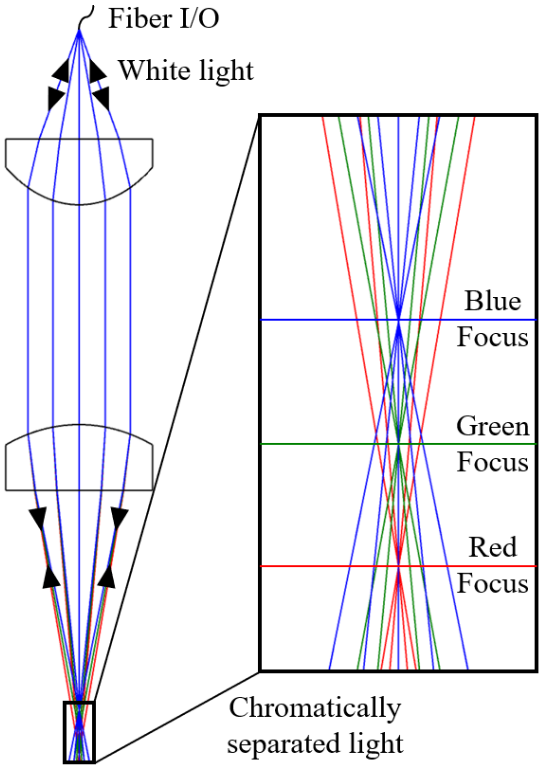

*Figure 5.8: A simple schematic of a chromatic confocal sensor. White light is collimated and then focused by a chromatically aberrated lens. Different colors of light focus in different focal planes. A reflective surface in a given focal plane will cause the associated color to return through the sensor with high signal while other colors diverge and return with low signal.*

A modern commercial CCS is in a "cateye" configuration, a common configuration for both interferometers and point source microscopes. In this configuration, light is focused on the surface. A different, but also very common, configuration is the confocal configuration, where a surface is placed concentric about a focus. Both interferometers and point source microscopes are commonly used in the confocal position, but confocal chromatic sensors are not. Thus, a potential modification to the use of a CCS is to measure a surface in a confocal configuration  (see Figure

5.9). This slight modification to a CCS lays the groundwork for the chromatic local curvature sensor (CLCS).

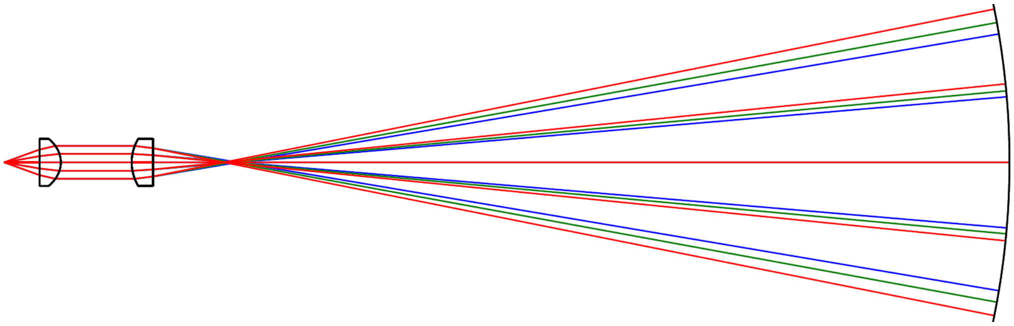

*Figure 5.9: Confocal configuration with a chromatic confocal sensor.*

## 5.6 Chromatic Local Curvature Sensor

Using the CCS in a confocal configuration without further modifications will result in the color of light that focuses at a point concentric with the surface under test returning through the CCS to the spectrometer with high signal (i.e. if the surface is concentric with the green focus, then green light will be measured). A confocal configuration then has little difference from a cateye configuration, so long as the surface being measured is spherical. However, no mirror is perfectly spherical though. What this means is that the spectrometer won’t just read a single color with high signal. Rather a spectrometer will read a small range of colors where the peak color (wavelength) is associated with the best fit sphere (see Figure 5.10). While

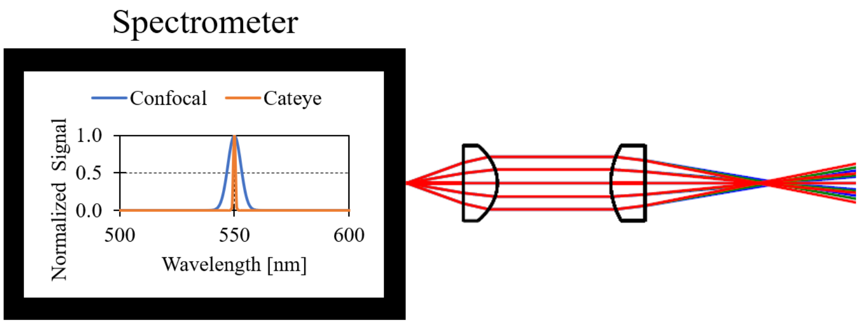

*Figure 5.10: Two representative signals from different measurements. The cateye configuration yields a sharp peak at 550 nm. The confocal configuration also peaks at 550 nm, but due to irregularities in the spherical surface the signal will be broadened slightly.*

knowing the best fit sphere of a surface is useful and important, manufacturers may be more interested in how spherical a surface is. They want to know what the error from a sphere is. Thus, more significant modifications are required to make this system work.

A Zemax model was created for a multiple exposure method (see Figure 5.11). Light from a monochrometer (or spectrally filtered white light) enters the system from the left. The white light is spectrally filtered, and then passes through a 50/50 beam splitter. A chromatic lens focuses each of the wavelengths at a different focal plane. Light then propagates to the optic being measured (perhaps an aspheric surface), reflects, and returns to the chromatic lens. The beam splitter then sends the light to an achromatic lens, which focuses the light onto a pinhole. Wavelengths that

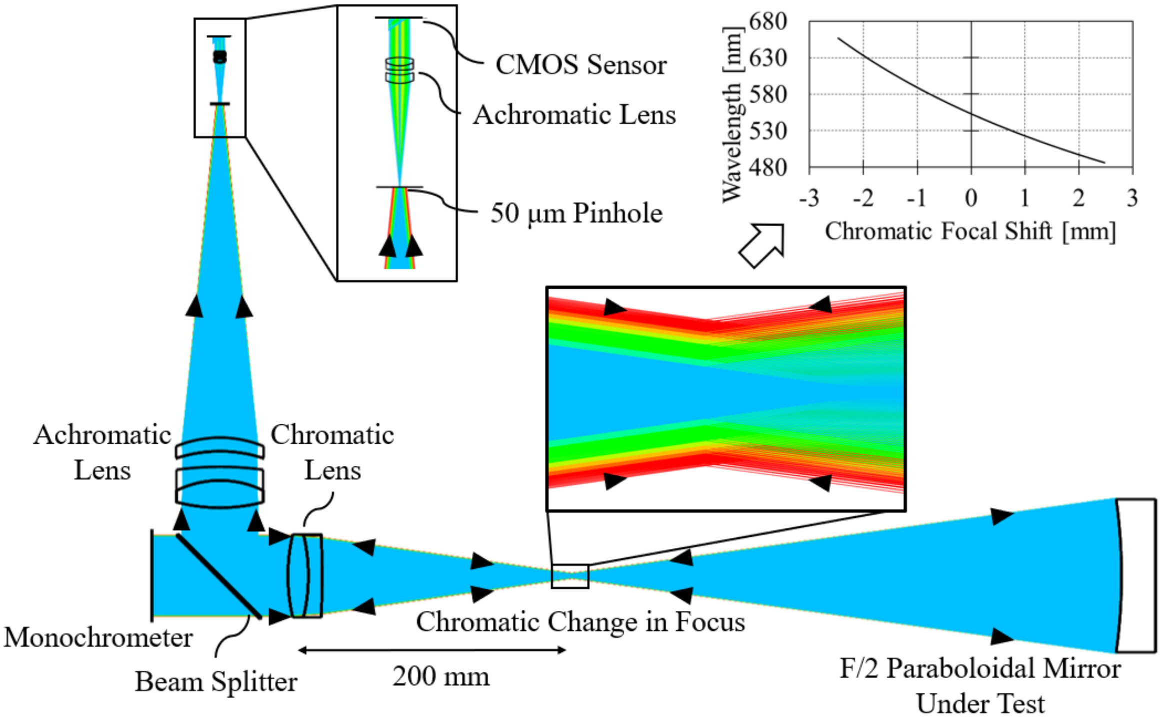

*Figure 5.11: A chromatic local curvature sensor. Spectrally filtered light is focused by a chromatic lens, reflects from an aspheric surface, passes through the chromatic lens again, reflects from a beam splitter, focuses by an achromatic lens, is spatially filtered by a pinhole, is collimated by another achromatic lens imaging the pupil onto a CMOS sensor where a series of time separated pupil images are formed. The chromatic focal shift allows for local curvatures to be measured with peak to valley changes in distance from the center of curvature of +/- 2.5 mm.*

were not confocal at the various locations across the pupil are significantly filtered by the pinhole. The spatially filtered beam then propagates to another achromatic lens, which collimates the light and forms a pupil image on a CMOS sensor.

In the Zemax model, the chromatic lens is a 2” diameter F/4 lens with diffraction limited performance at each individual visible wavelength. The chromatic change in focus is +/- 2.5 mm centered near 550 nm wavelength. An F/2 paraboloidal mirror 112 mm in diameter is tested, which has an aspheric departure from the base radius of 0.02 mm. The achromatic lens is similarly F/4, but diffraction limited for the full visible spectrum. The pinhole size chosen was 50 μm. This is large enough to ensure diffraction from the edges of the pinhole do not affect the measurement, but small enough to ensure that non-confocal light is filtered out. A scaled down version of the first achromatic lens is used to then collimate the light, which is then incident upon the CMOS sensor (multiple wavelengths are shown simultaneously in Figure 5.12). Note, an achromatic lens may not be the best candidate for forming pupil images since imaging is occurring through the chromatic lens. Thus, an alternative chromatically aberrated lens is necessary so that all the pupil images are in focus at the same plane.

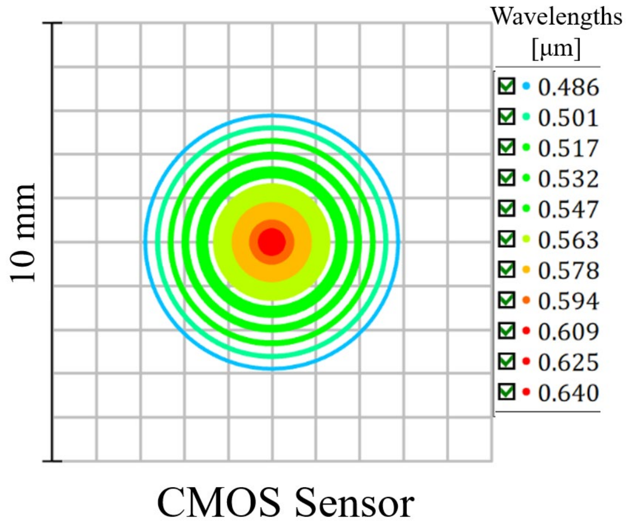

*Figure 5.12: Spot diagrams on the CMOS sensor. The separate wavelengths are compiled from separate exposures, clearly visible in annular rings.*

A single-shot method is also a possibility for the CLCS, however this requires the use of a diffraction grating and designating specific regions of a CMOS sensor to be associated with a specific wavelength range. Spectral blurring would need to be carefully considered. Yet, with a single-shot method, measurements could be obtained more quickly. Variations due to air motion or shape change in a deformable mirror could potentially be measured.

For the multiple exposure approach, if the CMOS sensor ran at 100 FPS then 100 wavelength bands could be measured each second. In interferometry, extra time can cause vibrations to corrupt the phase measurement of a surface, which is why single-shot measurements are so powerful. For the CLCS, there is no phase measurement, no phase unwrapping, etc. Therefore, actively changing surfaces may not be measurable, but there does not appear to be the same negativities for the CLCS as for interferometry by taking multiple exposures for a surface measurement.

There is one subtlety to this measurement that should be explored to gain a better appreciation for the complexity of this sensor. Aligning the optic under test to the CLCS may prove to be very challenging because of the implementation of a pinhole at the focus of a lens. A small tilt in the test mirror of 0.2° will walk the beam completely off a 50 µm pinhole. Thus, either the position of the pinhole should be variable, or the test mirror needs to be aligned with high precision (~0.001°). If the pinhole position is variable, the spot position should be measurable. Thus, a custom beam splitter, similar to a Shack cube [46], should be implemented, except each surface should have curvature such that the confocal white light is not dispersed. In this manner a CMOS sensor

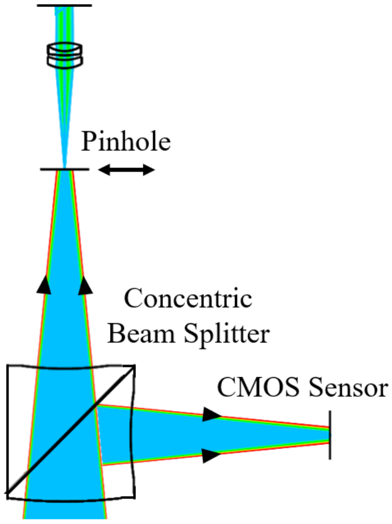

*Figure 5.13: Concentric beam splitter introduced into beam path so a CMOS sensor can be used to centroid the spot. Then the pinhole position can be automatically adjusted to assist in alignment.*

could be placed in the separate light path to get the centroid of the focus, and the pinhole position could be automatically adjusted for correct alignment (see Figure 5.13).

The CLCS has a great potential to open the doors to rapid precision freeform optics metrology. Like deflectometry, there is no need for implementing special optics for different aspheric surfaces. Whether the optic under test is axially symmetric, off-axis, near spherical, or highly aspheric, a chromatic local curvature sensor may be the universal metrology instrument required to make these optics of the future possible. And if an optic is measurable, then the door for manufacturing is opened.

## 5.7 Conclusion

This chapter has been a brief discussion of various null metrology techniques used for a variety of optical components. Understanding the pyramid wavefront sensor helps in better understanding the Solar wavefront sensor of Chapter 4. The Fizeau sub-aperture test revealed how highly aspheric surfaces can be measured using basic interferometry techniques. Additionally, a transmission test for a gullwing lens was discussed to show it is possible to measure such an optic without sub-aperture stitching. Note, this is relevant to the mobile phone industry where gullwing lenses are a staple. Current metrology methods involve sub-aperture stitching techniques, thus not every lens is measured. A rapid full aperture test would make it possible to measure every lens, and thus obtain even tighter tolerances. Tighter tolerances that will be necessary as cellphone manufactures push towards better cameras.

A modern metrology system, the confocal chromatic sensor (CCS), was introduced as a primer for a new concept metrology system, the chromatic local curvature sensor (CLCS). The CLCS makes it possible to perform full aperture tests of aspheric elements. The conceptual system shown in this chapter can measure an F/2 paraboloidal mirror without null optics. Highly aspheric surfaces can be measured if the chromatic change in focus becomes larger. Though each wavelength should still obtain a diffraction limited spot, which is challenging with a large chromatic change in focus. Further developments of the CLCS could lead to rapid high precision metrology of freeform surfaces, even freeform surfaces with significant peak to valley variations in shape.

# CHAPTER 6 : TELESCOPE OPTICAL DESIGNS

## 6.1 Introduction

This chapter is different from any of the previous chapters in that it is a compilation of optical designs for telescopes with different applications in mind. Several of the designs build upon the heritage of other telescope designs and modern telescopes that have been constructed. The design goals of many of the telescopes were based on improvement over previous telescopes with the limitation often being the ability to optimize within a specific imaging criterion for a larger field of view. Two of the designs presented have previously been published in papers, where detailed analyses including some tolerancing, and deeper discussion of scientific applications. The focus of this presentation is the nominal optical performance of the designs; thus, these designs do not fully represent a manufacturable telescope. A full tolerance analysis of each design would still be required, among other things, like mechanical design. Additionally, a new class of telescopes is introduced, the double Cassegrain, of which the four mirror 20-m telescope is a variant.

## 6.2 Ground Based Wide-field 6.5 m Spectroscopic Telescope

In the previously mentioned paper, "6.5 m telescope for multi-object spectroscopy over a 3° field of view", a detailed description of such a telescope is provided. The design in this paper was inspired by a large 6.5 m F/1.25 primary mirror blank with a 1.3 m center hole, manufactured by the Mirror Lab. The use of this mirror had not been designated when it was initially casted, thus potential applications were explored. The goal for this design was to obtain a wide field, 3.0° field of view for multi-object spectroscopy. The ideal focal ratio for optimal fiber optic coupling efficiency is near F/3.7. Thus, the design was optimized for this focal ratio. In the published paper there are few details on the design process. Herein is a more detailed description of the requirements in the merit function, such as the size of the elements, locations of elements, and the field sampling necessary for high order aspheres. A unique 1.56 m gull-wing lens was required to make this design possible. Lenses of this nature and size have been previously manufactured and implemented into telescopes [47].

The most challenging aspect of the design was fitting the 3.0° F/3.7 focus through the 1.3 m center hole. The minimum size of the field occurs near the focus, which is 1.26 m in diameter. Also, no elements were allowed inside the primary center hole due to the greater seismic risks associated with such a geometry. Having a fast focus with geometric constraints, a wavelength range from 365 nm to 900 nm and a large 3° FOV made it essential for highly aspheric elements to be used.

These are constraints very similar in nature to what cell phone lens designers have enforced upon them. A cell phone has very demanding thickness constraints. Thus, the only solution to collecting more light for imaging is to make the lens with a very fast focal ratio to improve low light performance. Modern cellphones have been able to achieve focal ratios less than 2. Additionally, the first surface is usually the stop so that the maximum amount of light can be collected. Visible light needs to be imaged for a large field of view. Because of these constraints, and many others, cell phone lenses almost always have one or more highly aspheric gullwing lenses. Section 5.3 revealed that this telescope design requires a gullwing lens, just like cell phones. The main difference of course is the scale.

When highly aspheric elements are used, in optimization it is necessary to sample the field with a much greater density than when using spherical elements. In many cases, 3-5 field sampling points are plenty to ensure an optical design meets the imaging criteria across the FOV (for spherical surfaces). Not so when highly aspheric elements are used. A good rule of thumb is to have 3 field sampling points plus the number of higher order terms, otherwise different segments of the lenses can be optimized for solely one field of view and the intermediate fields are poorly optimized. In the spectroscopic telescope design, the aspheric elements went out to 14th order, thus there were 6 higher order terms (including conic constant). Using this rule of thumb, at least 9 sampling points were used, which ensured that the optical performance was well optimized across the FOV. Truthfully, this is just for preliminary optical design. The field performance at a higher density should be at least evaluated before a final design is settled upon.

Another constraint of the optical designs of this telescope was the size of the elements used. The largest lenses that can be created with high optical quality and a large bandwidth are composed of fused silica. The size of fused silica lenses is limited to about 2 m, however at that size the elements become quite heavy (one element of such size approaches 1 ton), and structural support becomes extra challenging. Thus, the lenses were kept to less than 1.6 m in diameter, perhaps half the weight of a 2 m lens. This requirement of smaller apertures caused the lenses to be clustered close to the large 1.2 m diameter focus, which drove the optical design space towards a limited geometry region. The lenses could not be too close to the 1.3 m center hole.

Another significant optical design challenge was in the correction for atmospheric dispersion. Due to the large size of the elements being used, and the large bandwidth desired, traditional rotating prisms were not considered. Additionally, the counterrotating wedged elements such as are used in DESI, limited the optical design space. No, the correction of atmospheric dispersion was accomplished by introduction of a prism into the system by lateral motion of spherical elements, as originally proposed by Saunders [48]. This increased the size of two of the elements, but they were still less than 1.6 m, as desired. The elements used were not both kept to a low power as is recommended. Thus, on-axis coma was introduced into the design. To compensate for this as well as astigmatism and tilt, the secondary mirror must be laterally displaced as well, though by much smaller increments.

In this manner, multiple configurations were optimized for elevation angles of 40°, 50°, 70°, and zenith pointing, each for a large 3° field of view over 365 nm to 900 nm. The chief ray angles were kept close to normal on a curved image plane so that manufacturing of fiber positions would only require the fibers to be normal to the curved surface, rather than at some oblique angles. The lenses were kept to less than 1.6 m in diameter and aspect ratios ≈20 or less. All lenses were kept at least ≈2” away from the primary mirror (i.e. none inside the central hole). With the merit function properly setup, and after several global searches, a design involving 5 lenses was chosen for further optimization. A Cassegrain design was chosen to keep the overall length of the

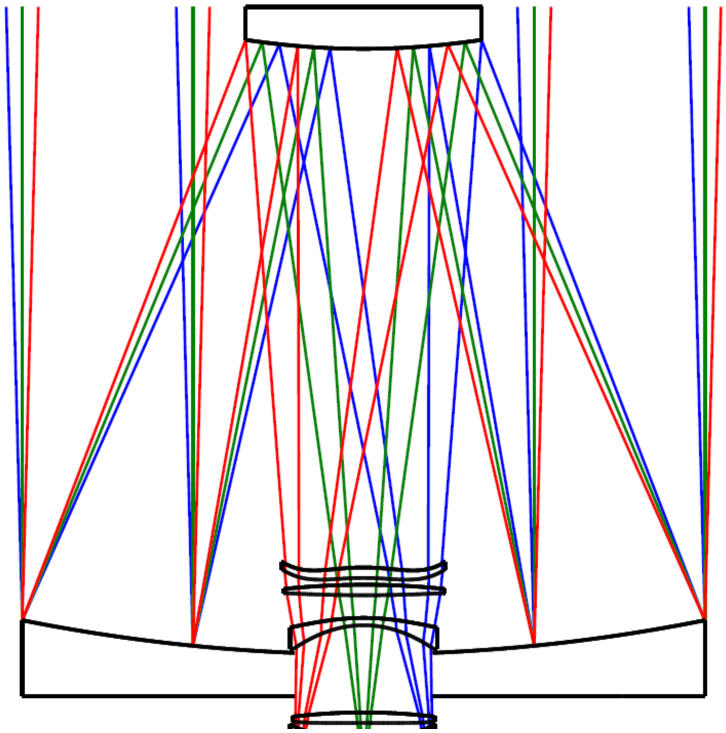

*Figure 6.1: 3D layout of the 3° 6.5-m spectroscopic telescope final design.*

telescope reasonable. Additionally, this would keep the tolerances somewhat loose compared to a three-mirror telescope. The final design settled on is shown in Figure 6.1.

The imaging performance across the field of view from zenith pointing down to 40° elevation is 80% of the polychromatic light within 1.2”, or 140 µm diameter. Since this design is not diffraction limited, geometric spot diagrams provide a good representation of optical performance, shown in Figure 6.2. Spots are shown only along the positive y direction from 0° to 1.5° for two configurations, zenith pointing and 40° elevation. Preliminary evaluations in Zemax showed that exposures could occur over periods of time near 15 minutes before atmospheric dispersion has changed enough where adjustments in the lateral motion of the correcting elements is required. Thus, changes in distortion by lateral motion of the correcting elements is not required during exposures. Note, the max distortion of this design is ~1%. Thus, distortion would need to be carefully calibrated. The prescription for this telescope is given in Table 6-1.

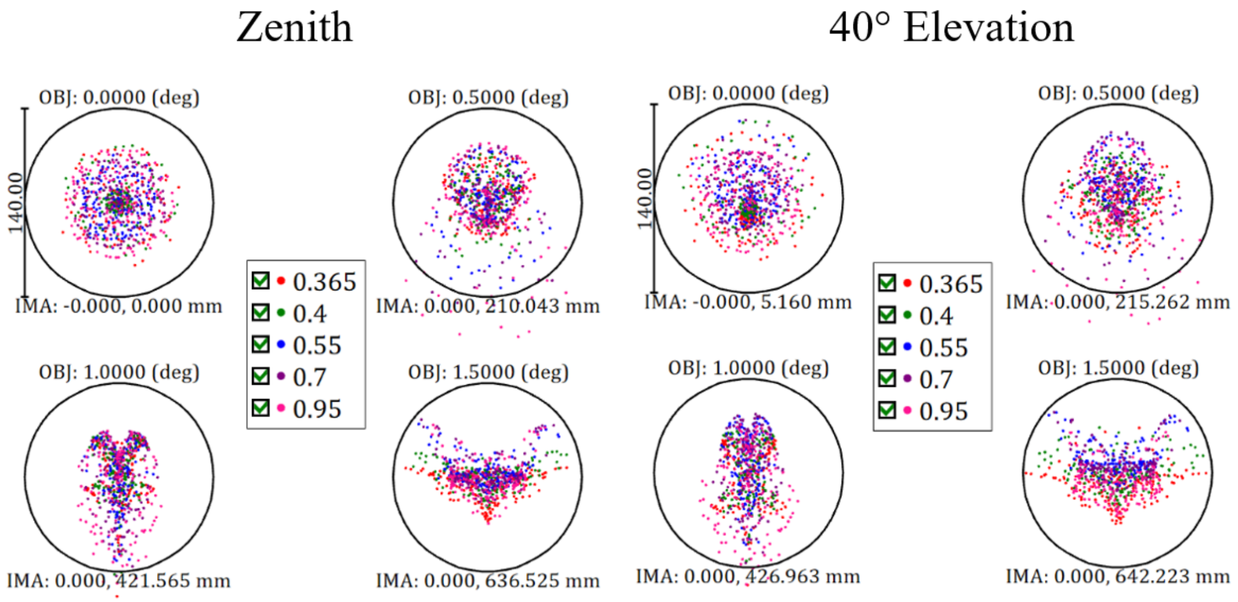

*Figure 6.2: Spot diagrams across the field of view for both zenith pointing and 40° elevation. Note, the polychromatic encircled energy is nearly 100% into the 140 µm (1.2 arcsecond) circles shown.*

*Table 6-1: Prescription for wide-field 6.5 m spectroscopic telescope when Zenith pointing. Lateral motions of surfaces 2, 5-6, and 11-12 are required for atmospheric dispersion correction.*

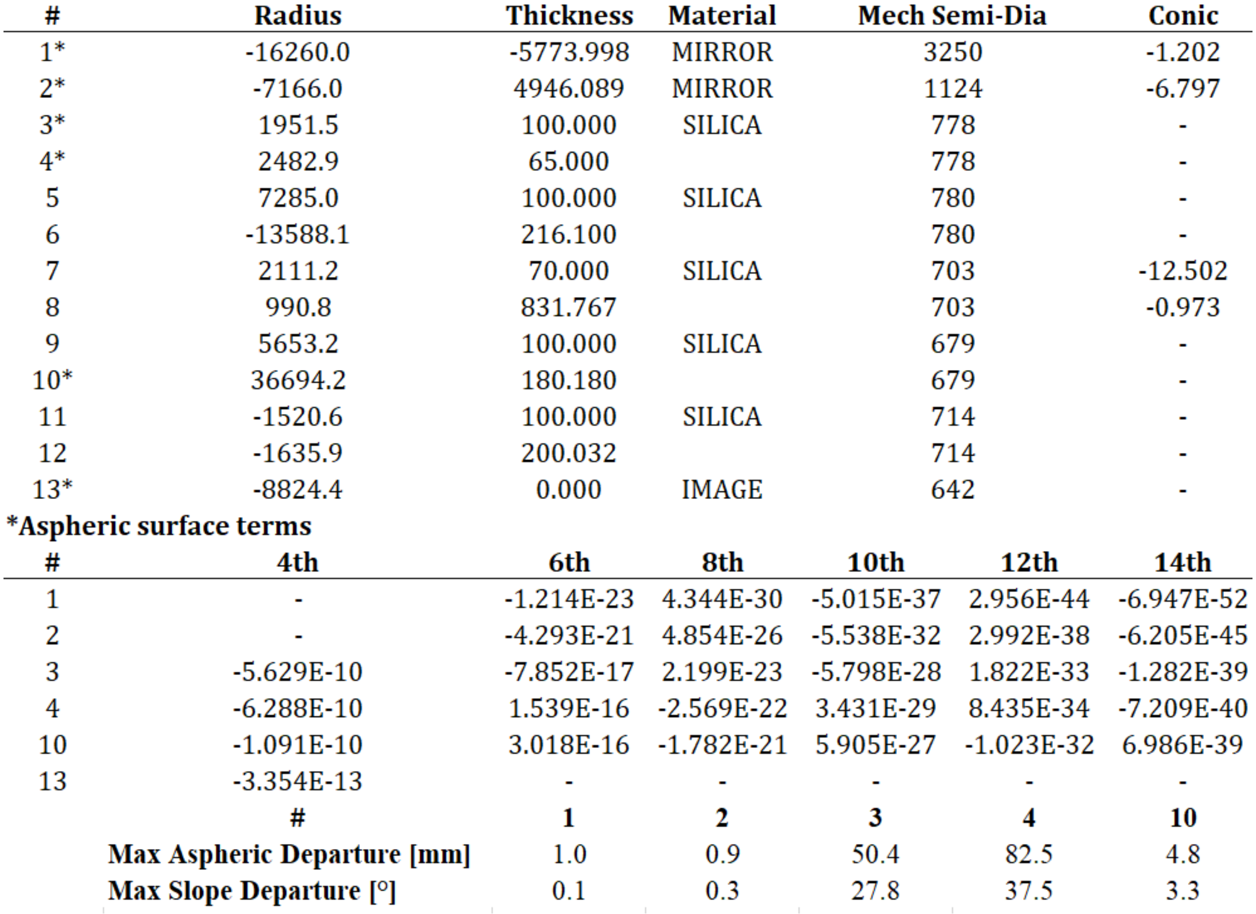

| # | Radius | Thickness | Material | Mech Semi-Dia | Conic |
|---|---|---|---|---|---|
| 1* | -16260.0 | -5773.998 | MIRROR | 3250 | -1.202 |
| 2* | -7166.0 | 4946.089 | MIRROR | 1124 | -6.797 |
| 3* | 1951.5 | 100.000 | SILICA | 778 | - |
| 4* | 2482.9 | 65.000 | | 778 | - |
| 5 | 7285.0 | 100.000 | SILICA | 780 | - |
| 6 | -13588.1 | 216.100 | | 780 | - |
| 7 | 2111.2 | 70.000 | SILICA | 703 | -12.502 |
| 8 | 990.8 | 831.767 | | 703 | -0.973 |
| 9 | 5653.2 | 100.000 | SILICA | 679 | - |
| 10* | 36694.2 | 180.180 | | 679 | - |
| 11 | -1520.6 | 100.000 | SILICA | 714 | - |
| 12 | -1635.9 | 200.032 | | 714 | - |
| 13* | -8824.4 | 0.000 | IMAGE | 642 | - |

***Aspheric surface terms**

| # | 4th | 6th | 8th | 10th | 12th | 14th |
|---|---|---|---|---|---|---|
| 1 | - | -1.214E-23 | 4.344E-30 | -5.015E-37 | 2.956E-44 | -6.947E-52 |
| 2 | - | -4.293E-21 | 4.854E-26 | -5.538E-32 | 2.992E-38 | -6.205E-45 |
| 3 | -5.629E-10 | -7.852E-17 | 2.199E-23 | -5.798E-28 | 1.822E-33 | -1.282E-39 |
| 4 | -6.288E-10 | 1.539E-16 | -2.569E-22 | 3.431E-29 | 8.435E-34 | -7.209E-40 |
| 10 | -1.091E-10 | 3.018E-16 | -1.782E-21 | 5.905E-27 | -1.023E-32 | 6.986E-39 |
| 13 | -3.354E-13 | - | - | - | - | - |

| # | 1 | 2 | 3 | 4 | 10 |
|---|---|---|---|---|---|
| **Max Aspheric Departure [mm]** | 1.0 | 0.9 | 50.4 | 82.5 | 4.8 |
| **Max Slope Departure [°]** | 0.1 | 0.3 | 27.8 | 37.5 | 3.3 |

## 6.3 Double Cassegrain

The Ritchey-Chretien solution for a Cassegrain telescope takes only three input parameters (the separation of the mirrors, the back focal distance, and the focal length) and the shapes of the mirrors are analytically determined (i.e. the radii of curvature and conic constants). This solution can be obtained by using 4$^{th}$ order aberration theory with aspheric wavefront adjustments [52]. Obtaining analytical solutions for other telescopes is possible using 4$^{th}$ order aberration theory, but it is very challenging once there are more than two powered mirrors. However, if there are still only two powered mirrors, but four reflections instead of two, an analytical solution is still possible. The solution to this scenario is called the double Cassegrain telescope. The double Cassegrain telescope opens the doorway to a new class of telescopes.

The double Cassegrain telescope consists of two mirrors of relatively low power. Light reflects from the outer ring of the primary mirror to the outer ring of the secondary mirror. It then reflects from the inner ring of the primary mirror and then central region of the secondary mirror. The primary mirror has one conic constant, and the inner and outer parts of the secondary mirror have two different conic constants. The only parameters required are the same as for a Cassegrain telescope, the separation of the mirrors, the back focal distance, and the focal length (see Figure 6.3). With three different conic surfaces three aberrations can be corrected: spherical, coma, and astigmatic aberrations.

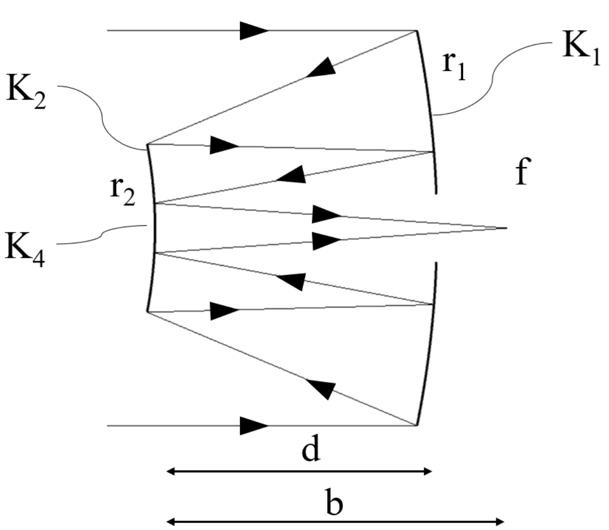

*Figure 6.3: General layout of double Cassegrain telescope. Light reflects from both the primary mirror and secondary mirror twice. The inner part of the secondary mirror has a different conic constant from the outer, though the radius of curvature is identical.*

In general, the primary is hyperboloidal with a large aperture, which introduces a lot of negative spherical aberration, as well as some coma and astigmatism. The secondary also tends to be hyperboloidal, which introduces an opposite amount of spherical aberration, coma, and astigmatism. A slightly converging beam is then incident on the smaller central region of the hyperbolic primary, and only a small amount of positive spherical aberration is introduced. The central region of the secondary mirror tends to be elliptical, which allows for negative spherical aberration to be introduced. Collectively, three different conics allows for perfect 4th order correction of three aberrations. With spherical, coma, and astigmatic aberrations corrected, the imaging surface is the Petzval surface. Note, this means that if a solution is found where the radii of curvature of both mirrors is identical, then the Petzval surface is flat.

The advantages of the double Cassegrain telescope include a larger field of view, a compact geometry, and an alignment procedure like a Cassegrain telescope. The challenges involve more complicated baffling, and a large central obscuration. To view the analytical solution to this telescope, see Appendix E.

As a specific example, if a telescope were desired where the separation of the mirrors is 100 mm, the back focal distance is 125 mm, the focal length is 1000 mm, and the focal ratio is F/7. A Ritchey-Chretien telescope would only be diffraction limited in the visible spectrum over a 0.3° FOV, and a Double-Cassegrain telescope would be diffraction limited in the visible spectrum over

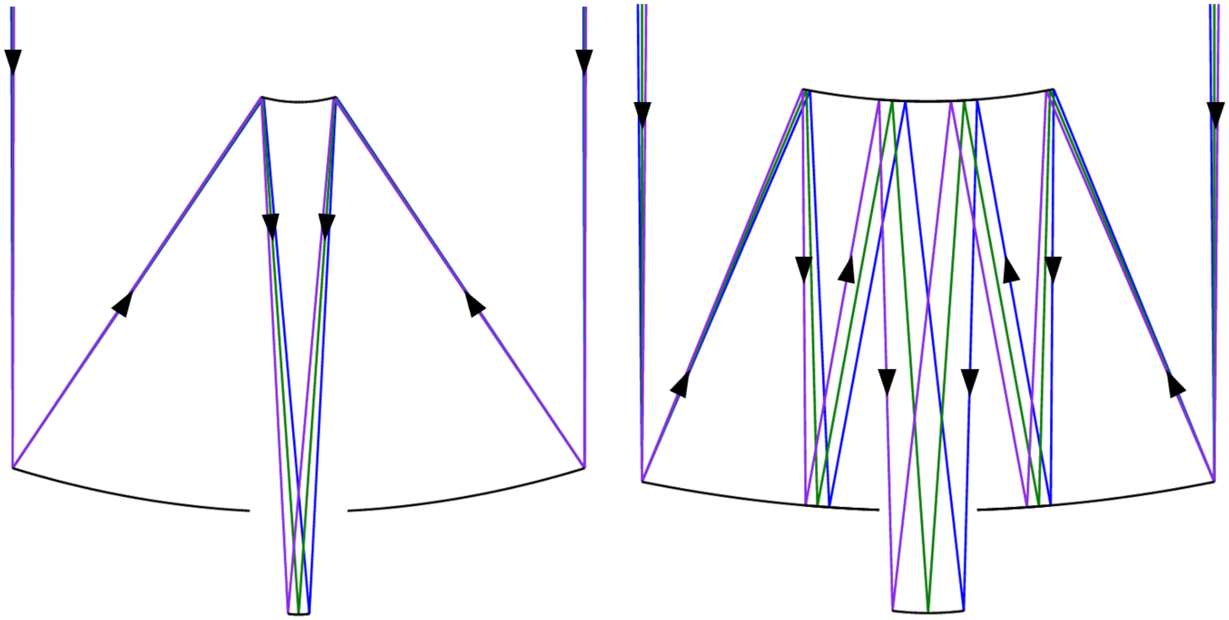

*Figure 6.4: A 140 mm Ritchey-Chretien telescope design (left) and a Double-Cassegrain telescope design (right) both with the same mirror separation, back focal distance, and focal length. The field of view by area is more than 10 times as much for the Double-Cassegrain.*

a 1.0° FOV, both with curved focal surfaces. Additionally, the Cassegrain telescope has steeper curvatures to fit within the same geometry, thus there is tight tolerancing (see Figure 6.4).

The Double-Cassegrain telescope can serve as a starting point for a wide variety of telescope designs. Faster focal ratios are possible while retaining diffraction limited imaging if higher order even aspheric terms are implemented during optimization. The real limitation is the necessity for baffling. While the secondary mirror and baffling of a Ritchey-Chretien Cassegrain telescope can block <10% of the incoming light, the Double-Cassegrain telescope must block >40% of the incoming light or straylight will degrade the imaging. As a result, the diffraction-limited resolution tends to be worse and the contrast of the MTF at high spatial frequencies is reduced. Nevertheless, large fields of view are readily attainable.

Other adjustments to the Double-Cassegrain telescope include variation of the radii of curvature of the inner primary and secondary surfaces, which can allow for faster and more compact geometries. Additionally, the separation of mirrors can be varied to obtain interesting geometries where central obscuration can be reduced, and baffling can be simplified. Of course,

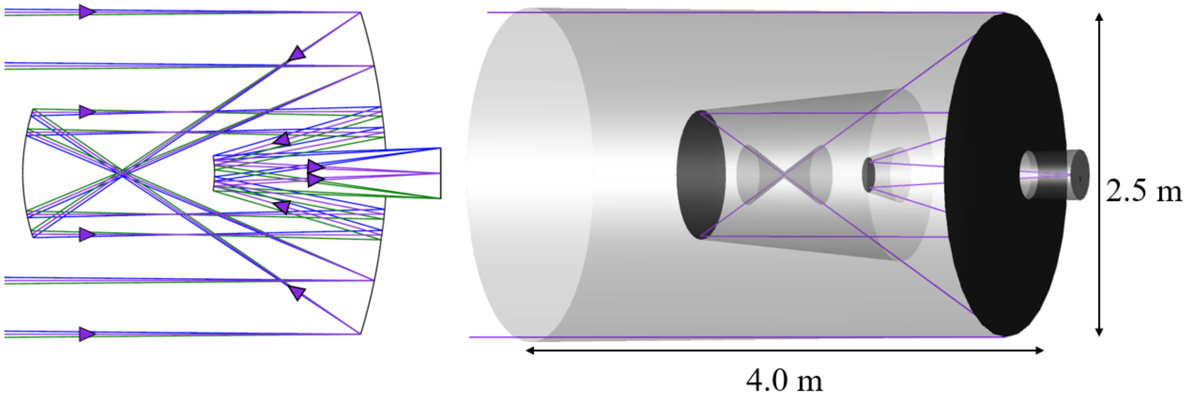

*Figure 6.5: A Gregorian-Cassegrain variant of the Double-Cassegrain telescope for a 2.5 m diffraction limited UV telescope with a 1.0° FOV (left). The baffling blocks about 30% of the incoming light (right). Note, the Petzval surface is flat.*

the alignment is no longer like a Cassegrain telescope at that point. Nevertheless, new axially symmetric telescope designs are possible beginning with the Double-Cassegrain solution.

A few examples illustrate the power of a four-reflection telescope. A Gregorian-Cassegrain variant makes it possible to create a 2.5-M F/9.0 diffraction-limited UV (360 nm) space telescope with a wide 1.0° field of view. Additionally, the baffling blocks only 30% of the incoming light (see Figure 6.5).

Another variant retains the fixed separation of the primary and secondary mirrors but varies the radii of curvature of the inner surfaces as well as the even aspheric terms. About 56% of the light is obscured, but the 8.4 m telescope focuses at F/9.0 for a 5.0° FOV with 80% of the encircled energy at 550 nm into <0.4 arcseconds. The telescope is capable of being perfectly baffles, though this is the cause for the large central obscuration (see Figure 6.6).

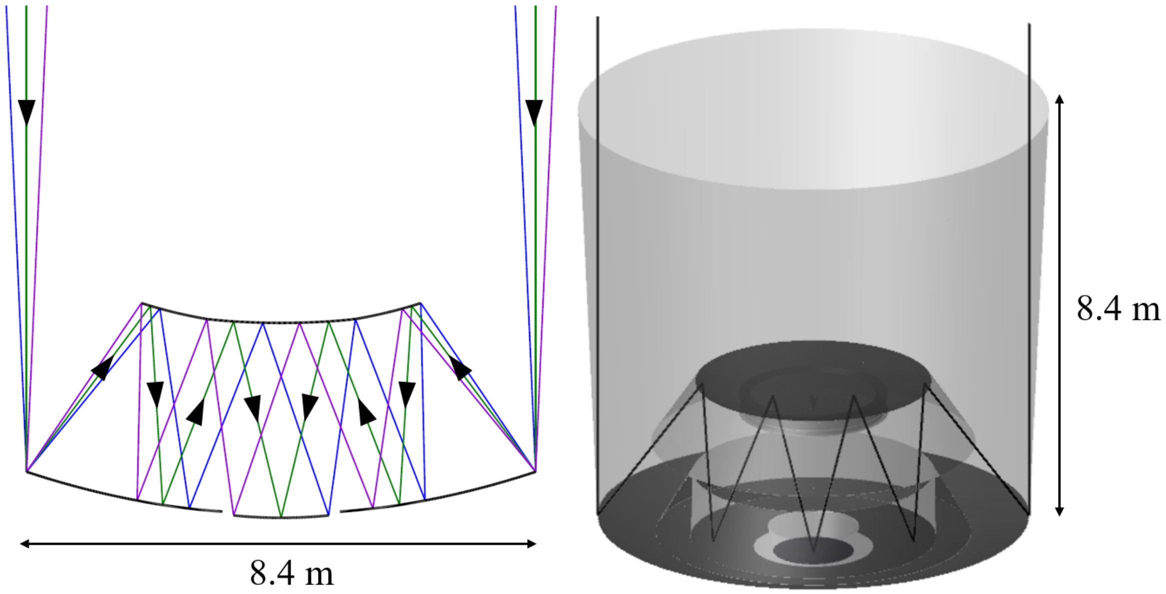

*Figure 6.6: 5.0° 8.4 m double Cassegrain telescope (left). The telescope is fully baffled, admitting only light within +/- 2.5° (right).*

## 6.4 Four Mirror 20-m Space Telescope with Diffraction Limited 1.0° FOV

In the paper "A 20 m wide-field diffraction-limited telescope", published by Phil. Trans A, a telescope design is introduced with applications as a space telescope or potentially a Moon telescope near an outpost on the Moon. The paper, written by Eads and Angel, provides greater details on the potential applications of such a telescope [53]. This telescope is another four-reflection telescope, though all four mirrors are separated, and the design is closer in nature to a Cassegrain-Mersenne rather than a double Cassegrain. Contained within this section is a deeper discussion of the design process for this telescope, and the motivation for the design goals. Due to the discussion of similar content, there is some overlap between this section and the cited paper.

Modern telescopes are moving towards an improvement over the Hubble Space Telescope (HST) in one of two ways. Telescopes are either moving to a larger field of view with the same resolution (as in the Roman Space Telescope [54]) or they are moving toward a larger aperture with higher resolution (as in LUVOIR [55]). No modern telescopes are seeking to improve upon both in a significant manner. Thus, it is of interest to push the limits of modern telescopes by increasing both the field of view and the diffraction limited imaging. The Hubble Space telescope has a field of view of several arcminutes. The goal of the proposed telescope design was to increase this field of view to 60 arcminutes. Additionally, a diffraction limited resolution of ~0.01" would improve upon Hubble by nearly an order of magnitude, thus a 20-m primary mirror aperture was chosen.

If the field of view is a few arcminutes, classical solutions to such a large telescope involve 3-mirror or 4-mirror anastigmats [56,57]. With modern lens design tools, it is possible to take one of these classical designs and push it towards a more powerful design, where the limitations for performance are often geometric constraints, such is vignetting. Due to the desire for a pupil image in the system, where wavefront errors from the primary mirror could be corrected for a wide field, a 4-mirror design was investigated with a form similar to Sasián's [58], but allowing for all mirrors to be aspheric out to the 14th order.

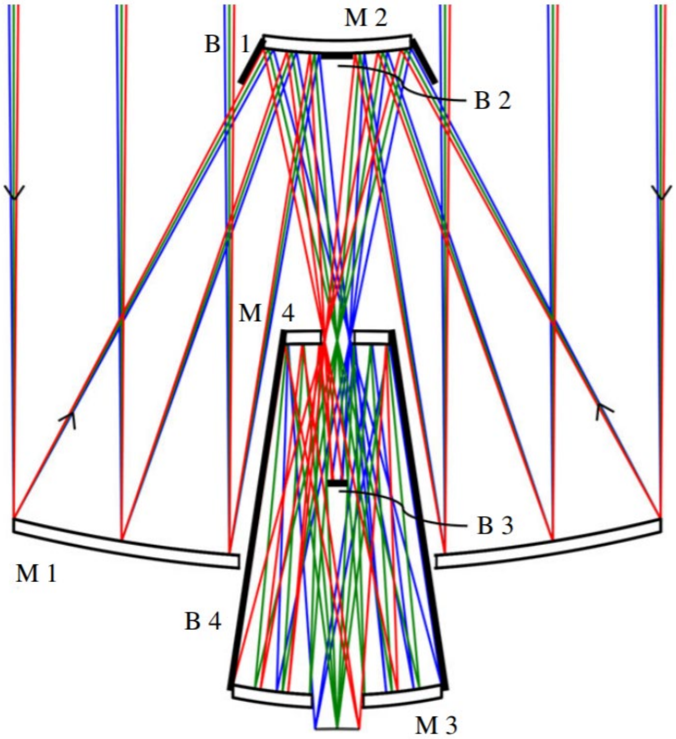

*Figure 6.7: Optical design of a 20-m telescope with a 1° FOV. Baffles are put in place to show the simplicity and to confirm stray-light performance of the telescope.*

A few additional design goals were established to push the design towards a solution that was fully baffled, had small vignetting, worked at F/4, and operated from UV through IR. The goal of a focal ratio greater than or equal to F/4 was so that the image could be adequately sampled at 1μm wavelength with available HgCdTe detectors with 10μm pixels. Additionally, working at a faster focal ratio of F/4 keeps the detector size smaller for a large 1.0° field, and reduces the vignetting for large off-axis field angles.

The optical design settled upon is shown in Figure 6.7. The path of rays is such that the primary and secondary mirrors form a cassegrain telescope that is poorly corrected. The size of the focus is such that it is smaller than the central obscuration of the pupil image formed on the quaternary. Also, locating M4 at the cassegrain focus made it possible to minimize the size of M4 so that it did not cause vignetting of rays reflected from the primary mirror. The ratio of central hole size of M4 relative to the outer diameter could not exceed the ratio of central obscuration of the primary relative to the primary diameter.

After the cassegrain focus, light reflects from M3 and a pupil image is then formed on M4. Light then comes to a focus through a hole in M3. One issue with this design is the direct light path from M2 to the focus. Thus, a baffle between M3 and M4 is necessary to block light along this straylight path. This placement is unfortunate, since it causes off-axis field angles to have three additional central obscurations. Fortunately, these obscurations do not amount to very much (see Figure 6.8).

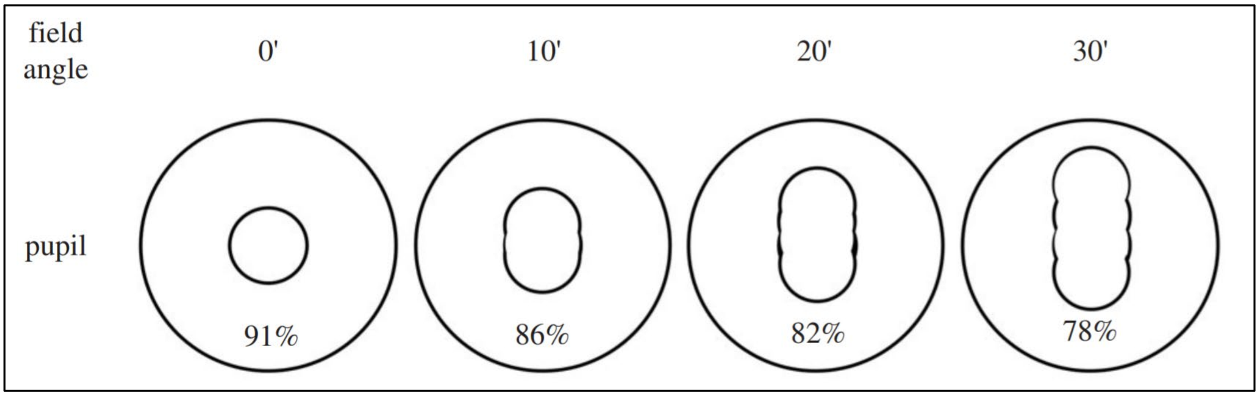

*Figure 6.8: Central obscuration of pupil versus field angle. On-axis has 91% of the light transmitted to the image plane while large field angles have less due to baffling (78% at the edge of the field).*

The on-axis central obscuration causes 9% of the light to be removed from the pupil while off-axis angles get no worse than 22% of the light removed from the pupil. This does have an effect on the PSFs for off-axis angles, but it is not so great that the strehl ratio is significantly affected. In Figure 6.9, the PSFs for the telescope across the field of view and for different wavelengths are provided. The 250 nm and 500 nm wavelengths would be imaged onto a silicon detector and the HgCdTe detector would be used for the 1 μm and above wavelengths, both of which have predicted future sized pixels. The performance at 500 nm out to nearly +/- 20’ is above 80% strehl, which is 10 times the diffraction limited field of LUVOIR at 500 nm (by solid angle).

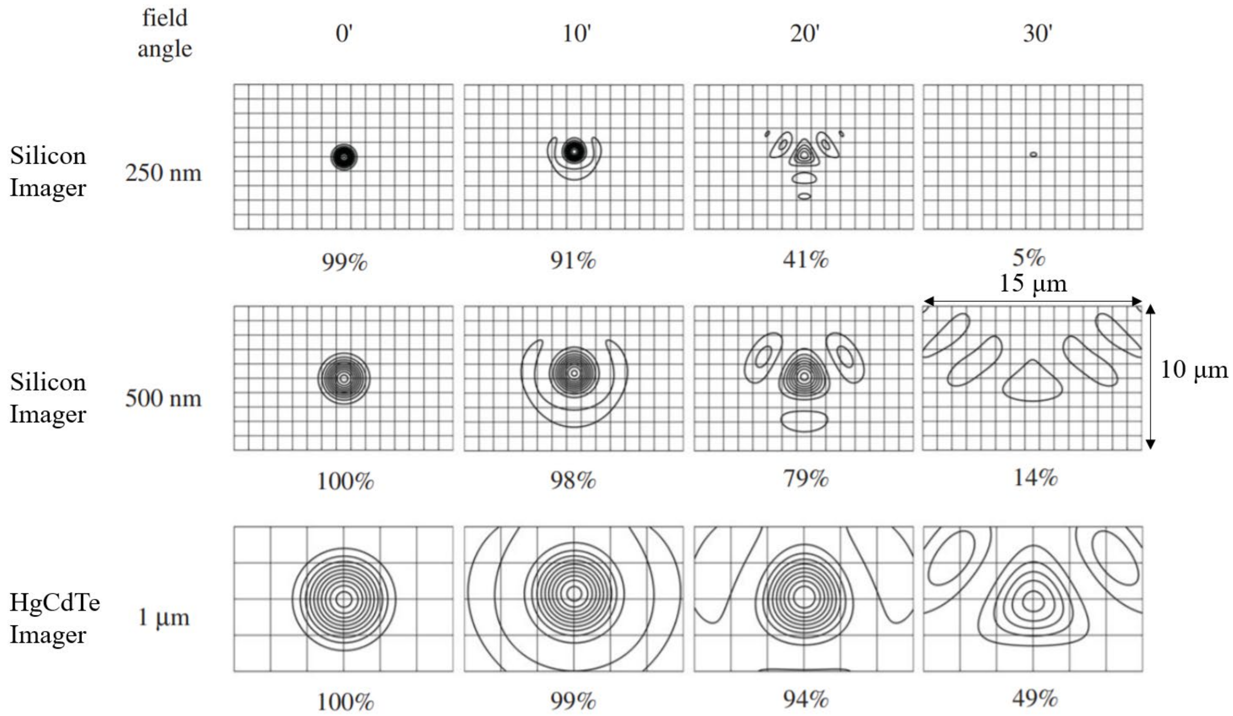

*Figure 6.9: PSFs for the 20-m telescope across the field of view for various wavelengths. The strehl ratio for each PSF is provided below each. Contour lines are spaced at 10% intervals from 5% up to 95%. Diffraction limited performance is obtained for 250 nm out to +/- 10', and 500 nm out to +/-20'. 1 µm wavelength is not quite diffraction limited at the edge of the field, but still has a high strehl ratio of 49%. Two types of imagers are presented where the silicon imager has 1 µm pixels and the HgCdTe imager has 2.5 µm pixels. Both are guesses at what may be possible in a few decades. Due to noise limitations, multiple exposures would be required, a method used by cell phones, which often use ~1 µm pixels.*

The straylight performance of this telescope is nearly perfect. The baffles shown in Figure 6.7 are modelled as perfectly absorbing surfaces (in a real telescope, they would be made with a series of concentric rings). Using these baffles, a reverse ray trace was performed from the image plane. The source was the size of the detector, and angles varied out to +/-90° for the initial trace. A very large detector was placed in front of the telescope to determine what rays were able to make it out of the telescope. No rays were detected outside +/- 0.5° angle of incidence upon the detector. The converse of this ray trace must also then be true. Any rays traced from the sky towards the telescope outside of +/- 0.5° field angle cannot make it to the detector plane. Thus, the telescope is well baffled. The resulting relative radiant intensity of this reverse ray trace is provided in Figure

6.10. It is notable that the radiant intensity follows the expected form of 91% on-axis and 78% off-axis (from Figure 6.8).

In conclusion, this 20-m telescope forms a basis for further investigation for the manufacture of a large space or lunar-based telescope. The optical performance shows a resolution gain by a factor of 8 compared to Hubble, also with a larger field of view. Some discussion of tolerancing and methods for making such a telescope, as well as placement on the moon, are provided in “A 20 m wide-field diffraction-limited telescope” [53].

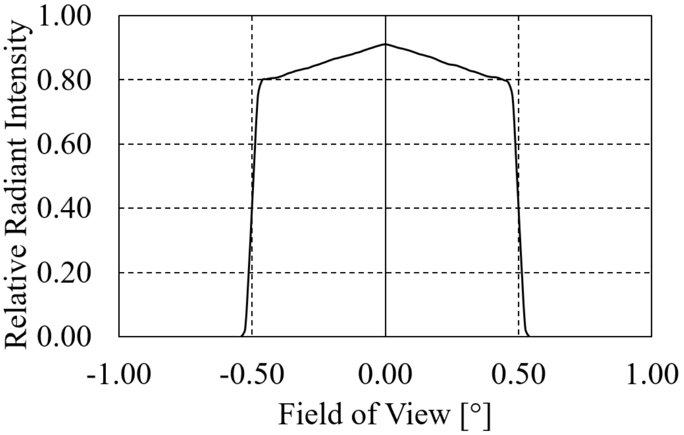

*Figure 6.10: Reverse ray trace from the image plane of the telescope. Rays outside the desired +/- 0.5° FOV do not make it to the sky, therefore rays outside this FOV do not make it from the sky to the image plane. Interestingly, the relative radiant intensity follows the same profile as shown in the pupil images. On-axis angles transmit with ~90% efficiency and edge of the field angles transmit with <80 efficiency.*

## 6.5 Oxygen Spectroscopic Telescope with 300,000 Resolution

Earth-like exoplanets are of great scientific and public interest. Whether a planet has primitive life is indicated by the presence of oxygen in the atmosphere made by that life. Thus, life on exoplanets can be identified by observing the oxygen absorption spectrum from distant stars that pass through a transiting exoplanet.

It is possible to identify these spectral characteristics of an exoplanet using a large telescope. However, it may be cheaper and more powerful to use a collection of small telescopes, ~1 m in diameter. The E-ELT has a diameter of 39 m, which has a collection area of 1100 m$^2$ [49]. Using a large array of 1m telescopes would require ~1,500 telescopes to have a similar collection area. To analyze the spectrum of light passing through an exoplanet, each telescope would image the associated star into a fiber, and bundles of fibers would feed to custom Littrow spectrometers. Multiple spectrometers would be necessary to accomplish the task, about five.

There is a trade space to be explored where light gathering power is balanced against the need for adaptive optics. If smaller 0.5 m telescopes are used, then only fast tip-tilt is needed to keep a high strehl star image centered on the fiber. A tip-tilt mirror would be used to keep the brightest speckle centered on the fiber so that the fiber coupling efficiency is maximized [50]. However, four times as many telescopes and spectrometers are needed compared to a 1.0-m telescope. Additionally, the light gathering power of a single 0.5 m telescope may make it necessary for ~1-hour exposures for a magnitude 12.5 star. There is a trick that could be used to make a 0.5 m telescope possible though. It is necessary to understand the workings of the spectrometer before this trick can be adequately explained.

A Littrow spectrometer uses light emitting from a line of fibers placed at the focus of an achromatic lens. This light is thus collimated by the said lens. Placing a tilted reflective echelle grating in the collimated space will cause the spectrum to reflect with angular separation, in perhaps the vertical direction. This spectrally separated light then returns through the achromatic lens and comes to a focus in the same plane where the fibers are located. At this plane a CCD or CMOS sensor is placed to obtain a measurement of the split spectrum. The trick for using a 0.5 m fiber telescope involves the use of a CCD.

If a CCD were used, then each row of pixels could be associated with a certain wavelength of light coming from multiple fibers running down an entrance slit. Instead of reading one pixel, the charge from an entire row could be accumulated before readout, giving plenty of a photoelectrons to get above the noise. The issue with this trick is getting all the fibers from different telescopes aligned just right. This can be challenging because the use of an echelle grating produces smile distortion at off-axis positions.

Yuan et. al state that smile distortion for a diffraction grating can be derived from the grating equation. It is geometric distortion that should be corrected in the design phase [51]. Since a straight line of fibers produces a parabolically curved spectrum, the converse is true, and this distortion can be corrected by having the fibers positioned in the opposite curve. The tolerancing of the fiber positions is rather tight, within a few microns. Though according to Yuan et. al this is desirable to keep the data reduction simple. Thus, a CCD could be used to read out one row of data at a time, and 0.5 m telescopes are made practical.

Reading out data in a photon starved scenario is possible, but perhaps not ideal. Therefore, a 1-m fiber telescope may be the better option. However, a deformable mirror and adaptive optics wavefront correction is then necessary to obtain a high strehl ratio, and an associated high fiber coupling efficiency. The telescope was chosen to have an F/5 focal ratio to couple well into the fiber. At 765 nm wavelength (the oxygen wavelength) an F/5 focal ratio produces an airy disk (width across first dark ring) that is about 9 microns in diameter. Fibers 9 micron in diameter are commercially available, which is why F/5 was chosen. These fibers also have claddings around 125 microns in diameter, which limits the number of fiber feeds to a given spectrometer. Another advantage to F/5 is that a prime focus telescope can be used without the need of other powered mirrors and will still obtain nearly diffraction limited imaging for a +/- 1 arcminute field, all that is necessary for finding. Additionally, an array of 1-m telescopes could be mounted on the same structure, and the balance of the structure is reasonable with the adaptive optics and fiber located ~5 meters above the primary.

One other desirable characteristic of 0.5 or 1.0 m telescopes is to make them robust so that a dome is not necessary to protect the telescope, and to integrate a fast tip-tilt mirror to compensate for wind rocking the telescope. A large portion of the cost of a telescope is then removed. This could require an optically non-distorting glass window above the fiber across the whole entrance aperture to protect the mirror coating. However, the additional weight at the top of the telescope causes structural challenges. We have explored the use of a back silvered mangin primary mirror instead. The coating would be well protected on the back of the primary mirror and based on solar experience, would last many decades. Since the focal ratio is only F/5, chromatic change in focus is small.

The design of the telescope is thus a paraboloidal mangin mirror with a Newtonian fold mirror, and subsequent fold mirrors for minimizing geometry. A deformable mirror for the 1.0 m telescope could be a Newtonian fold mirror, or a subsequent mirror. A spectral filter could then be used to transmit the oxygen band (from 759 nm to 771 nm) and reflect all other wavelengths to a wavefront sensor for determining deformable mirror shape changes. This wavefront sensor may only need to be a pyramid wavefront sensor due to the small 1-m size of the telescope. The mangin mirror could be cheaply made by spin casting (on perhaps liquid tin), and then figuring the final shape on one or both surfaces.

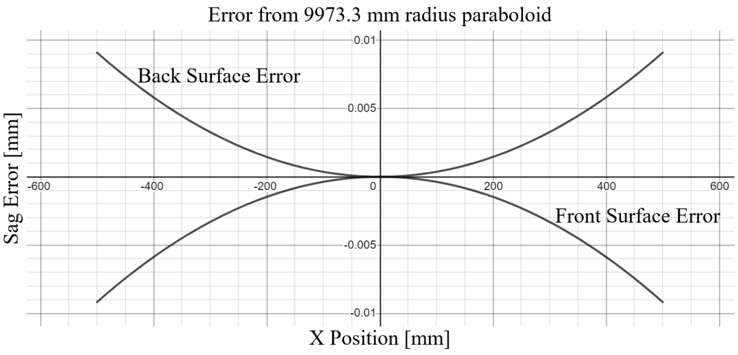

*Figure 6.11: Shape error from spin casting a 1-m paraboloidal mangin mirror working at F/5, to the median shape.*

For an F/5 1.0 m telescope spun to a median radius of curvature this would require the front and back surfaces to have ~9 microns PV polished out (see Figure 6.11).

*Table 6-2: Prescription for mangin mirror paraboloidal fiber telescope for oxygen spectroscopy.*

| # | Radius | Y | Z | Material | Mech Semi-Dia | Conic | Tilt Angle [°] |
|---|---|---|---|---|---|---|---|
| 1 | -9965.999 | 0.000 | 0.000 | N-BK7 | 500.000 | -1.000 | - |
| 2 | -9980.546 | 0.000 | 25.400 | Mirror | 500.000 | -1.000 | - |
| 3 | Infinity | 0.000 | -4200.000 | | 123.008 | - | 45.000 |
| 4 | Infinity | -600.000 | -4200.000 | Mirror | 28.506 | - | 45.000 |
| 5 | Infinity | -600.000 | -4100.000 | Dichroic Mirror | 8.295 | - | -7.500 |

The prescription for the telescope is provided in Table 6-2. The Newtonian fold mirror removes the central 6.5” of the incoming light, a small 2.6% loss of light. A second fold mirror helps to minimize geometry while also providing the means for wavefront correction as a deformable mirror. A final dichroic mirror transmits the oxygen spectrum and reflects all other

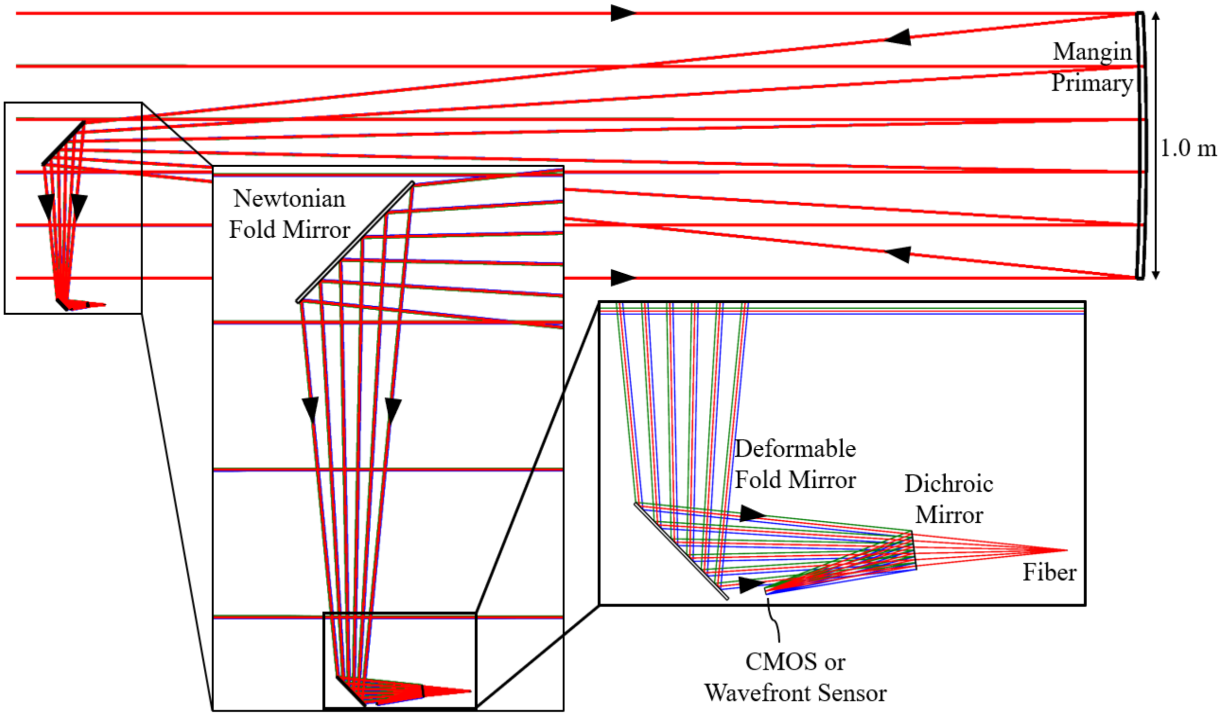

*Figure 6.12 Layout of mangin fiber telescope with a 2 arcminute FOV working at F/5 from 0.4 – 1.0 micron wavelength. The Newtonian fold mirror is followed by a second fold mirror, which could be deformable. This is not located at a pupil position; thus, atmospheric correction only occurs on-axis. A dichroic mirror transmits the oxygen spectrum to a fiber and reflects the remaining light onto a CMOS sensor or wavefront sensor.*

wavelengths to a wavefront sensor or CMOS for tip-tilt. Figure 6.12 shows the system layout in detail.

This telescope design reveals a way to make a cheap, yet powerful array of telescopes for spectroscopic applications. Additionally, this design is optimized for high efficiency throughput to the spectrometer. At F/5 the numerical aperture (NA) of the focused beam is 0.1, below the maximum NA of most fibers. Also, since the fiber is sized similar to the airy disk, up to 84% of the collected light is coupled into the fiber. After transmission through a multi-mode fiber, the light will have a larger NA, thus the lens in the spectrometer for imaging the fibers would work at F/4 to ensure collection of all the light.

The spectrometer takes fibers from an array of Mangin Newtonian telescopes. The goal of the spectrometer design was to search for A band oxygen absorption (759 nm to 771 nm) with a resolving power of 300,000 to get high signal to noise ratio. The Littrow spectrograph uses a 400 mm focal length achromatic lens with a large field of view. It collimates light from the fiber inputs onto a large 100 mm by 400 mm echelle grating with 74° blaze angle (see Figure 6.13). The echelle grating used at 74° angle of incidence was modelled in Zemax with 78.5 lines/mm and using 32$^{nd}$ order.

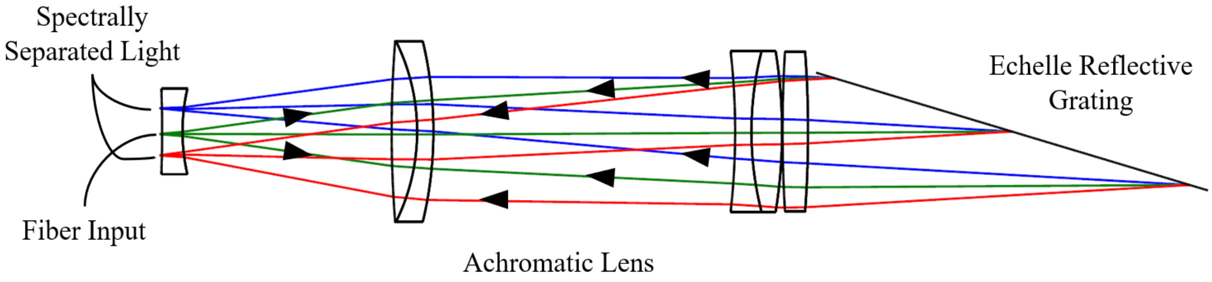

*Figure 6.13: Littrow spectrometer with fiber input at the focus of an achromatic lens, which collimates the light onto a reflective echelle grating. Returning light is spectrally separated and images onto an array of sensors.*

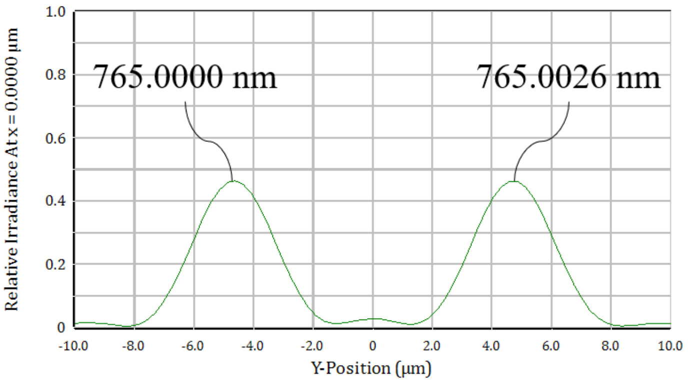

*Figure 6.14: Cross section of two point spread functions overlapped. A small spectral separation of 0.0026 nm results in a complete separation of the airy disks, i.e. 300,000 resolution. Note, if resolution is defined by the peak of one PSF located at the minimum of the other PSF, then the resolution is increased to 600,000.*

This diffraction grating dramatically separates the oxygen spectrum across 44 mm at the focus of the achromatic lens, with each PSF approximately 7.4 µm in diameter. Putting in 765 nm and 765.0026 nm results in the cross section of the PSFs shown in Figure 6.14. The two PSFs are separated such that their minima are overlapping, thus a resolution of 300,000 is obtained. If resolution is instead defined by the Rayleigh criterion, then the resolving power is 600,000. The CCD or CMOS sensor used needs perhaps 3 µm pixels to well sample the diffraction limited spots.

The horizontal dimension of the fiber line is 48 mm across, and the fibers follow a nearly parabolic curve, where the edges of the line are displaced by 5 mm relative to the center (i.e. the sag of the curve). This produces spectra that are all dispersed in a similar manner (i.e. minimizing smile distortion). The reflection from the echelon grating brings symmetry into the lens, which significantly reduces any distortion in the lens, but due to the grating there is still some residual pincushion distortion. The blue part of the spectrum is shifted slightly up and outward at the edges

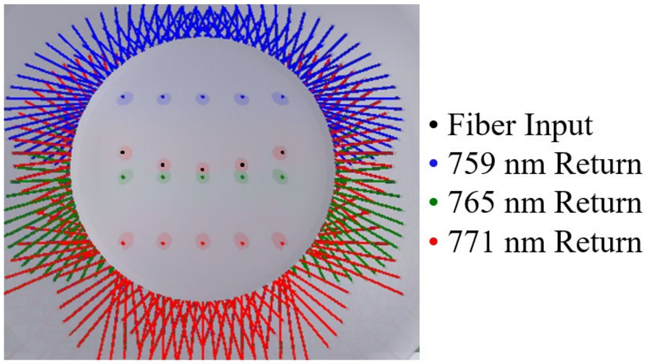

*Figure 6.15: Axial view of Littrow spectrometer. Fiber inputs are in black, the returning beams are shown according to their color in the oxygen spectrum. CMOS or CCD sensors would be tiled in an array on the image surface that minimizes distortion effects.*

of the field and the red part of the spectrum is shifted slightly down and outward at the edges of the field, both about 75 µm (see Figure 6.15). This slightly distorted spectrum can be remedied by placing an array of sensors across the image plane where sensors at the edge of the field are slightly clocked. By combination of this spectrometer with fiber feeds from hundreds of telescopes, and by using multiple spectrometers, a high spectral resolution of oxygen wavelengths from distant stars is possible.

In particular, this design shows that by using a series of Newtonian Mangin telescopes that feed star images into fibers at the diffraction limit, in the spectral region from 759 nm to 771 nm can be analyzed with 300,000 resolution. If resolution is defined by the Rayleigh criterion, then the oxygen spectrum is resolved with 600,000 resolution. If fibers could be position in the imaging plane within 125 µm of each other, then over 400 telescopes could feed fibers to a single Littrow spectrometer. To obtain the light gathering power of an ELT about 1,500 1.0-m aperture telescopes would be required, though adaptive optics for each telescope would be required. If smaller 0.5 m telescopes were used then only a fast tip tilt mirror would be required, but the effects of distortion would need to be well-corrected so that each wavelength could be read out in a row. Whichever variant is used, the telescope array as discussed in this section could inexpensively open the doors to direct observation of exoplanet spectra to determine if a given exoplanet has life produced oxygen.

## 6.6 Conclusion

This chapter has been a compilation of several optical designs for telescopes. Two of the designs have powerful spectroscopic applications from Earth. The first design would require a deeper investigation into the manufacture of large gull-wing lenses but could prove to be a useful addition for dark energy characterization. The second design is an inexpensive option for moving towards Earth-like exoplanet identification by use of a large array of small 1-m telescopes each feeding fibers to Littrow spectrometers. The third design has the potential to be a next generation UVOIR telescope with a large field of view and a high resolution (8 times better than Hubble). Additionally, it could serve as a spectroscopic telescope, depending on the carousel of instruments chosen.

Optical design of modern telescopes has been greatly enhanced by the new tools and software that have been placed into the hands of the optical designer. A merit function can be defined to show improvement for any number of design parameters, allowing the discovery of designs that could not be found years ago. These new designs often rely upon the heritage left by optical designers of the past. More specialized and even free-form optics may soon become the norm, only made possible because of the progress made by scientists who have gone before.

# CONCLUSIONS

This dissertation has been a presentation of optical and metrology designs for telescopes and solar energy. While seemingly unrelated, both areas rely upon the same principles of optical sciences: geometric optics, aberration theory, diffraction theory, interferometry, laser propagation, etc. The main difference between the two areas is the precision and accuracy necessary to fulfill system requirements.

For solar optics, <1 mrad RMS accuracy is all that is desired. The angular size of the sun is 0.5° or 8.7 mrad. Thus, the solar disk can be blurred to a size of about 10.7 mrad, where concentration is reduced by one third. Even at this level, solar energy can still be well used for electricity or heat generation (or hydrogen fuel generation). Because of this reduced accuracy requirement, the metrology for solar optics is either non-existent, or low in accuracy as well. It is proposed that only 0.2 mrad RMS metrology accuracy is required to obtain surface errors within 1 mrad RMS (at least for low-order surface errors). An experiment using a Laser Hartmann metrology system was herein presented, which showed an inexpensive heliostat metrology system that obtained the desired measurement accuracy for an actively focusing heliostat.

In contrast, telescope metrology systems require ~3 orders of magnitude higher accuracy and precision. Telescope optics are regularly finished to <20 nm RMS surface error. This is accomplished using expensive and specialized metrology systems, such as interferometers or tracking lasers. The Laser Hartmann metrology system for a deformable heliostat cost <$1,000 in equipment. Telescope metrology systems easily break $100K. Solar optics solely care about getting the Sun's light within a certain geometry. Telescopes have a similar goal, but also desire to form detailed images of stars and exoplanets. While diffraction theory is applicable to solar optics (e.g. mid-spatial frequency errors can scatter and diffract light into higher orders), telescopes are much more concerned with the effects of diffraction (e.g. the point spread function of a telescope depends on the Fourier transform of the entrance pupil of the telescope and the system aberrations).

Optical design and metrology can be applied fluidly between the two areas of solar optics and telescopes. There are additional complications to telescopes that require greater care in design and manufacturing, but generally there is a large level of funds that make it possible to achieve performance goals. In contrast, solar optics do not require so much precision in manufacturing, but they are greatly limited by cost. Competing with fossil fuels is challenging. Thus, there is a high level of creativity and care when designing a solar energy system. Achieving <1 mrad RMS errors for <$1/W is not easy.

Regardless of the area of consideration, the breadth of the optical sciences allows for its application to many different situations. When the goal is to define and achieve system requirements, the way that light interacts with objects can be predicted in different ways: Ray tracing, diffraction theory, Maxwell’s equations, etc. Part of defining and achieving system requirements is to know which theory should be used for a given scenario. This is part of what it means for an optical scientist to “Know thy requirements.”

# Appendix A : **DERIVATION OF THE IDEAL HELIOSTAT SHAPE**

This appendix shows in detail the calculations that led to the surface coefficients given in Chapter 3. Two approaches are given for the derivation of the tangential and sagittal radii of curvature: Aberration theory and the Coddington equations. Following the derivation of radii of curvature is the derivation of shape coefficients for an alt-azimuth mounted heliostat mirror.

## A.1 **4th Order Derivation**

According to 4th order aberration theory, there are five possible aberrations for an optical system: Spherical ($W_{040}$), Coma ( $W_{131}$), Astigmatism ($W_{222}$), Field Curvature ($W_{220}$), and Distortion ($W_{311}$) (see section 1.4). Of these aberrations, only Spherical, Coma, and Astigmatism contribute to a spherical surface mirror. According to the Seidel coefficient formulas, the aberrations are as follows: $W_{040} = \frac{1}{8}S_I = -\phi^3 y^4/32$, $W_{131} = \frac{1}{2}S_{II} = -\bar{u}\phi^2 y^3/4$, $W_{222} = \frac{1}{2}S_{III} = -\bar{u}^2\phi y^2/2$, $W_{220} = 0$, and $W_{311} = 0$ [13]. In these equations $\phi$ is the surface power, $y$ is the marginal ray height (or aperture radius), and $\bar{u}$ is the chief ray slope (or optical angle).

If the mirror shape is chosen to be a conic surface, then it is possible to cancel spherical aberration. The aspheric contribution of a mirror to the Seidel equations is $\delta S_I = a$, $\delta S_{II} = \frac{\bar{y}}{y}a$, $\delta S_{III} = \left(\frac{\bar{y}}{y}\right)^2 a$, $\delta S_{IV} = 0$, $\delta S_V = \left(\frac{\bar{y}}{y}\right)^3 a$, where $a = -\kappa\phi^3 y^4/4$, and $\kappa$ is the conic constant [13]. Since the heliostat mirror is the stop of the optical system, a change to a conic surface only affects the first term (Spherical aberration). If the conic constant $\kappa = -1$ (i.e. a paraboloidal surface), then $\delta S_I = \phi^3 y^4/4$. Thus, $\delta W_{040} = \phi^3 y^4/32$ and Spherical aberration is perfectly corrected with no effect on Coma or Astigmatism.

Choosing a parabolic surface, the wavefront error function is

$$W(\vec{H},\vec{\rho}) = W_{131}(\vec{H}\cdot\vec{\rho})(\vec{\rho}\cdot\vec{\rho}) + W_{222}(\vec{H}\cdot\vec{\rho})^2, \qquad \textit{Eq A-1}$$

which can be altered to

$$W(H,\rho,\theta) = -\frac{\bar{u}\phi^2 y^3}{4} H\rho^3\cos\theta - \frac{\bar{u}^2\phi y^2}{2} H^2\rho^2\cos^2\theta, \qquad \textit{Eq A-2}$$

where $y$ is the aperture radius, thus $\rho y = r = \sqrt{X^2+Y^2}$ . Choose $H$ to be in the tangential plane. Thus, $\bar{u}H = \bar{u}_{sun}$ (the optical angle of the Sun), $Y = r\cos\theta$. The wavefront error function simplifies to

$$W(X,Y,r) = -\frac{\bar{u}_{sun}\phi^2 r^2 Y}{4} - \frac{\bar{u}_{sun}^2\phi Y^2}{2}, \qquad \textit{Eq A-3}$$

which depends on the Solar angle in a quadratic manner. The second term, which is $\propto Y^2$, is the astigmatic term. This astigmatism can be corrected by making an additional aspheric adjustment to the surface shape (i.e. an additional wavefront term).

An increase in the optical path difference (OPD) is associated with a decrease in the surface sag. Additionally, a change in the surface sag results in twice the change in OPD, due to the double pass nature of reflective surfaces. Therefore, to correct for astigmatism, the change in sag must be

$$\Delta Z = -\frac{\bar{u}_{sun}^2\phi Y^2}{4} = -\frac{\bar{u}_{sun}^2 Y^2}{2R}, \qquad \textit{Eq A-4}$$

which is half of the astigmatic wavefront error.

The sag of the surface becomes

$$Z = \frac{Y^2}{2R}(1-\bar{u}_{sun}^2) + \frac{X^2}{2R}, \qquad \textit{Eq A-5}$$

which is a perfect parabola when the Sun is on-axis, as expected.

One other alteration to the sag is required. Aberration theory is based on the axial distance from the vertex being unchanged for different fields of view. In other words, the “z distance” is unchanged, but the traversed distance at off-axis angles increases (i.e. the hypotenuse, see Fig. A-1). This is not the case for heliostats where the distance from the vertex of the mirror to the target is unchanged for different angles. Thus, a defocus term needs to be added.

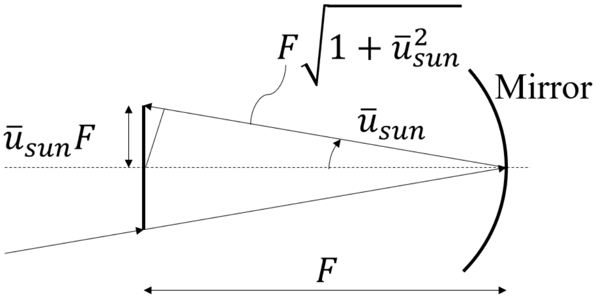

*Fig. A-1: Ray diagram showing the increase in focal distance at off-axis angles.*

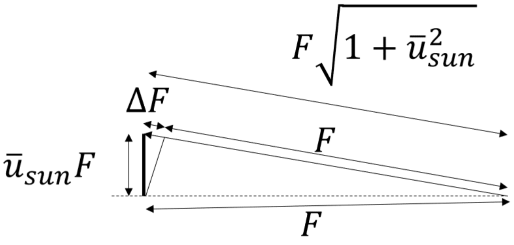

*Fig. A-2: Section of Fig. A-1 showing the required change in focus.*

This can be calculated by approximating the required change in focus (see Fig. A-2) where

$$\Delta F = F - F\sqrt{1+\bar{u}_{sun}^2} \approx F - F\left(1+\frac{\bar{u}_{sun}^2}{2}\right), \qquad \textit{Eq A-6}$$

which reduces to

$$\Delta F = -\frac{\bar{u}_{sun}^2 F}{2} = -\frac{\bar{u}_{sun}^2 R}{4}. \qquad \textit{Eq A-7}$$

For a mirror, the change in focus is equivalent to twice the change in radius,

$$\Delta R = 2\Delta F = -\frac{\bar{u}_{sun}^2 R}{2}. \qquad \textit{Eq A-8}$$

The change in sag of the mirror can be calculated using this change in radius and the ideal sag of the mirror:

$$Z = \frac{r^2}{2R} \qquad \textit{Eq A-9}$$

$$\frac{\Delta Z}{\Delta R} = -\frac{r^2}{2R^2} \qquad \textit{Eq A-10}$$

$$\Delta Z = -\frac{r^2}{2R^2}\Delta R = \frac{r^2}{2R^2}\frac{\bar{u}_{sun}^2 R}{2} = \frac{\bar{u}_{sun}^2 r^2}{4R} \qquad \textit{Eq A-11}$$

The addition of Eq A-11 to Eq A-5 provides

$$Z = \frac{Y^2}{2R}\left(1 - \frac{\bar{u}_{sun}^2}{2}\right) + \frac{X^2}{2R}\left(1 + \frac{\bar{u}_{sun}^2}{2}\right), \qquad \textit{Eq A-12}$$

which is the ideal shape for the heliostat mirror to correct for astigmatism. The tangential and sagittal radii of curvature are thus:

$$R_t = R/(1 - \frac{\bar{u}_{sun}^2}{2}) \qquad \textit{Eq A-13}$$

$$R_s = R/(1 + \frac{\bar{u}_{sun}^2}{2}) \qquad \textit{Eq A-14}$$

Coma is still present when choosing a surface with these radii of curvature. However, the amount of coma is significantly reduced at off-axis angles because of the increase of tangential radius of curvature at larger angles. In this scenario, coma does not increase linearly with the field of view. Rather, it is of a cubic form with no Coma on-axis or at ~80° angle of incidence (from Eq A-3):

$$W_{\max}(\bar{u}_{sun}) = -\frac{\bar{u}_{sun}\phi^2 y^3}{4} = -\frac{\bar{u}_{sun}(1-\bar{u}_{sun}^2/2)^2 y^3}{R^2}. \qquad \textit{Eq A-15}$$

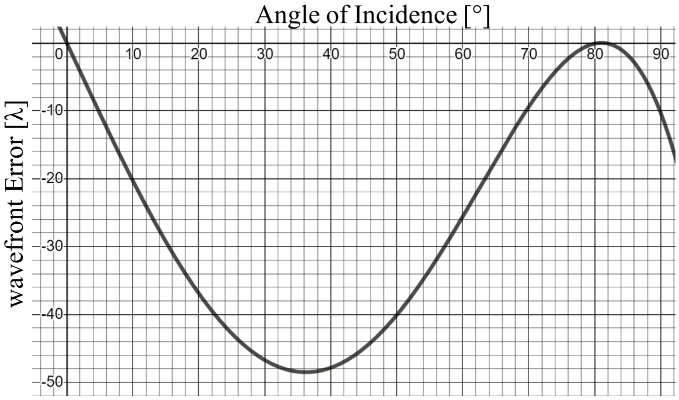

*Fig. A-3: Maximum wavefront error with active correction of astigmatic aberrations. λ is 550 nm, y is 750 mm, R is 80000 mm.*

The plot of Eq A-15 shows that the maximum wavefront error is ~50 waves for an F/27 1.5 m mirror (see Fig. A-3). The maximum reflected slope error can be calculated by taking the derivative of $W$ with respect to $Y$, then plugging in $y$ to get the maximum error. This turns out to be

~0.1 mrad maximum reflected slope error, which is much smaller than the errors introduced by bending a flat panel heliostat mirror.

Note, these equations are technically only valid for "small" angles of incidence. This is because 4th order aberration theory, while useful, is based upon the marginal and chief rays, which are accurate for only "small" angles. However, the final wavefront error equation (Eq A-15) is remarkably accurate. In contrast, the equations for the radii of curvature (Eq A-13 and Eq A-14) would introduce significant surface slope error for large angles of incidence. In order to derive radii of curvature that work for all angles of incidence, aberration theory is superseded by the Coddington equations.

## A.2 **Coddington Derivation**

The Coddington equations [13] are designed specifically to model astigmatic contributions by a surface. There are two imaging equations for the sagittal and tangential planes:

$$\frac{n'}{s'} - \frac{n}{s} = \frac{n'\cos(I') - n\cos(I)}{R_S}, \qquad \textit{Eq A-16}$$

$$\frac{n'\cos^2(I')}{t'} - \frac{n\cos^2(I)}{t} = \frac{n'\cos(I') - n\cos(I)}{R_t}. \qquad \textit{Eq A-17}$$

In these equations, $n'$ is the index of refraction in image space, $n$ is the index of refraction in object space, $s'$ is the sagittal image distance, $s$ is the sagittal object distance, $t'$ is the tangential image distance, $t$ is the tangential object distance, $I$ is the angle of incidence in object space, $I'$ is the angle of exitance in image space, $R_s$ is the sagittal radius of curvature of the surface, and $R_t$ is the tangential radius of curvature. For a heliostat mirror imaging the Sun, $n' = -1$, $n = 1$, $I' = -I$, and $s = t = \infty$. The equations thus reduce to

*Eq A-18*

$$\frac{-1}{s'} = \frac{-2\cos(I)}{R_s},$$

$$\frac{-\cos^2(I)}{t'} = \frac{-2\cos(I)}{R_t}. \qquad \textit{Eq A-19}$$

In these equations, $s'$ is the sagittal focal distance and $t'$ is the tangential focal distance. The effective tangential and sagittal radii of curvature can thus be defined as $R_{s,eff} = 2s'$ and $R_{t,eff} = 2t'$, and the effective radii of curvature are calculated as

$$R_{s,eff} = R_s/\cos(I), \qquad \textit{Eq A-20}$$

$$R_{t,eff} = \mathrm{R_t}\cos(I). \qquad \textit{Eq A-21}$$

In order to have both effective radii of curvature such that the sagittal and tangential focal distances are the same, the sagittal and tangential radii of curvature should be chosen such that $R_{s,eff} = R_{t,eff} = R$. Thus,

$$R_s = R\cos(I), \qquad \textit{Eq A-22}$$

$$R_t = R/\cos(I). \qquad \textit{Eq A-23}$$

The effective radii of curvature are <u>changed</u> by the angle of incidence. The actual radii of curvature are <u>chosen</u> so that the effect caused by off-axis angles is corrected. Performing a polynomial expansion on these equations yields

$$R_s = R\left(1 - \frac{I^2}{2!} + \frac{I^4}{4!} - \frac{I^6}{6!} + \cdots\right), \qquad \textit{Eq A-24}$$

$$R_t = R/\left(1 - \frac{I^2}{2!} + \frac{I^4}{4!} - \frac{I^6}{6!} + \cdots\right). \qquad \textit{Eq A-25}$$

Removing terms higher than order 2, and applying a reciprocal binomial approximation to Eq A-24 yields

$$R_s \approx R/\left(1 + \frac{I^2}{2}\right), \qquad \textit{Eq A-26}$$

$$R_t \approx R/(1-\frac{I^2}{2}). \qquad \text{Eq A-27}$$

If $I$ is replaced by $\bar{u}_{sun}^2$ then we recover Eq A-13 and Eq A-14, which validates the use of aberration theory. An alternative comparison of 4th order theory and the Coddington equations for astigmatism has been previously established [59]. With more exact equations for the desired radii of curvature the shape of the mirror can be calculated for an alt-azimuth mounted heliostat.

## A.3 **Shape Coefficients for an Alt-Azimuth Mounted Heliostat**

A heliostat is designed to reflect sunlight onto a target, which scenario is composed of three vectors, the solar vector $\vec{S}$, mirror vector $\vec{M}$, and tower vector $\vec{T}$ (see Fig. A-4). The plane containing all three of these vectors is the tangential plane. The angle of astigmatism on the surface of the heliostat mirror is given by the projection of the solar vector onto the surface of the mirror $\vec{S}_{projected}$.

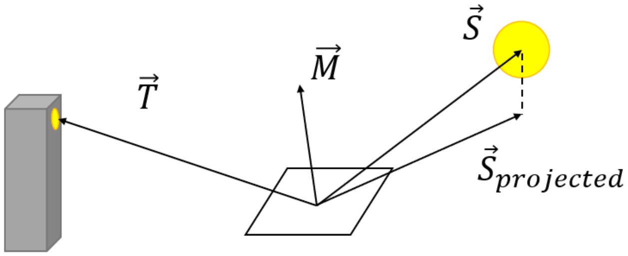

*Fig. A-4: A heliostat focusing sunlight onto a tower. This scenario defines three important vectors: the solar vector $\vec{S}$, mirror vector $\vec{M}$, and tower vector $\vec{T}$. Included also is the projection of the solar vector onto the surface of the mirror $\vec{S}_{projected}$.*

The orientation of the solar vector is essential to calculating the shape of the heliostat. The widely accepted equations for calculating the solar position were initially discovered by Jean Meeus [60]. The NOAA solar position calculator is based on these

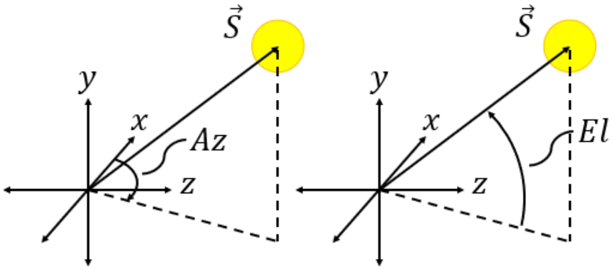

*Fig. A-5 Illustrations showing the azimuth and elevation angles. +z is East and +x is North.*

equations [61]. For increased speed, a MATLAB® function was created to perform these calculations (see Appendix B). The solar position is defined by the azimuth and elevation angles (see Fig. A-5). The elevation angle is defined as the angle from the nearest horizon point to the Sun. The azimuth angle is defined as the clockwise angle from North to the Sun. These angles establish a spherical polar coordinate system for the position of the Sun. The solar vector can then be defined as

$$\vec{S} = (cos(Az)\,cos(El),\quad sin(El),\quad sin(Az)\,cos(El)). \qquad \text{Eq A-28}$$

The mirror vector is found by combination of the solar vector and normalized tower vector:

$$\vec{M} = \frac{\vec{S}+\vec{T}}{\|\vec{S}+\vec{T}\|}. \qquad \text{Eq A-29}$$

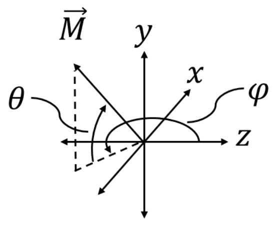

*Fig. A-6: A diagram outlining the two angular rotations of an alt-azimuth mounted heliostat to point the heliostat in the correct direction. +z is East and +x is North.*

The mirror vector can then be used to calculate the elevation and azimuth angles of the heliostat. The initial pointing of the heliostat is defined as East. This may seem arbitrary but is chosen because surfaces in non-sequential OpticStudio® are initially placed with their optical axes pointing along the z-axis. In order to have East, North, and Up all pointing along positive axes directions, the z-axis was chosen to point East and the x-axis was chosen to point North, leaving the y-axis to point Up. Thus, the heliostat azimuth angle $\varphi$ is defined as a counterclockwise rotation about the y-axis and the heliostat elevation angle $\theta$ is defined as a counterclockwise rotation about the local x-axis of the heliostat surface. Based on the geometry given in Fig. A-6,

$$\varphi = \text{atan2}\left(\frac{M_x}{M_z}\right), \qquad \text{Eq A-30}$$

$$\theta = \text{asin}(M_y), \qquad \text{Eq A-31}$$

where $M_x$, $M_y$, and $M_z$ are the three components of the mirror vector in the x, y, and z directions, respectively. Note, $\mathrm{atan2}(\mathrm{x})$ returns an angle between 0 and 2π.

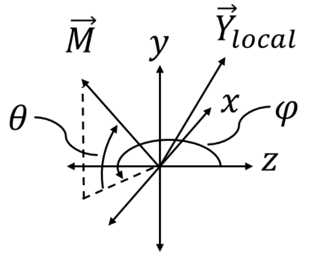

*Fig. A-7: Schematic showing the local y-axis of the heliostat mirror relative to the global coordinate system.*

The angle of incidence on the mirror surface is provided by

$$I = \mathrm{acos}\,(\vec{M} \cdot \vec{S})\ . \qquad \textit{Eq A-32}$$

To define the angle of astigmatism on the surface of the heliostat mirror, the local x and y-axes need to be defined in global coordinates (see Fig. A-7). The local y-axis is perpendicular to the mirror vector. Because of this orthogonality the y-component of the local y-axis is equivalent to the length of the projection of the mirror vector onto the x-y plane. Additionally, the projection of the local y-axis onto the x-z plane points 180° from the similarly projected mirror vector, but the magnitude of the projected local y-axis is the same as the y-component of the mirror vector. Therefore, the local y-axis can be calculated by

$$\vec{Y}_{local} = (-\,sin(\theta)\,cos\,(\phi),\quad \cos\,(\theta),\quad -\,sin(\theta)\,sin\,(\phi)). \qquad \textit{Eq A-33}$$

The local z-axis is just the mirror vector, which makes the local x-axis

$$\vec{X}_{local} = \vec{Y}_{local} \times \vec{Z}_{local}. \qquad \textit{Eq A-34}$$

With the local x, y, and z axes of the mirror in global coordinates, any vector defined in the global coordinate system can be defined in terms of the local axes of the mirror. Using basic vector algebra, the projected solar vector is determined by subtracting the component that points in the direction of the mirror vector, and then normalizing, which yields

$$\vec{S}_{projected} = \frac{\vec{S}-(\vec{M}\cdot\vec{S})\vec{M}}{\|\vec{S}-(\vec{M}\cdot\vec{S})\vec{M}\|}. \qquad \textit{Eq A-35}$$

The projected solar vector can then be converted into the local axes of the mirror for easily defining the angle of astigmatism. The rotation matrix that should be applied is

$$\bar{\bar{R}} = \begin{pmatrix} \vec{X}_{local} \\ \vec{Y}_{local} \\ \vec{Z}_{local} \end{pmatrix} = \begin{pmatrix} X_x & X_y & X_z \\ Y_x & Y_y & Y_z \\ Z_x & Z_y & Z_z \end{pmatrix}. \qquad \text{Eq A-36}$$

The local solar vector is then defined as

$$\vec{S}_{local} = \bar{\bar{R}}\vec{S}_{projected} = (S_x, \quad S_y), \qquad \text{Eq A-37}$$

which can be directly used to calculate the angle of astigmatism:

$$\gamma_A = \text{atan2}\left(\frac{S_y}{S_x}\right). \qquad \text{Eq A-38}$$

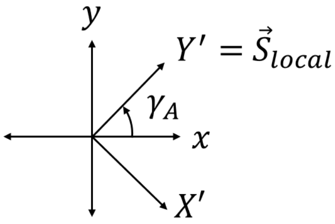

*Fig. A-8: In this figure $\gamma_A$ is the angle of astigmatism, Y' is the rotated y-axis (also the local solar vector), and X' is the rotated x-axis.*

The angle of astigmatism determines the orientation of the ideal toroid (see Fig. A-8). In a target-aligned heliostat [38], the heliostat is able to rotate about the mirror vector, thus keeping toroid oriented correctly in the tangential plane. For an alt-azimuth mounted heliostat, the *toroidal shape* must rotate about the mirror vector. Thus, the toroid must be defined in terms of the local x and y axes of the mirror. The ideal toroid in a rotated coordinate system is given by

$$Z = \frac{Y'^2}{2R_t} + \frac{X'^2}{2R_s}, \qquad \text{Eq A-39}$$

where $R_t$ and $R_s$ are given by Eq A-22 and Eq A-23, $Z$ is the sag of the surface, and $X'$ and $Y'$ are the rotated coordinates. These rotated coordinates in terms of local coordinates are given by:

$$X' = S_y x - S_x y, \qquad \text{Eq A-40}$$

$$Y' = S_x x + S_y y, \qquad \text{Eq A-41}$$

which come from the local solar vector (Eq A-37).

Plugging in the rotated coordinates in terms of local x and y coordinates provides the ideal sag of the surface:

$$z = \frac{\left(S_x x + S_y y\right)^2}{2R_t} + \frac{\left(S_y x - S_x y\right)^2}{2R_s}. \qquad \textit{Eq A-42}$$

This expression is suitable for use in the computer, but greater insight into the composition of the surface is found by reducing this expression. After much algebraic manipulation the surface can be decomposed into three separate modes,

$$z = \frac{1}{4}\left(\frac{1}{R_t} + \frac{1}{R_s}\right)(x^2 + y^2) + S_x S_y \left(\frac{1}{2R_t} - \frac{1}{2R_s}\right) 2xy + \frac{1}{2}\left(\frac{1}{2R_t} - \frac{1}{2R_s}\right)\left(S_x^2 - S_y^2\right)(x^2 - y^2), \qquad \textit{Eq A-43}$$

which expression can be further simplified to

$$z = \frac{1}{4}(C_t + C_s)(x^2 + y^2) + \frac{1}{4}(C_t - C_s)\sin(2\gamma_A)\, 2xy + \frac{1}{4}(C_t - C_s)\cos(2\gamma_A)\,(x^2 - y^2) \qquad \textit{Eq A-44}$$

with $C_t = \cos(I)/R$ and $C_s = 1/(R\cos(I))$.

This functional form of the surface sag shows that the surface is made up of three different terms: power $(x^2 + y^2)$, oblique astigmatism $(2xy)$, and vertical astigmatism $(x^2 - y^2)$. These are of the same form as the Zernike standard surface polynomials. These also happen to be the bending modes that are naturally part of a flat plate [62,63]. Thus, the desired shape can be readily induced into a flat back-silvered mirror.

In its final form, the surface shape equation and its three coefficients are given by

$$a_1 = \frac{1}{4}(C_t + C_s), \qquad \textit{Eq A-45}$$

$$a_2 = \frac{1}{4}(C_t - C_s)\ \sin(2\gamma_A), \qquad \textit{Eq A-46}$$

$$a_3 = \frac{1}{4}(C_t - C_s)\ \cos(2\gamma_A), \qquad \textit{Eq A-47}$$

$$z = a_1(x^2 + y^2) + a_2(2xy) + a_3(x^2 - y^2). \qquad \textit{Eq A-48}$$

The angle of astigmatism, $\gamma_A$, is found by combination of Eq A-28 through Eq A-38. A MATLAB® function is given in Appendix C to calculate these coefficients.

# Appendix B : SOLAR POSITION MATLAB® CODE

```
function [A1,A2] =
SolarPositionCalculatorV3(Lat,Lon,TZone,Year,Month,Day,Time)
%This function uses equations from the NOAA Solar Calculations
excel file
%,found free online, to calculate Solar Azimuth and Elevation
angles.
%Using latitude, longitude, timezone, localtime, year, month,
and day, the
%solar azimuth and elevation angles are calculated.

%If there are no input arguments, then calculations are
performed for
%September 15, 2020 at Noon in Tucson, AZ. If Time is not
included, it is
%set to Noon and the function returns sunrise and sunset times.
If Time is
%given, then the function returns the Solar Azimuth and Solar
Elevation
%angles

%The NOAA solar position calculations are based on equations
from
%Astronomical Algorithms by Jean Meeus. For more information
visit:
%https://www.esrl.noaa.gov/gmd/grad/solcalc/calcdetails.html#:~:
text=General,minutes%20outside%20of%20those%20latitudes.

%By Ryker W. Eads at The University of Arizona

%8/14/2020
%V1 - RWE: Uses reads and writes from excel spread sheet from
NOAA.
%8/19/2020
%V2 - RWE: Updated calculator to no longer need excel
spreadsheet.
%8/19/2020
%V3 - RWE: Fixed incorrect calculations, and decreased
computation time by
%vectorization.
```

```
if nargin == 0
    Lat = 32.0944;
    Lon = -110.8147;
    TZone = -7;
    Year = 2020;
    Month = 6;
    Day = 21;
    Time = 12/24;%Out of 1
elseif nargin == 6
    Time = 0.5;%Out of 1
elseif nargin ~= 7
    errmsg = ['Incorrect number of inputs. Read notes at 
beginning of function.' ...
    ,'(Lat,Lon,TZone,Year,Month,Day,[Time])'];
    errordlg(errmsg)
end


DateNumber = datenum(Year,Month,Day);%Serial date in matlab

ExDate = DateNumber - 693960;%Convert to serial date in excel

JulDay = ExDate + 2415018.5 + Time - TZone/24;%Julian day

JulCen = (JulDay-2451545)/36525;%Julian century

%Geometric mean long sun (deg)
GMLS = mod(280.46646+JulCen.*(36000.76983 + 
JulCen*0.0003032),360);

%Geometric mean anom sun (deg)
GMAS = 357.52911+JulCen.*(35999.05029 - 0.0001537*JulCen);

%Eccentric Earth Orbit
EEO = 0.016708634-JulCen.*(0.000042037+0.0000001267*JulCen);

%Sun Eq of Ctr
SEOC = sin(radians(GMAS)).*(1.914602-
JulCen.*(0.004817+0.000014*JulCen))+ ...
    sin(radians(2*GMAS)).*(0.019993-
0.000101*JulCen)+sin(radians(3*GMAS))*0.000289;

%Sun True Long (deg)
STL = GMLS + SEOC;
```

```
%Sun Trun Anom (deg)
STA = GMAS + SEOC;

%Sun Rad Vector (AUs)
SRV = (1.000001018*(1-EEO.^2))./(1+EEO.*cos(radians(STA)));

%Sun App Long (deg)
SAL = STL-0.00569-0.00478*sin(radians(125.04-1934.136*JulCen));

%Mean Oblique Ecliptic (deg)
MOE = 23+(26+((21.448-JulCen.*(46.815+JulCen.*(0.00059-
JulCen*0.001813))))/60)/60;

%Obliq Corrected (deg)
OC = MOE+0.00256*cos(radians(125.04-1934.136*JulCen));

%Sun Rt Ascen (deg)
SRA =
degrees(atan2(cos(radians(OC)).*sin(radians(SAL)),cos(radians(SA
L))));

%Sun Declin (deg)
SDE = degrees(asin(sin(radians(OC)).*sin(radians(SAL))));

%Variable y
vy = tan(radians(OC/2)).^2;

%Eq of Time (minutes)
EOT = 4*degrees(vy.*sin(2*radians(GMLS))-
2*EEO.*sin(radians(GMAS)) ...
    +4*EEO.*vy.*sin(radians(GMAS)).*cos(2*radians(GMLS)) ...
    -0.5*vy.^2.*sin(4*radians(GMLS))-
1.25*EEO.^2.*sin(2*radians(GMAS)));

%HA Sunrise (deg)
HASR =
degrees(acos(cos(radians(90.833))./(cos(radians(Lat))*cos(radian
s(SDE))) ...
    -tan(radians(Lat))*tan(radians(SDE))));

%Solar Noon (LST)
SN = (720-4*Lon-EOT+TZone*60)/1440;

%Sunrise Time (LST)
SRT = (SN*1440-HASR*4)/1440;
```

```
%Sunset Time (LST)
SST = (SN*1440+HASR*4)/1440;

%Sunlight Duration (minutes)
SD = 8*HASR;

%True Solar Time (minutes)
TST = mod(Time*1440+EOT+4*Lon-60*TZone,1440);

%Hour Angle (deg)
if(TST/4<0)
    HA = TST/4+180;
else
    HA = TST/4-180;
end

%Solar Zenith Angle (deg)
SZA = degrees(acos(sin(radians(Lat))*sin(radians(SDE)) ...
    +cos(radians(Lat))*cos(radians(SDE)).*cos(radians(HA))));

%Solar Elevation Angle (deg)
solelu = 90 - SZA;

%Approximate Atmospheric Refraction (deg)
AAR = zeros(size(solelu));

%Switch cases
C1 = solelu>=85;
C2 = (solelu>=5)&(solelu<85);
C3 = (solelu<5)&(solelu>=-0.575);
C4 = solelu<-0.575;

if sum(C1)>0%Ensure there are elements in existence that meet
the case
    AAR(C1) = 0;
end
if sum(C2)>0
    AAR(C2) = (58.1./tan(radians(solelu(C2)))-
0.07./tan(radians(solelu(C2))).^3 ...
            +0.000086./tan(radians(solelu(C2))).^5)/3600;
end
if sum(C3)>0
    AAR(C3) = (1735+solelu(C3).*(-518.2+solelu(C3).* ...
```

```
            (103.4+solelu(C3).*(-
12.79+solelu(C3)*0.711))))/3600;
end
if sum(C4)>0
    AAR(C4) = -20.772./tan(radians(solelu(C4)))/3600;
end

%Solar Azimuth Angle (deg)
theta = degrees(acos(((sin(radians(Lat))*cos(radians(SZA))) ...
        -
sin(radians(SDE)))./(cos(radians(Lat))*sin(radians(SZA)))));
solaz = mod(180 + (1-sign(HA))*180 + sign(HA).*theta,360);

%Solar Elevation Angle Corrected (deg)
solel = solelu + AAR;

if nargin == 6 %If time is not included, return Sunset and
Sunrise
    A1 = SRT;
    A2 = SST;
else %If there are no arguments, or 7 arguments, return solar az
and el.
    A1 = solaz;
    A2 = solel;
    if nargin == 0
        A1 = [A1,A2];%Display azimuth and elevation
    end
end

function rad = radians(deg)
    %Convert degrees to radians
        rad = deg*pi/180;
end

function deg = degrees(rad)
    %Convert radians to degrees
        deg = rad*180/pi;
end

end
```

# Appendix C : HELIOSTAT SHAPE COEFFICIENTS MATLAB® CODE

```
function [a1,a2,a3,rot_astig,rotaz,rotel,I]  ...
    = HeliostatShapeProperties(solaz,solel,towerVec)
%% This program calculates the ideal analytical heliostat shape
and
%orientation for heliostats on dual-axis az-el mounts.

%The tangential and sagittal radii of curvature are calculated
for the
%given geometry at the specified time. Due to the nature of az-
el heliostat
%mounts, the angle of astigmatism on the surface of the
heliostat mirror
%must vary throughout the day to correct for off-axis
aberrations properly.
%The effective radii of curvature are derived from the
Coddington
%equations: Rt = R/cos(AOI), Rs = R*cos(AOI). Thus, to correct
for
%astigmatism, the tangential and sagittal radii of curvature
must be
%changed to make the correction, i.e. set Rt = R*cos(AOI) and Rs
=
%R/cos(AOI). Then sunlight will focus both in the tangential and
sagittal
%planes at the same distance, R/2, from the mirror vertex. The
shape must
%be aligned such that the plane containing the solar vector,
tower vector,
%and mirror vertex is the tangential plane. Thus, the astigmatic
shape must
%be locally rotated on the surface of the mirror to keep the
tangential
%radius of curvature in the tangential plane.

%solaz is the Solar Azimuth angle(s), solel is the Solar
Elevation angle(s)
%and towerVec is the tower vector, which is defined as the
vector from the
%heliostat to the tower target. The input angles should be in
units of
```

```
%degrees. The tower vector should be in units of mm. +x is
North, +z is
%East, and +y is up.

%As an example, a tower vector [10000,20000,-40000] means the
target is 10
%m North of the heliostat, 20 m up, and 40 m West.

%The outputs are the shape coefficients, a1, a2 and a3, which
are used in
%the equation Z = a1*(x^2+y^2) +a2*(2*x*y)+a3*(x^2-y^2).
rot_astig is the
%angle of astigmatism defining the orientation of the tangential
radius of
%curvature relative to the local x-axis of the mirror. rotaz is
the
%required rotation of the heliostat mirror about its azimuth
axis, and
%rotel is the rotation about the elevation axis. I is the angle
of
%incidence, which is needed to calculate toroidal curvatures,
and is an
%optional output for further calculations (such as cosine
factor).

%% Establish solar positions.
solazrad = solaz'*pi/180;
solzerad = (90 - solel')*pi/180;%Convert to Zenith angle

numTimes = length(solel);%Number of times at which to calculate
shape
%% Define Tower Vector
%All units in mm
% towerVec = [0 0 -40000];%+X is North, +Z is East, +Y is Up
if norm(towerVec)>0
    towerVec_u = towerVec/norm(towerVec);%Normalized tower
vector from mirror to target
else
    a1=NaN;
    a2=NaN;
    a3=NaN;
    rot_astig=NaN;
    rotaz=NaN;
    rotel=NaN;
    I=NaN;
```

```
    errordlg('Invalid Tower Vector. Please read function
description.')
    return;
end

%% Calculate angle of incidence and angle of astigmatism
solVec_u = [cos(solazrad).*sin(solzerad), cos(solzerad), ...
    sin(solazrad).*sin(solzerad)];%Solar vector from mirror to
sun
tVecRep = repmat(towerVec_u,size(solVec_u,1),1);%Repeat tower
vector for
%calculations
mVec = tVecRep + solVec_u;%Mirror pointing vector = tower vector
+ solar vector
mVec_u = zeros(size(mVec));%Preallocate
for i = 1:numTimes
    mVec_u(i,:) = mVec(i,:)/norm(mVec(i,:));%Normalized mirror
pointing vector
end

rotaz = atan2(mVec_u(:,1),mVec_u(:,3))*180/pi;%Rotate mirror
about
%local Y-axis, i.e. Vertical vector, beginning with mirror
pointed East.
rotel = -asin(mVec_u(:,2))*180/pi;%Rotate mirror about local x-
axis, Zemax input
%Note, rotel is actually -rotel, for ease in entering into
Zemax.
%%
%Elevation axis calculation
% Mx = mVec_u(:,1);
% My = mVec_u(:,2);
% Mz = mVec_u(:,3);
% Nz = -My.*Ny.*Mz./(Mx.^2+Mz.^2);
% Nx = -My.*Ny.*Mx./(Mx.^2+Mz.^2);

Ny = cos(rotel*pi/180);
Nx = -sin(-rotel*pi/180).*sin(rotaz*pi/180);
Nz = -sin(-rotel*pi/180).*cos(rotaz*pi/180);

newY = [Nx,Ny,Nz];%Local Y-axis

sol_dot_m = zeros(numTimes,1);%Preallocate
solVec_proj = zeros(size(mVec_u));
sol_proj_u = solVec_proj;
```

```
for i = 1:numTimes
    %Dot product of solar and mirror vectors
    sol_dot_m(i) = solVec_u(i,:)*mVec_u(i,:)';
    %Subtract the mirror normal vector component of solar vector
to project
    %the solar vector onto the mirror plane.
    solVec_proj(i,:) = solVec_u(i,:) - sol_dot_m(i)*mVec_u(i,:);
    %Normalize projected solar vector for later calculations.
    sol_proj_u(i,:) = solVec_proj(i,:)/norm(solVec_proj(i,:));
end

AOIrad = acos(sol_dot_m);%Angle of incidence
I = AOIrad*180/pi;

newZ = mVec_u;%Local Z-axis of mirror
newX = zeros(size(newZ));
for i = 1:length(I)
    newX(i,:) = cross(newY(i,:),newZ(i,:));%Local X-axis of
mirror, derived form Y and Z axes
end

S = zeros(size(sol_proj_u));
for i = 1:numTimes
    %Rotation matrix for reducing vectors to two dimensions on
the mirror
    %plane
    Mrot = [newX(i,:);newY(i,:);newZ(i,:)];
    %Rotate the projected solar vector
    S(i,:) = Mrot*sol_proj_u(i,:)';

end
%Calculate the angle of astigmatism
rot_astig = atan2(S(:,2),S(:,1))*180/pi;
rot_astig(rot_astig<0) = rot_astig(rot_astig<0) + 360;
%% Establish non-rotated surface shape
RofC = 2*norm(towerVec);%No astigmatism radius of curvature.
R_tan = RofC./cos(I*pi/180);%Local y radius of curvature
R_sag = RofC.*cos(I*pi/180);%Local x radius of curvature

%% Calculate rotated shape
%Change to curvatures for calculations
C_tan = 1./(R_tan);
C_sag = 1./(R_sag);
%Derived from analytical calculations
a1 = (C_tan + C_sag)/4;
```

```
a2 = (C_tan - C_sag).*S(:,1).*S(:,2)/2;
a3 = (C_tan - C_sag).*(S(:,1).^2-S(:,2).^2)/4;
end
```

# Appendix D : **SELECTED PUBLICATION**

Optical design for a fly's eye CPV system with large, on-axis dish solar concentrator

Reproduced from [R. W. Eads, J. Hyatt, and R. Angel, "Optical design for a Fly's eye CPV system with large, onaxis dish solar concentrator," in *AIP Conference Proceedings* (2019), Vol. 2149.], with the permission of AIP Publishing .

## Optical Design for a Fly's Eye CPV System with Large, On-axis Dish Solar Concentrator

Ryker W. Eads[1, a)], Justin Hyatt[1], and Roger Angel[1, 2]

[1]*The University of Arizona, 933 N Cherry Ave, Tucson, AZ 85719, USA*
[2]*REhnu Inc., 1718 E Speedway Blvd #221 Tucson, AZ 85719, USA*

[a)]Corresponding author: eadsr@email.arizona.edu

**Abstract.** Here we describe an optical concentrator system for CPV which uses a large dish reflector to concentrate sunlight and a small receiver with fly's eye lens array to apportion the focused sunlight equally between many multi-junction cells. The small receiver is fan cooled. This architecture is aimed at a reduction in cost of complete CPV generating systems, which include dual axis tracking. In many CPV systems the light is evenly divided by identical Fresnel lenses facing the sun, and the cells are typically housed along with the lenses in modules, backed by large, passively cooled aluminum plates. The fly's eye system advantages are that the weight, complexity and cost of the inherently large scale optical collection is reduced to just that of the 4 mm thick glass mirrors, and the small receiver packages are easier and less expensive to manufacture than large modules. A specific fly's eye generator design using two large off-axis primary reflectors and non-obscuring receivers below the collection area has been described recently by Hyatt et al. [1], and the principles have been demonstrated in a prototype. Here we describe an alternative on-axis design optimized for greater uniformity of the light distributed to the cells, and excellent tolerance to mispointing. Ray tracing analysis shows deviations in uniformity of the full spectrum of sunlight distributed to the many cells of no more than 1% for sun mispointing angles of up to 0.5° and 80% of the maximum flux reaches the CPV cells when mispointing to +/- 0.9°. In this design, the central receiver blocks 4% of the entering sunlight, however, mechanical construction is simplified with a corresponding reduction in weight and cost. Also, not all the light blocked by the receiver is wasted, since it will be used to power the receiver's cooling fan via a built-in small PV panel, eliminating parasitic power loss.

### INTRODUCTION

Mirror Concentrated Photovoltaic (CPV) systems are ideal for concentrating large areas of light due to their low cost, achromaticity and fast focal ratios (high concentrations). However, at high concentration the angle of acceptance

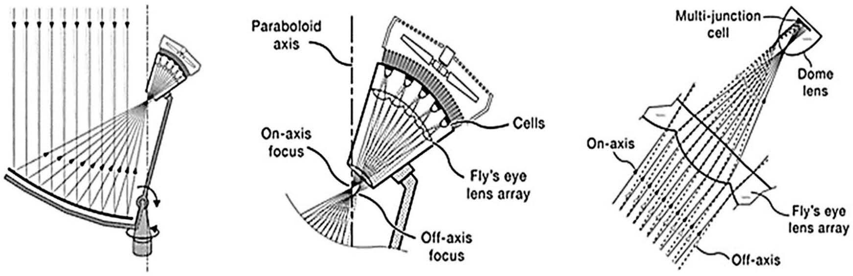

**FIGURE 1.** Schematics of the optical design by Hyatt et. al.[1]

may be small unless the optics preserve étendue. Field lenses and other additional optics may be used in a mirror CPV system to maximize mispointing tolerance. A previous design by Hyatt et. al. [1] used an off-axis dish mirror, field lens, a fly's eye lens array, and dome lenses to achieve ~500x geometric concentration and accepting 80% of full power when the sun pointing is 0.7° off axis. Due to the asymmetry of this previous design only two of these systems may be placed on a tracker with no tracker-to-tracker shadowing, and a substantial receiver support structure is necessary to reduce mispointing error due to gravity and wind. Additionally, because it is off axis, the 144 fly's eye lenses used for the 1.65-meter square mirror had each cut and positioned uniquely. All these factors together lead us to look for a simpler and more economical solution.

A new design of similar nature is here introduced though it uses an on-axis aspheric dish mirror. The on-axis receiver shadows 4% of the entrance pupil, but the system requires a simpler receiver support structure, functions at 1000x geometric concentration, and needs only 24 unique fly's eye lenslets. For this design there are the same number of dielectric-air interfaces, but with the proper implementation of anti-reflection (AR) coatings losses from these surfaces can be largely eliminated.

## OPTICAL DESIGN REQUIREMENTS

Despite the high concentration used in this new system, a large acceptance angle is still required to allow for mispointing. We targeted 0.5° of sun mispointing with no vignetting at 0.7 micron wavelength. Additionally, the design requires achromaticity over a large range of wavelengths from 0.4-1.6 microns, though we allow small vignetting for >1.0 micron wavelength. Another requirement is that that each junction of the multi-junction (MJ) cell receives the same geometric concentration. The entrance pupil is divided into 100 equal amounts of light (the central 4 are blocked) so that each MJ cell receives equal flux. The optics for this design are low cost: the dish mirror is made by slumping [2], there are only 24 unique lenses in the fly's eye array, the field lens is low mass and has only spherical surfaces, and identical dome lenses are placed on top of each MJ cell. The symmetry of this design is what reduces the cost significantly. Also, the high concentration reduces the total area of MJ cells by a factor of 2 compared to the previous design [1].

## IMPLEMENTATION

The distribution of light on the fly's eye array is to be independent of allowed pointing errors. This is accomplished by using a field lens to image the primary onto the fly's eye array (Figure 2(a)). The concentration at the fly's eye array is 35x, which yields an energy density where air cooling can be used [1]. Different lenslet sizes across the pupil

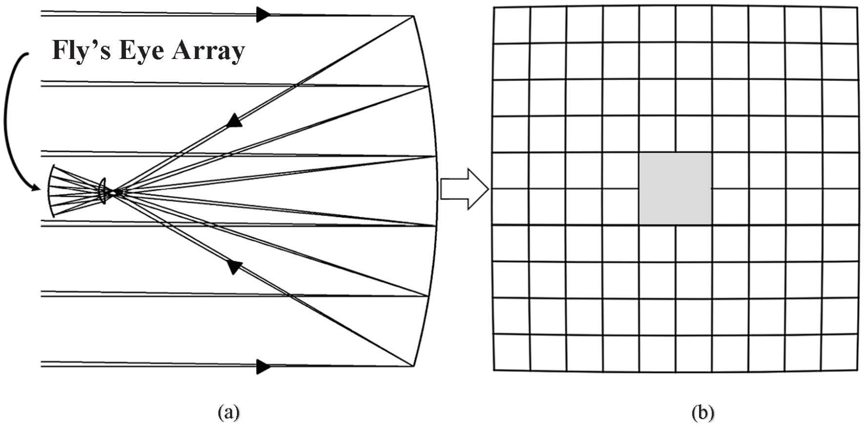

**FIGURE 2.** (a) Overall optical design of the system showing the imaging of the primary onto the fly's eye surface. (b) Barrel shaped entrance pupil divided into 100 equal areas.

diameter of a small reference segment of light, and D represents the clear aperture diameter of a chosen segment of light.

$$\varphi \sim R^2 + \left(f - \frac{R^2}{4f}\right)^2 \tag{1}$$

$$\frac{D}{D_0} = \sqrt{\frac{f^2}{R^2 + \left(f - \frac{R^2}{4f}\right)^2}} \tag{2}$$

The reference lenslet is chosen to be centered on the image of the parabolic mirror. This lenslet and its dome lens are optimized together for ideal imaging of the pupil. Each lenslet is scaled according to its distance from the image center. On-axis chief rays are used to position lenses, and the radii of curvature and clear aperture diameters are chosen according to their radial distance from the optical axis, scaling the reference lenslet by equation (2). The boundaries between lenslets are those naturally formed by the intersection of axially symmetric lenses (no discontinuities).

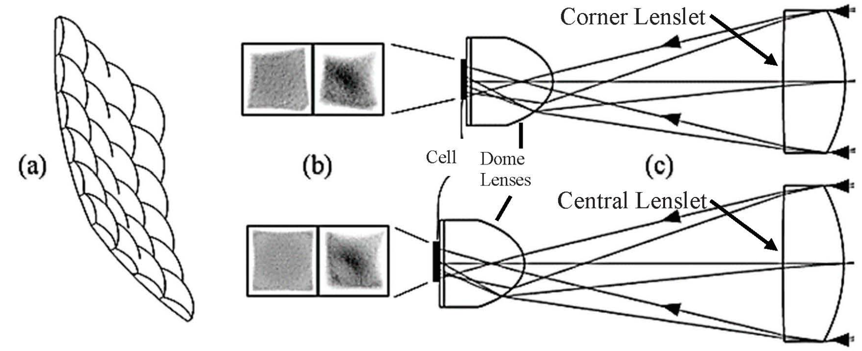

**FIGURE 4.** (a) Isometric view of lens array. (b) Solar illumination of 5.4 mm square cells, on- and off-axis by 0.5° in each case. (c) Detail of rays focused by large and small fly's eye lenses to cell/dome assemblies.

Due to symmetry the initial design is only one quadrant of the system according to the division shown in Figure 3(b). Thus, a 4x6 fly's eye lens array is created along the pupil image surface with each lens changing in size and curvature to conserve throughput to each CPV cell. An isometric view of the lens array is shown in Figure 4(a). The variation in size of lenses, and conservation of throughput is well represented by Figure 4(c). Non-sequential ray tracing provides proof of concept in Figure 4(b) showing the similarity in flux distribution for on axis sun and 0.5° off axis sun.

## RESULTS

Ray tracing one quadrant of this optical design shows performance for the system as a whole. In Figure 5, the flux received of 96 cells are plotted in a bar graph where 100% is the mean cell flux, and the binning is set to every 0.5%. The flux to each cell varies +/-1% from the mean for on-axis sunlight and 0.5° off-axis. Thus, all 96 cells may be placed on a single circuit with all cells running near optimal current. This simplifies the electronics required to maintain high output and reduces the overall cost. 80% of the maximum flux is still achieved for +/- 0.9° off-axis sun.

The overall efficiency of the system is limited by the number of dielectric-air interfaces. The dish mirror is back-silvered with a reflectivity near 95%. Acid-etched coatings on all the lenses create transmissions greater than 99% [1, 4] for each surface, 5 surfaces total. Also, 4% of the mirror is shadowed. This leads to an ideal optical efficiency of 86.7%. Using a 4J CPV cell with 43% efficiency at 1000x [5], the overall ideal system efficiency is 37.3%.

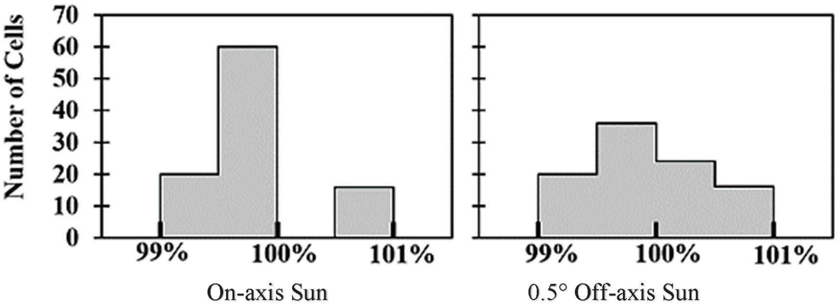

**FIGURE 5.** Flux distribution across cells for sun on-axis and ½° off axis

## CONCLUSION

A new two-stage concentration design is shown that uses first a field lens to image the mirror onto a fly's eye array at 35x geometric concentration. A dome lens images each fly's eye lenslet onto a MJ cell to further boost concentration to 1000x. The dish mirror can be constructed by slumping square glass sheets, produceing a barrel shaped entrance pupil. The pupil is divided into 100 equal areas where the central 4 areas are shadowed by the receiver. The field lens is thin (~25mm) and has spherical surfaces. The fly's eye lens array has quad symmetry that requires only 24 unique lenses for construction, and each dome lens and cell is identical. The flux distribution across the cells for an on-axis and ½° off-axis sun are uniform to within 1% allowing high mispoint and tolerance for alignment. 80% of the maximum flux is still obtained when sun mispointing is +/- 0.9°. All these design points paint a picture of a cost-effective CPV system with ideally 37.3% system efficiency.

Future developments involve researching a manufacturing method for a 4x6 fly's eye array and the creation of a prototype inexpensive dual-axis tracker unit (where much of the cost for CPV systems is rooted).

## ACKNOWLEDGMENTS

We gratefully acknowledge support from the University of Arizona Office of Research, Discovery & Innovation.

## REFERENCES

1. AIP Conference Proceedings 2012, 030008 (2018); https://doi.org/10.1063/1.5053507
2. [2] Proceedings Volume 9175, High and Low Concentrator Systems for Solar Energy Applications IX; 91750B (2014) https://doi.org/10.1117/12.2062394
3. [3] Blake M. Coughenour, Thomas Stalcup, Brian Wheelwright, Andrew Geary, Kimberly Hammer, and Roger Angel, "Dish-based high concentration PV system with Köhler optics," Opt. Express 22, A211-A224 (2014)
4. L. McCollister, H & Pettit, Richard. (1983). Antireflection Pyrex Envelopes for Parabolic Solar Collectors. Journal of Solar Energy Engineering-transactions of The Asme - J SOL ENERGY ENG. 105. 425-429. 10.1115/1.3266403.
5. Steiner, Marc & Siefer, Gerald & Schmidt, Thomas & Wiesenfarth, Maike & Frank, Dimroth & Bett, Andreas. (2016). 43 % direct sunlight conversion efficiency using 4J cells with achromatic full glass lens. 1766. 080006. 10.1063/1.4962104.

# Appendix E : **DOUBLE CASSEGRAIN MATLAB® CODE**

```
%This script takes the mirror separation, back focal distance,
and focal
%length of the desired telescope and calculates the ideal radii
of
%curvature and conic constants for a Ritchey-Chretien telescope
and a
%Double-Cassegrain telescope.
%% b,d,f user input
clc, clear
prompt = {'Enter separation of mirrors [mm]:','Enter back focal
distance: [mm]', ...
    'Enter focal length of telescope [mm]:'};
dlgtitle = 'Input';
dims = [1 45];
definput = {'100','125','1000'};
answer = inputdlg(prompt,dlgtitle,dims,definput);

    d=str2double(answer{1});
    b=str2double(answer{2});
    f=str2double(answer{3});

%% If boundary conditions are met, calculate:
if f>d/(sqrt(2)-1) && b+d<sqrt(f^2-2*d*f) && b>0 && f>0 && d>0

rad1 = d.*f.*(2.*b+(-3).*d+2.*f).*(b.^2+(2.*d+(-1).*f).*f).^(-
1)+(-1).*( ...
d.^2.*f.*(b.^2+(2.*d+(-1).*f).*f).^(-2).*(4.*b.^3+(-
4).*b.^2.*(d+( ...
-2).*f)+d.^2.*f+4.*b.*f.*((-1).*d+f))).^(1/2);%Radius of
curvature of primary

rad2 = (-2).*(f.*(4.*d.^4.*f+4.*d.^3.*(2.*f+(-
1).*rad1).*rad1+2.*d.^2.*(4.*f+ ...
  (-3).*rad1).*rad1.^2+2.*d.*(2.*f+(-
1).*rad1).*rad1.^3+f.*rad1.^4).*(8.*d.*f+ ...
  rad1.*(4.*f+rad1)).^(-
2)).^(1/2)+2.*f.*(6.*d.^2+6.*d.*rad1+rad1.^2).*(8.* ...
  d.*f+rad1.*(4.*f+rad1)).^(-1);%Radius of curvature of
secondary

%Conic constant of primary mirror
```

```
k1 = d.^(-2).*rad2.^(-2).*(8.*d.^4+8.*d.^3.*(rad1+(-
2).*rad2)+2.*d.* ...
rad1.*rad2.^2+(-1).*rad1.^2.*rad2.^2+2.*d.^2.*(rad1.^2+(-5).*
...
rad1.*rad2+4.*rad2.^2)).^(-1).*(64.*d.^8+64.*d.^7.*(4.*rad1+(-
3).* ...
rad2)+rad1.^4.*rad2.^3.*((-
1).*rad1+rad2)+2.*d.*rad1.^3.*rad2.^2.* ...
(3.*rad1.^2+(-8).*rad1.*rad2+4.*rad2.^2)+8.*d.^6.*(50.*rad1.^2+(
...
-84).*rad1.*rad2+25.*rad2.^2)+8.*d.^5.*(38.*rad1.^3+(-112).* ...
rad1.^2.*rad2+75.*rad1.*rad2.^2+(-10).*rad2.^3)+d.^2.*rad1.^2.*
...
rad2.*((-16).*rad1.^3+76.*rad1.^2.*rad2+(-
84).*rad1.*rad2.^2+21.* ...
rad2.^3)+2.*d.^4.*(56.*rad1.^4+(-280).*rad1.^3.*rad2+335.* ...
rad1.^2.*rad2.^2+(-
103).*rad1.*rad2.^3+4.*rad2.^4)+2.*d.^3.*rad1.* ...
(8.*rad1.^4+(-80).*rad1.^3.*rad2+170.*rad1.^2.*rad2.^2+(-98).*
...
rad1.*rad2.^3+11.*rad2.^4));

%Conic constant of secondary mirror (outer ring)
k2 = d.^(-2).*rad1.^(-1).*(d+rad1).^(-1).*(2.*d+rad1).^(-
2).*rad2.^(-1) ...
.*(8.*d.^4+8.*d.^3.*(rad1+(-2).*rad2)+2.*d.*rad1.*rad2.^2+(-1).*
...
rad1.^2.*rad2.^2+2.*d.^2.*(rad1.^2+(-5).*rad1.*rad2+4.*rad2.^2))
...
.^(-1).*(512.*d.^11+256.*d.^10.*(9.*rad1+(-
10).*rad2)+2.*rad1.^5.* ...
rad2.^5.*((-1).*rad1+rad2)+d.*rad1.^4.*rad2.^4.*(19.*rad1.^2+(-
45) ...
.*rad1.*rad2+22.*rad2.^2)+32.*d.^9.*(134.*rad1.^2+(-333).*rad1.*
...
rad2+164.*rad2.^2)+32.*d.^8.*(132.*rad1.^3+(-
567).*rad1.^2.*rad2+ ...
626.*rad1.*rad2.^2+(-176).*rad2.^3)+d.^2.*rad1.^3.*rad2.^3.*((-
83) ...
.*rad1.^3+334.*rad1.^2.*rad2+(-
356).*rad1.*rad2.^2+100.*rad2.^3)+ ...
d.^3.*rad1.^2.*rad2.^2.*(188.*rad1.^4+(-1221).*rad1.^3.*rad2+
...
2244.*rad1.^2.*rad2.^2+(-1392).*rad1.*rad2.^3+240.*rad2.^4)+8.*
...
```

```
d.^7.*(290.*rad1.^4+(-
2018).*rad1.^3.*rad2+3859.*rad1.^2.*rad2.^2+ ...
(-2436).*rad1.*rad2.^3+416.*rad2.^4)+8.*d.^6.*(84.*rad1.^5+(-
986) ...
.*rad1.^4.*rad2+3060.*rad1.^3.*rad2.^2+(-
3349).*rad1.^2.*rad2.^3+ ...
1284.*rad1.*rad2.^4+(-128).*rad2.^5)+2.*d.^4.*rad1.*rad2.*((-
101) ...
.*rad1.^5+1127.*rad1.^4.*rad2+(-3399).*rad1.^3.*rad2.^2+3664.*
...
rad1.^2.*rad2.^3+(-1404).*rad1.*rad2.^4+144.*rad2.^5)+2.*d.^5.*(
...
40.*rad1.^6+(-997).*rad1.^5.*rad2+5229.*rad1.^4.*rad2.^2+(-
9298).* ...
rad1.^3.*rad2.^3+6172.*rad1.^2.*rad2.^4+(-1376).*rad1.*rad2.^5+
...
64.*rad2.^6));

%Conic constant of "quaternary" mirror (inner annulus of
secondary)
k4 = (-1).*d.^(-1).*(d+rad1).^(-1).*(d+(-
1).*rad2).*(8.*d.^3+4.*d.* ...
rad1.*(rad1+(-2).*rad2)+4.*d.^2.*(3.*rad1+(-2).*rad2)+(-1).* ...
rad1.^2.*rad2).^(-2).*(8.*d.^4+8.*d.^3.*(rad1+(-2).*rad2)+2.*d.*
...
rad1.*rad2.^2+(-1).*rad1.^2.*rad2.^2+2.*d.^2.*(rad1.^2+(-5).*
...
rad1.*rad2+4.*rad2.^2)).^(-1).*(512.*d.^11+2560.*d.^10.*(rad1+(-
1) ...
.*rad2)+rad1.^5.*rad2.^4.*(rad1.^2+(-5).*rad1.*rad2+4.*rad2.^2)+
...
128.*d.^9.*(42.*rad1.^2+(-
91).*rad1.*rad2+40.*rad2.^2)+128.*d.^8.* ...
(48.*rad1.^3+(-171).*rad1.^2.*rad2+164.*rad1.*rad2.^2+(-40).*
...
rad2.^3)+d.*rad1.^4.*rad2.^3.*((-2).*rad1.^3+29.*rad1.^2.*rad2+(
...
-60).*rad1.*rad2.^2+28.*rad2.^3)+2.*d.^2.*rad1.^3.*rad2.^2.*(5.*
...
rad1.^4+(-58).*rad1.^3.*rad2+182.*rad1.^2.*rad2.^2+(-
176).*rad1.* ...
rad2.^3+44.*rad2.^4)+32.*d.^7.*(129.*rad1.^4+(-683).*rad1.^3.*
...
rad2+1090.*rad1.^2.*rad2.^2+(-
586).*rad1.*rad2.^3+80.*rad2.^4)+8.* ...
```

```
d.^5.*rad1.*(44.*rad1.^5+(-488).*rad1.^4.*rad2+1757.*rad1.^3.*
...
rad2.^2+(-2494).*rad1.^2.*rad2.^3+1336.*rad1.*rad2.^4+(-200).*
...
rad2.^5)+(-2).*d.^3.*rad1.^2.*rad2.*(16.*rad1.^5+(-
185).*rad1.^4.* ...
rad2+733.*rad1.^3.*rad2.^2+(-1096).*rad1.^2.*rad2.^3+564.*rad1.*
...
rad2.^4+(-64).*rad2.^5)+32.*d.^6.*(51.*rad1.^5+(-387).*rad1.^4.*
...
rad2+937.*rad1.^3.*rad2.^2+(-852).*rad1.^2.*rad2.^3+262.*rad1.*
...
rad2.^4+(-16).*rad2.^5)+8.*d.^4.*rad1.*(4.*rad1.^6+(-76).* ...
rad1.^5.*rad2+430.*rad1.^4.*rad2.^2+(-
959).*rad1.^3.*rad2.^3+840.* ...
rad1.^2.*rad2.^4+(-240).*rad1.*rad2.^5+8.*rad2.^6));

%Petzval curvature (i.e. imaging surface curvature)
P = -4/rad1+4/rad2;
%Petzval radius
Prad = 1/P;
else
    rad1 = NaN;
    rad2 = NaN;
    k1 = NaN;
    k2 = NaN;
    k4 = NaN;
    msg = ['Boundary conditions violated for Double-Cassegrain
Solution.', ...
        ' All values must be positive numbers and the focal
length should', ...
        ' be much larger than the mirror separation. See code
line 19 for more details.'];
    errordlg(msg)
end

%% Cassegrain Solution
r1 = 2.*d.*(b+(-1).*f).^(-1).*f;%Radius of curvature of primary
r2 = 2.*b.*d.*(b+d+(-1).*f).^(-1);%Radius of curvature of
secondary

%Conic constant of primary mirror
k1Cass = (b+(-1).*f).^(-3).*((-1).*b.^3+2.*b.*d.^2+3.*b.^2.*f+(-
3).*b.* ...
  f.^2+f.^3);
```

```
%Conic constant of secondary mirror (outer ring)
k2Cass = (b+d+(-1).*f).^(-3).*((-1).*b.^3+(-
1).*d.^3+d.^2.*f+d.*f.^2+f.^3+ ...
  b.^2.*(d+3.*f)+b.*(d.^2+(-2).*d.*f+(-3).*f.^2));

%Petzval curvature (i.e. imaging surface curvature)
P = -2/r1+2/r2;

%Petzval radius
PradCass = 1/P;
%% Display data

format longG
format compact
fS = '%.6f';
R1 = num2str(r1,fS);
R2 = num2str(r2,fS);
Rad1 = num2str(rad1,fS);
Rad2 = num2str(rad2,fS);
K1 = num2str(k1,fS);
K1Cass = num2str(k1Cass,fS);
K2 = num2str(k2,fS);
K2Cass = num2str(k2Cass,fS);
K4 = num2str(k4,fS);
K4Cass = 'NaN';
T =
table({R1;Rad1},{R2;Rad2},{K1Cass;K1},{K2Cass;K2},{K4Cass;K4},'V
ariableNames', ...
    {'R1','R2','K1','K2','K4'},'RowName',{'Ritchey-
Chretien','Double-Cassegrain'});
disp(T)
```

# REFERENCES

1. H. M. Martin, "Making mirrors for giant telescopes," in (2019).
2. J. E. Greivenkamp, *Field Guide to Geometrical Optics* (2009).
3. M. W. Davidson and T. J. Fellers, "Understanding Conjugate Planes and Kohler Illumination," Aperture (2002).
4. M. Johns, "The Giant Magellan Telescope (GMT)," in *Ground-Based and Airborne Telescopes* (2006).
5. M. Johns, P. McCarthy, K. Raybould, A. Bouchez, A. Farahani, J. Filgueira, G. Jacoby, S. Shectman, and M. Sheehan, "Giant Magellan Telescope: overview," in *Ground-Based and Airborne Telescopes IV* (2012).
6. H. Baig, K. C. Heasman, and T. K. Mallick, "Non-uniform illumination in concentrating solar cells," Renew. Sustain. Energy Rev. (2012).
7. L. Huang, M. Idir, C. Zuo, and A. Asundi, "Review of phase measuring deflectometry," Opt. Lasers Eng. (2018).
8. I. Trumper, H. Choi, and D. W. Kim, "Instantaneous phase shifting deflectometry," Opt. Express (2016).
9. L. Jiang, X. Zhang, F. Fang, X. Liu, and L. Zhu, "Wavefront aberration metrology based on transmitted fringe deflectometry," Appl. Opt. (2017).
10. L. Huang, J. Xue, B. Gao, C. Zuo, and M. Idir, "Zonal wavefront reconstruction in quadrilateral geometry for phase measuring deflectometry," Appl. Opt. (2017).
11. P. Su, R. E. Parks, L. Wang, R. P. Angel, and J. H. Burge, "Software configurable optical

test system: A computerized reverse Hartmann test," Appl. Opt. (2010).

12. A. Morales and D. Malacara, "Geometrical parameters in the Hartmann test of aspherical mirrors," Appl. Opt. (1983).
13. J. M. Sasian, *Introduction to Aberrations in Optical Imaging Systems.* (Cambridge University Press, 2012).
14. A. Rakich, "The 100th birthday of the conic constant and Schwarzschild's revolutionary papers in optics," in *Novel Optical Systems Design and Optimization VIII* (2005).
15. S. Yuan and J. Sasian, "Aberrations of anamorphic optical systems. I: The first-order foundation and method for deriving the anamorphic primary aberration coefficients," Appl. Opt. (2009).
16. P. J. Sands, "Thin double-plane symmetric field lenses," J. Opt. Soc. Am. (1973).
17. Y. Cao, L. Lu, and Z. Deng, "Chromatic aberration of plane-symmetric optical systems," Appl. Opt. (2019).
18. R. K. Tyson, "Conversion of Zernike aberration coefficients to Seidel and higher-order power-series aberration coefficients," Opt. Lett. (1982).
19. K. L. G. Parkin, "The Breakthrough Starshot system model," Acta Astronaut. (2018).
20. J. Hyatt, R. Eads, N. Didato, and R. Angel, "Laser beam projection for starshot launch," in *AO4ELT 2019 - Proceedings 6th Adaptive Optics for Extremely Large Telescopes* (2019).
21. C. Ai and J. C. Wyant, "Effect of piezoelectric transducer nonlinearity on phase shift interferometry," Appl. Opt. (1987).
22. P. J. de Groot, "Vibration in phase-shifting interferometry: errata," J. Opt. Soc. Am. A (1995).

23. C. P. Brophy, "Effect of intensity error correlation on the computed phase of phase-shifting interferometry," J. Opt. Soc. Am. A (1990).

24. K. Masuko, M. Shigematsu, T. Hashiguchi, D. Fujishima, M. Kai, N. Yoshimura, T. Yamaguchi, Y. Ichihashi, T. Mishima, N. Matsubara, T. Yamanishi, T. Takahama, M. Taguchi, E. Maruyama, and S. Okamoto, "Achievement of more than 25% conversion efficiency with crystalline silicon heterojunction solar cell," IEEE J. Photovoltaics (2014).

25. J. F. Geisz, R. M. France, K. L. Schulte, M. A. Steiner, A. G. Norman, H. L. Guthrey, M. R. Young, T. Song, and T. Moriarty, "Six-junction III–V solar cells with 47.1% conversion efficiency under 143 Suns concentration," Nat. Energy (2020).

26. C. Meehan, "NREL Developing Improved Tech to Lower Costs for Multi-Junction Solar Cells," (2018).

27. M. Saadah, E. Hernandez, and A. A. Balandin, "Thermal management of concentrated multi-junction solar cells with graphene-enhanced thermal interface materials," Appl. Sci. (2017).

28. J. Hyatt, C. Davila, N. Didato, R. Peon, M. Rademacher, D. Reshidko, F. Sodari, P. Strittmatter, G. Vincent, B. Wheelwright, C. Zammit, and R. Angel, "CPV generator with dish reflector and fly's eye receiver," in *AIP Conference Proceedings* (2018).

29. R. W. Eads, J. Hyatt, and R. Angel, "Optical design for a Fly's eye CPV system with large, onaxis dish solar concentrator," in *AIP Conference Proceedings* (2019), Vol. 2149.

30. W. Marion and S. Wilcox, "A new solar radiation data manual for flat-plate and concentrating collectors," in (2008).

31. B. Gross, "Replacing Fuels with Sunlight," (2020).

32. D. Barlev, R. Vidu, and P. Stroeve, "Innovation in concentrated solar power," Sol. Energy Mater. Sol. Cells (2011).

33. AFDC, "Hydrogen Basics," (n.d.).

34. D. Roberts, "This climate problem is bigger than cars and much harder to solve," (2019).

35. M. Solar, "Megalim Solar Power- The Project," (2019).

36. E. A. Igel and R. L. Hughes, "Optical analysis of solar facility heliostats," Sol. Energy (1979).

37. M. Lando, J. Kagan, B. Linyekin, L. Sverdalov, G. Pecheny, and Y. Achiam, "Astigmatic corrected target-aligned solar concentrator," Opt. Commun. (2000).

38. R. Zaibel, E. Dagan, J. Karni, and H. Ries, "An astigmatic corrected target-aligned heliostat for high concentration," Sol. Energy Mater. Sol. Cells (1995).

39. A. Kraemer, "At the solarpaces Conference, Heliogen INTRODUCES solar heat at 1 cent/kWh," (2020).

40. W. Xu, Z. Lu, H. Liu, H. Zhang, and Z. Ni, "Shape and alignment measurement of the heliostat by laser deflectometry," in *Optical Modeling and Measurements for Solar Energy Systems II* (2008).

41. M. Roger, C. Prahl, and S. Ulmer, "Fast Determination of Heliostat Shape and Orientation By Edge Detection and Photogrammetry," in *Proceedings of the 14th Biennial CSP SolarPACES Symposium* (2008).

42. R. Kingslake, "The “absolute” Hartmann test," Trans. Opt. Soc. (1928).

43. R. Huang, P. Su, J. H. Burge, L. Huang, and M. Idir, "High-accuracy aspheric x-ray mirror metrology using Software Configurable Optical Test System/deflectometry," Opt. Eng.

(2015).

44. R. Eads and R. Angel, "6.5 m telescope for multi-object spectroscopy over a 3° field of view," Appl. Opt. **59**, (2020).

45. N. MKS, "Piezo Actuator, Tiny Picomotor, 12.7 mm Travel, 0.25 in. Shank," (2020).

46. R. V. Shack and G. W. Hopkins, "SHACK INTERFEROMETER.," in *Clever Opt, Innovative Appl of Opt* (1977).

47. O. Pirnay, V. Moreau, and G. Lousberg, "OAJ: 2.6m wide field survey telescope," in *Ground-Based and Airborne Telescopes IV* (2012).

48. W. Saunders, P. Gillingham, G. Smith, S. Kent, and P. Doel, "Prime focus wide-field corrector designs with lossless atmospheric dispersion correction," in *Advances in Optical and Mechanical Technologies for Telescopes and Instrumentation* (2014).

49. R. Tamai and J. Spyromilio, "European Extremely Large Telescope: progress report," in *Ground-Based and Airborne Telescopes V* (2014).

50. J. C. Christou, "Image quality, tip-tilt correction, and shift-and-add infrared imaging," Publ. Astron. Soc. Pacific (1991).

51. L. Yuan, J. Xie, Z. He, Y. Wang, and J. Wang, "Optical design and evaluation of airborne prism-grating imaging spectrometer," Opt. Express (2019).

52. J. Sasián, *Introduction to Lens Design* (2019).

53. R. W. Eads and J. R. P. Angel, "A 20 m wide-field diffraction-limited telescope," Philos. Trans. R. Soc. A Math. Phys. Eng. Sci. **379**, 20200141 (2020).

54. G. Mosby, B. J. Rauscher, C. Bennett, E. S. Cheng, S. Cheung, A. Cillis, D. Content, D. Cottingham, R. Foltz, J. Gygax, R. J. Hill, J. W. Kruk, J. Mah, L. Meier, C. Merchant, L.

Miko, E. C. Piquette, A. Waczynski, and Y. Wen, "Properties and characteristics of the Nancy Grace Roman Space Telescope H4RG-10 detectors," J. Astron. Telesc. Instruments, Syst. (2020).

55. S. Aloezos, J. Crooke, C. D. Dressing, L. Fantano, J. E. Hylan, S. Tompkins, M. R. Bolcar, V. T. Bly, C. Collins, L. D. Feinberg, K. France, G. Gochar, Q. Gong, A. Jones, I. Linares, M. Postman, L. Pueyo, A. Roberge, L. Sacks, and G. West, "The Large UV/Optical/Infrared (LUVOIR) Surveyor: Decadal Mission concept design update," in (2017).
56. D. G. Korsch, "<title>Optical design considerations for next-generation space and lunar telescopes</title>," in *Space Astronomical Telescopes and Instruments*, P. Y. Bely and J. B. Breckinridge, eds. (SPIE, 1991).
57. J. B. Hadaway, M. E. Wilson, D. C. Redding, and R. A. Woodruff, "Lessons learned in the optical design of the Next-Generation Space Telescope," in *Space Telescopes and Instruments V* (1998).
58. J. M. Sasian, "Flat-Field, Anastigmatic, Four-Mirror Optical System For Large Telescopes," Opt. Eng. (1987).
59. C. Zhao and J. H. Burge, "Comparison of exact pupil astigmatism conditions with Seidel approximations," Appl. Opt. (2002).
60. "Astronomical algorithms," Choice Rev. Online (1992).
61. NOAA, "ESRL Global Monitoring Laboratory - Global Radiation and Aerosols," https://www.esrl.noaa.gov/gmd/grad/solcalc/calcdetails.html.
62. D. J. O’Boy and V. V. Krylov, "Vibration of a rectangular plate with a central power-law profiled groove by the Rayleigh-Ritz method," Appl. Acoust. (2016).

63. I. Senjanović, N. Hadžić, N. Vladimir, and D. S. Cho, "Natural vibrations of thick circular plate based on the modified Mindlin theory," Arch. Mech. (2014).